NVE

Jernbaneverket

Statens vegvesen

Satellittbasert radarinterferometri (InSAR) for naturfare, skred og infrastruktur

Naturfareprosjektet: Delprosjekt 3 Kartlegging, datasamordning og ROS-analyser

122
2015

RAPPORT

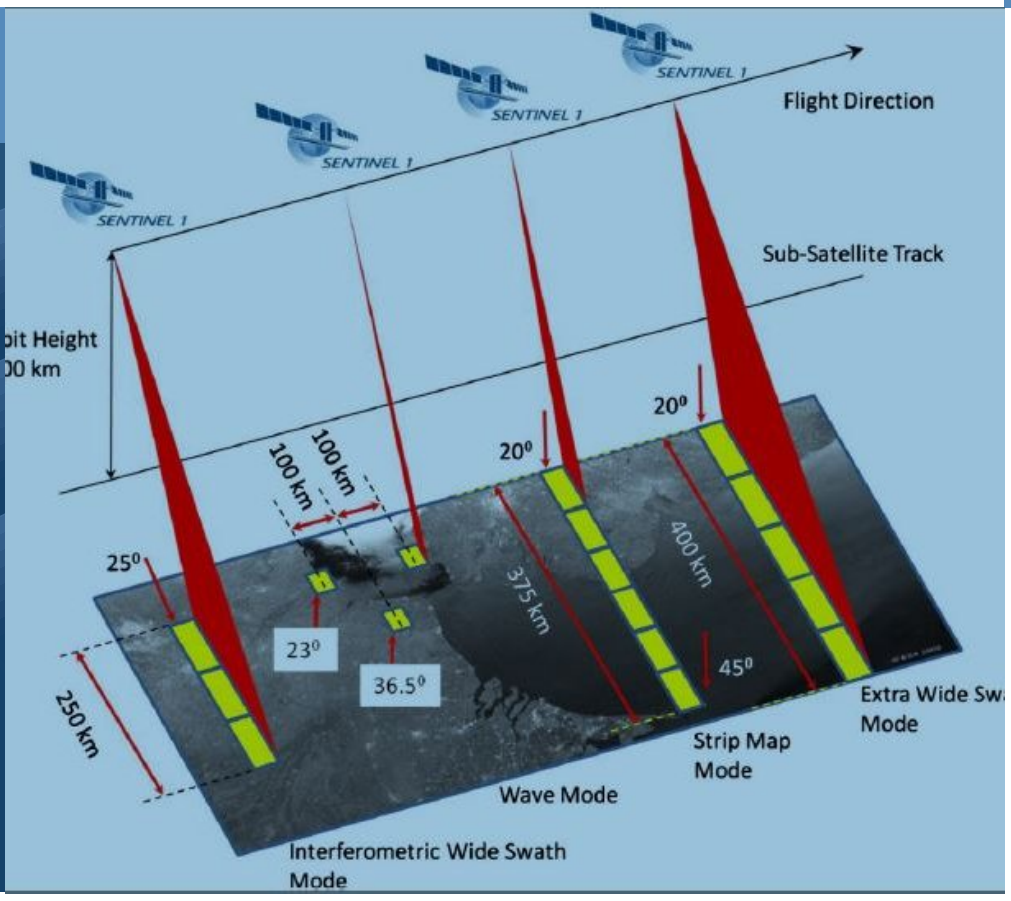

NIFS
NATURFARE
INFRASTRUKTUR - FLOM - SKRED

Rapport nr 122-2015

Satellittbasert radarinterferometri (InSAR) for naturfare, skred og infrastruktur

Utgitt av: Norges vassdrags- og energidirektorat

Redaktør:

Forfattere: Rouyet, Line; Lauknes, Tom Rune; Høgda, Kjell-Arild

Trykk: NVEs hustrykkeri
Opplag: P.O.D
Forsidefoto: Figur 6 From sentinel.esa.int.
ISBN 978-82-410-1174-0
ISSN 1501-2832

Sammendrag: The project aims to evaluate the potential (advantages and limitations) of satellite Synthetic Aperture Radar Interferometry (InSAR) technology for the mapping of deformation potentially damaging and dangerous for infrastructure and population, with a focus on the main interests of the three partners of the NIFS project

Emneord: SAR satellites, SAR Interferometry (InSAR), ground deformation, geohazards & infrastructure mapping and monitoring

Norges vassdrags- og energidirektorat
Middelthunsgate 29
Postboks 5091 Majorstua
0301 OSLO

Telefon: 22 95 95 95
Telefaks: 22 95 90 00
Internett: www.nve.no

NIFS
NATURFARE
INFRASTRUKTUR - FLOM - SKRED

norut
NORTHERN RESEARCH INSTITUTE

REPORT
05/2015
ISBN 978-82-7492-299-0
ISSN 1890-5226

Spaceborne radar interferometry (InSAR) for natural hazards, landslides and infrastructure: limitations and potential

Satellittbasert radarinterferometri (InSAR) for naturfare, skred og infrastruktur: begrensninger og muligheter

Author(s): Rouyet, Line; Lauknes, Tom Rune; Høgda, Kjell-Arild

PROJECT NAME: NIFS InSAR **PROJECT NO.**: 575

CONTRACTING: NVE, Statens vegvesen and Jernbaneverket

Document No.: 05/2015 Document Type: Report Status: Final

ISBN: 978-82-7492-299-0 ISSN: 1890-5226 No. of Pages: 76

Project leader: Line Rouyet Date: 01.03.2015

AUTHOR (S): Rouyet, Line; Lauknes, Tom Rune; Høgda, Kjell-Arild

TITLE: Spaceborne radar interferometry (InSAR) for natural hazards, landslides and infrastructure: limitations and potential / Satellittbasert radarinterferometri (InSAR) for naturfare, skred og infrastruktur: begrensninger og muligheter

SUMMARY:

The project aims to evaluate the potential (advantages and limitations) of satellite Synthetic Aperture Radar Interferometry (InSAR) technology for the mapping of deformation potentially damaging and dangerous for infrastructure and population, with a focus on the main interests of the three partners of the NIFS project (NVE, Statens vegvesen and Jernbaneverket). In this way, the report includes a presentation of the current status and use of InSAR technology in deformation mapping, a discussion about the advantages and limitations of the methods as well as future developments and potential. Examples were performed over Bergen area where two satellite datasets from RADARSAT-2 and one satellite dataset from TerraSAR-X/TanDEM-X [Cetinic, et al., 2015 (in prep.)] contribute to illustrate different advantages and limitations of the technology.

Keywords: SAR satellites, SAR Interferometry (InSAR), ground deformation, geohazards & infrastructure mapping and monitoring

Notices: -

PUBLISHER: Norut

CONTENTS

1 INTRODUCTION

This report is part of a Research & Development project initiated by Norges Vassdrags- og Energidirektorat (NVE), Statens vegvesen and Jernbaneverket. The NIFS (Naturfare - Infrastruktur - Flom - Skred) project is divided in seven subprojects focusing on hazards mapping and monitoring, early warning, risk assessment and crisis management (see www.naturfare.no). This is part of the NIFS subproject 3.1 (kartlegging skred og flom) aiming to provide an overview of the work in natural hazards mapping and assessment, taking into account the various processes: landslides, rockslides, avalanches, rockfalls, debris flows, floods.

The overall objective of the report "Spaceborne radar interferometry (InSAR) for natural hazards, landslides and infrastructure: limitations and potential" is to evaluate the potential (advantages and limitations) of satellite Synthetic Aperture Radar Interferometry (InSAR) technology for the mapping of deformation potentially damaging and dangerous for infrastructure and population, with a focus on the main interests of the three partners of the NIFS projects (NVE, Statens vegvesen and Jernbaneverket): landslides, rockfalls, movements affecting road/rails infrastructure, etc. It can be seen as a continuation of the report initiated by Norsk Romsenter (the Norwegian Space Center) about the multi-use potential of radar satellites and InSAR technology for mapping and monitoring landslide hazards and infrastructure: "Karlegging of overvåkning av skredfare of infrastruktur ved bruk av radarsatellitter og InSAR-metodikk" [Strøm, et al., 2014].

This report includes a presentation of the current status and use of InSAR technology in deformation mapping, a discussion of the potential of the methods, as well as recommendations for further works. Examples over Bergen area, where we used two satellite datasets from RADARSAT-2 and one satellite dataset from TerraSAR-X/TanDEM-X [Cetinic, et al., 2015 (in prep.)] contribute to illustrate different advantages and limitations of the technology. Chapter 2 is dedicated to theoretical explanations about SAR systems and InSAR methods. In Chapter 3, the context of the main study area, as well as the characteristics of the available data are introduced. In Chapter 4, examples of results over Bergen area are presented and discussed. The Chapter 5 is finally dedicated to the main discussions about the advantages and limitations of InSAR technology, as well as the future developments and potential in this field.

Acknowledgements: RADARSAT-2 data have been provided by Kongsberg Satellite Services (KSAT) through an agreement with Norwegian Space Centre, and TerraSAR-X/TanDEM-X data are owned by Globesar through an agreement with Airbus and are referred in the text to the report [Cetinic, et al., 2015 (in prep.)].

2 THEORY & METHODOLOGY

In this Chapter, we present an introduction to satellite Synthetic Aperture Radar (SAR) (2.1), SAR Interferometry (InSAR) technique for the detection of ground deformation (2.2) and the main processing steps and methods with their respective advantages and limitations (2.3).

The content of the Chapter is mainly based on the contributions of [Woodhouse, 2006; Lauknes, 2010; Ferretti, 2014]. More detailed treatments of the SAR principle can be found in e.g. [Curlander & McDonough, 1991; Franceschetti & Lanari, 1999; Cumming & Wong, 2005]. More details treatments of InSAR principles and processing can be found in e.g. [Massonnet and Feigl; 1998, Bamler and Hartl, 1998; Rosen et al., 2000; Rocca et al., 2000; Hanssen, 2001; Kampes, 2006; Ferretti, 2014].

2.1 SYNTHETIC APERTURE RADAR IMAGING

2.1.1 ACTIVE REMOTE SENSING

In active microwave remote sensing, electromagnetic waves are transmitted from an active sensor and the echoes (scattered signals) are then recorded and analyzed. This signal provides two main kinds of information related to distance information using the delay in the signal echo, and properties of the target using e.g. the intensity of the backscattered signal. Spaceborne or airborne active microwave sensors image the Earth to acquire information over a large surface using centimetric wavelength. They have a better ability to penetrate clouds, fogs and dust than optical sensors, as well as capability to image the Earth day and night.

2.1.2 SAR PRINCIPLE AND GEOMETRY

Synthetic Aperture Radar (SAR) system was developed in the fifties first for airborne missions. The technology allows using a short physical antenna, but in order to improve azimuth resolution, it synthetizes the effect of much longer antenna using the movement of the sensor along the satellite flying path (track). Resolution in range is obtained by using a high bandwidth system.

A spaceborne or airborne SAR has a side-looking geometry as shown in Figure 1. As the SAR moves along its (assumed) straight path, it illuminates a swath on the ground by transmitting a series of electromagnetic microwave pulses. The angle between the radar beam and the vertical is called *look angle*, while the angle between the radar beam and the surface normal (slightly larger due to the curvature of the Earth) is called *incidence angle*.

The SAR data are arranged as two-dimensional (2D) images with coordinates expressed in *slant range* (distance from the SAR sensor) and *azimuth* (position along the SAR flight path). Due to the side-looking geometry, and related to the conversion of the measured slant range to the ground range, geometrical distortions will appear in the SAR image. The process of generating SAR images with uniform pixel size in geographic coordinate system is called geocoding.

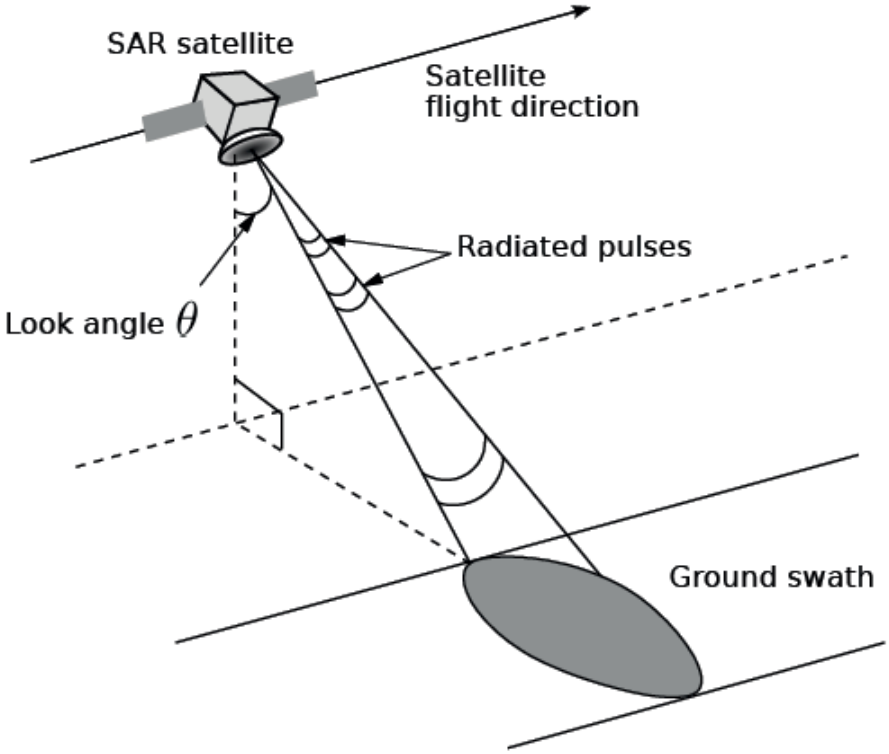

Figure 1: Simplified geometry of a Synthetic Aperture Radar (SAR) system. As the system moves along its flight path, it images an area on the ground called *swath*. From [Lauknes, 2010].

2.1.3 SAR ORBIT CONFIGURATION

Satellites equipped with SAR sensors have a near-polar orbit at an altitude between 500 and 800 km above the Earth's surface. Earth's rotation and satellite movement lead to an *ascending* and a *descending imaging geometry*. With an ascending orbit, the satellite crosses the equator going from South to North and with a descending orbit it crosses the equator going from North to South (Figure 2).

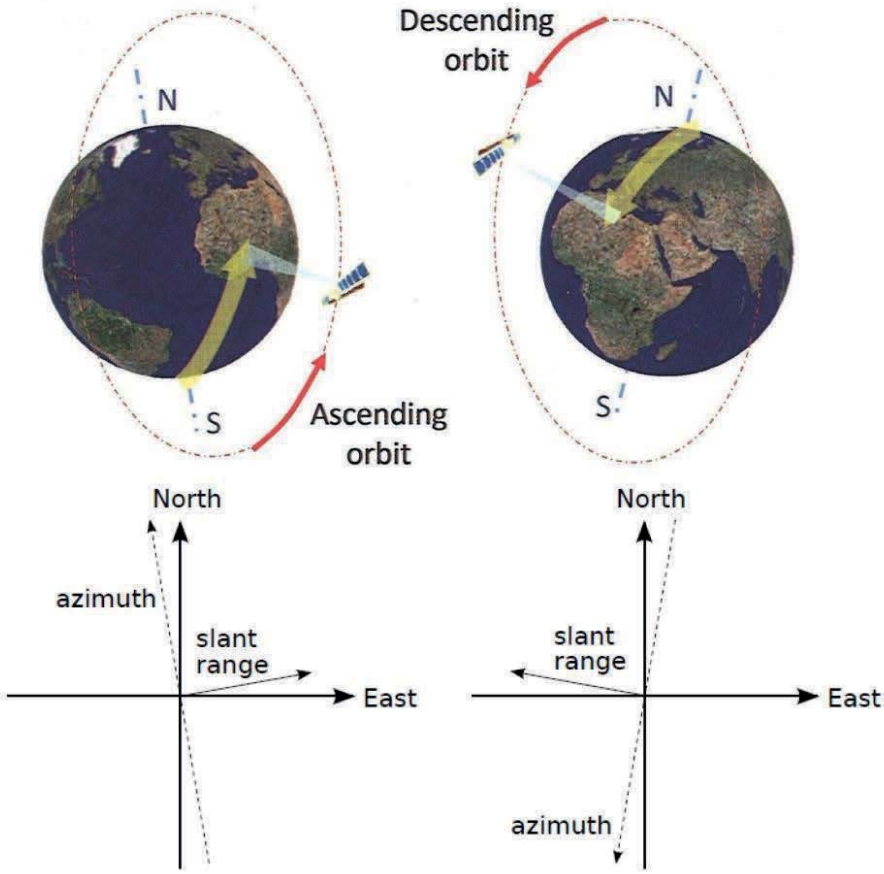

Figure 2: Geometry of ascending (left) and descending (right) satellite orbits. Modified from [Ferretti, 2014; Lauknes, 2010].

2.1.4 SAR GEOMETRICAL EFFECTS

When topographic features exist, SAR images are affected by distortions due to the side-looking geometry of the satellite. *Foreshortening* appears on the slopes facing the radar, resulting in compressed pixels on the ground. The opposite effect gives better resolution on slopes facing away from the radar. For steep-looking spaceborne radar systems, the slant range differences between two points located on foreslopes of mountains are smaller than they would be in flat areas (Figure 3, a'-b'). In the extreme case, *layover* appears when the top of a hill is closer to the radar than the foot of the hill (Figure 3, b'-c' & d'-e'). In this case, the received signal from at least two different altitudes is added into one slant range resolution cell, leading to a very high radar and ambiguous return. The layover effect can easily be observed in SAR images as areas with extremely high intensity. On the other side of the mountain, *shadow* occurs in the area not being illuminated by the radar (Figure 3, c'-d'). To partly overcome this limitation, most modern satellites have the possibility to operate within a range of different incidence angles, while the ERS satellites (which operated between 1991 and 2010), for example, had fixed, relatively steep, incidence angles (21-26°).

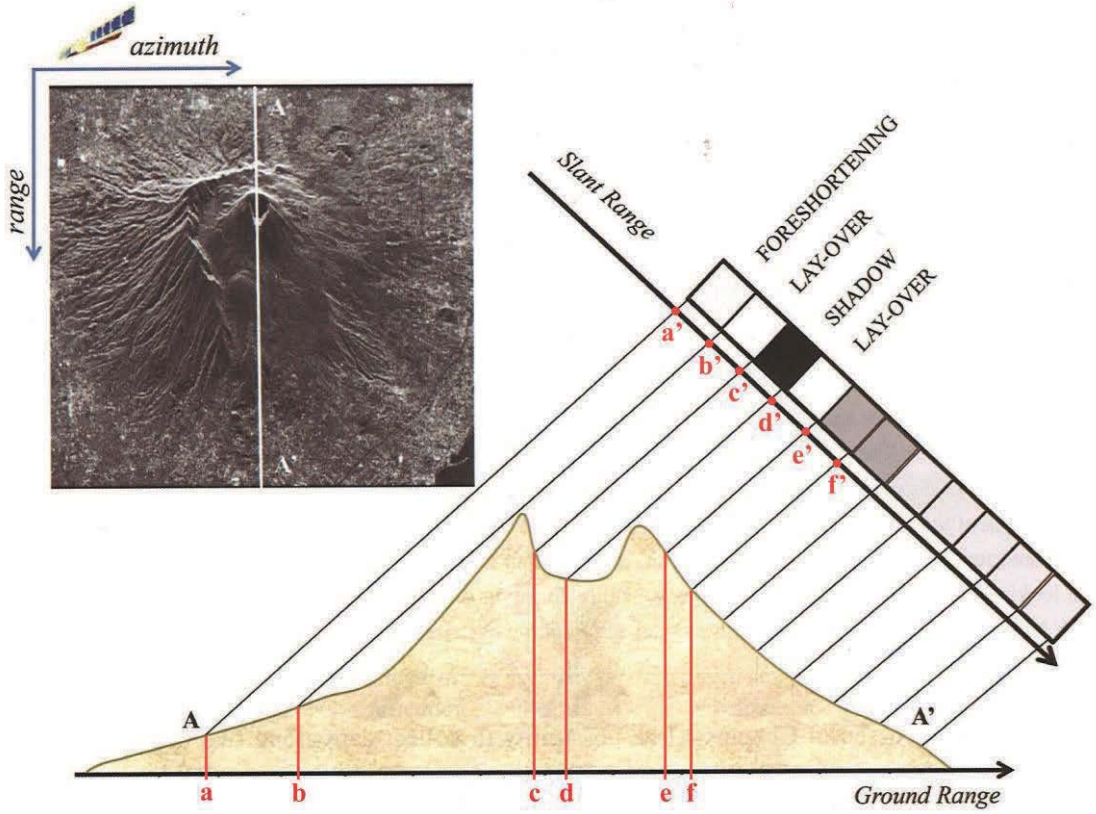

Figure 3: Example of geometric distortions over the Vesuvius volcano (ERS-1 image, 12 April 1996). The analysis of the range line A-A' allows highlighting different effects: foreshortening, layover, and shadowing. They have an impact on the intensity of the backscattered signal since image pixels correspond to terrain patches with different extensions (bright on slopes facing the sensors, dark on slopes facing the opposite direction). Modified from [Ferretti, 2014].

2.1.5 SAR COMPLEX IMAGES

Radar images include both amplitude and phase components. The amplitude gives information on the reflectivity of the terrain, and is related to the amount of the energy backscattering to the receive antenna (Figure 5, a). The phase is a property related to the sensor-target distance, used in SAR Interferometry (InSAR) (see section 2.2).

Because of the sinusoidal shape of radar wave, the sensor-target distance can be expressed as a defined number of wavelengths with an addition of a fraction of a wavelength λ, corresponding to the phase φ. Due to the two-way travel of the wave, the *effective wavelength* is actually $\lambda/2$ (Figure 5).

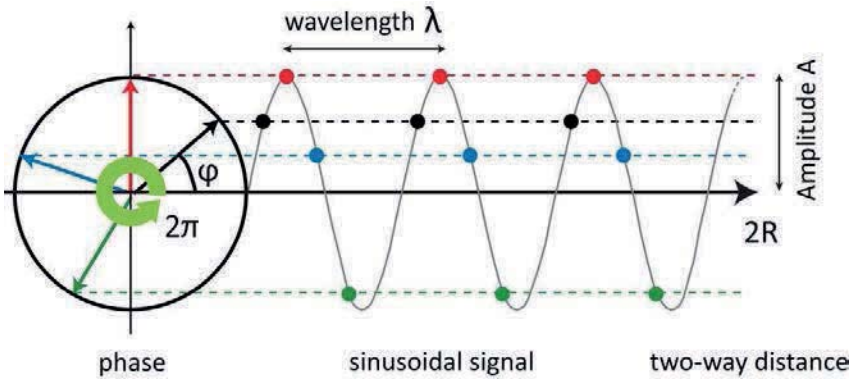

Figure 4: A sinusoidal function sinφ is periodic with a 2π radian period. φ is the phase shift compared to the transmitted signal. Due to the two-way travel of the wave, the effective wavelength is λ/2. Modified from [Ferretti, et al., 2007].

The phase (φ) is thus just a fraction of a wave cycle ranging between 0 and 2π (modulo-2π) that can be related to the slant range (R) by a simple linear equation:

$$\varphi = \frac{2\pi}{\lambda} 2R = \frac{2\pi}{\lambda/2} R = \frac{4\pi}{\lambda} R$$

Looking at Figure 5 (b), the phase information looks like random noise. Actually the phase values of a *single* SAR acquisition have no direct use. The values are uniformly distributed between 0° and 360° due to the superposition of the echoes coming from the multiple reflections on the different parts of the targets within each cell. The combination of the different phase information causes interferences, which create an image affected by speckle noise. We will see in section 2.2 how SAR interferometry is however able to exploit this component.

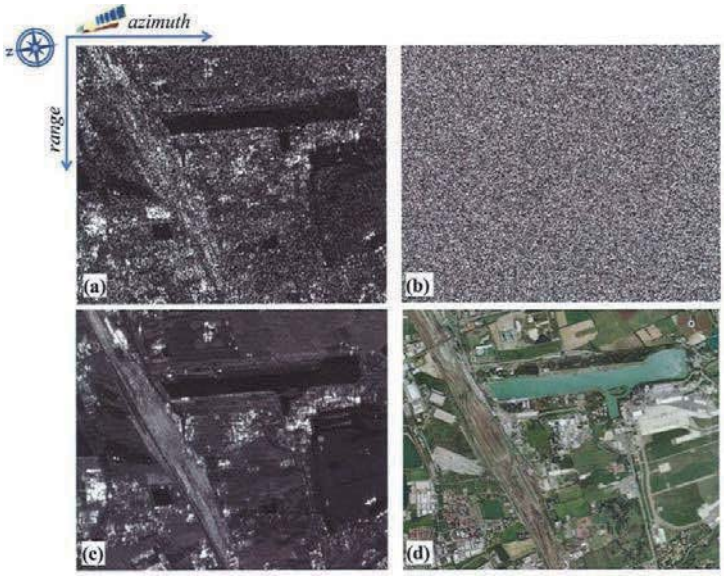

Figure 5: Amplitude (a) and phase (b) values of a ERS-2 SAR image over Milan in January 1997 compared with an optical image of the same area (d). Multi-reflectivity map (c) reduces the noise by averaging the amplitude values of 64 SAR images. From [Ferretti, 2014].

2.1.6 SAR AZIMUTH & RANGE RESOLUTIONS

The spatial resolution in SAR varies according to the sensor and is different in azimuth and range direction. The *slant range resolution* depends on the bandwidth of the sensor. Illuminating beam can be seen as the superposition of a set of sinusoidal signals centred at an operating central frequency of the radar sensor. The bandwidth is the difference between the highest and the lowest frequency of the transmitted signal. Larger is the bandwidth, better is the range resolution. To obtain the *ground range resolution*, the slant range must be projected onto the ground using a simple trigonometric relation depending on the incidence angle. The increase of the incidence angle from near to far range leads to an improvement in the ground range resolution.

Using the Doppler shift due to the movement of the satellite platform, *azimuth resolution* of SAR systems is independent on the distance from the radar to the target. It depends on the length of the antenna in along-track direction. Shorter antennas yield finer resolutions since a single point on the ground will be illuminated for a longer time. Due to various relationships related to the pulse frequency, the velocity of the satellite and the antenna size, a larger coverage will however imply a reduced azimuth resolution.

2.1.7 COMPARISON OF SAR SATELLITES CHARACTERISTICS

Each SAR sensor has its own characteristics that have an impact on the measurement capability (considering movement detection: depending on the direction, the velocity and the size of the moving area), atmospheric penetration and signal stability on different surfaces. A simplified overview of these elements is available in Table 1. The important parameters of some relevant SAR sensors are presented in Table 2 and Table 3.

Table 1: Main SAR satellite sensors characteristics and their influences on measurements.

SAR characteristics	Related to	Impact on
Sensor wavelength	Used frequency band	Detection capability (dep. on the velocity of the moving area), atmosphere penetration & stability on different surfaces
Spatial resolution (ground range & azimuth resolutions)	Bandwidth, antenna length in along-track direction and incidence angle	Detection capability (dep. on the size of the moving area)
Spatial coverage	Antenna size, incidence angle	Size of the potential analysed area
Line-of-sight	Orbit and incidence angle	Detection capability (dep. on the movement direction)
Temporal resolution	Revisit cycle of the satellite	Detection capability (dep. on the velocity on the moving area) & decorrelation

Table 2: Relevant satellite SAR missions, with main sensor parameters. Modified from [Lauknes, 2010].

Mission	ERS-1/2	Envisat ASAR[b]	RADARSAT-1[b]	RADARSAT-2
Country / Agency	ESA	ESA	Canada	Canada
Launch	1991 / 1995	2002	1995	2007
End of life / Mission duration	2000 / 2010[c]	2012[d]	2013	7 yrs (contin.)[e]
Band / Wavelength [cm]	C / 5.66	C / 5.62	C / 6.66	C / 5.55
Incidence Angle [deg.]	21 – 26	20 – 50	20 – 50	20 – 50
Swath width [km][a]	100	56 – 100	45 – 100	20 – 100
Ground range resolution [m][a]	20	12.5 – 28	7.8 – 26	2.8 – 25
Azimuth resolution [m][a]	5	5	8.4	2.1 - 27
Revisit Time [days]	35	35	24	24

Table 3: Relevant satellite SAR missions, with main sensor parameters. Modified from [Lauknes, 2010].

Mission	ALOS-1/2 PALSAR[f]	TerraSAR-X / TanDEM-X	COSMO-SkyMed 1-4	Sentinel-1a/b
Country/Agency	Japan	Germany	Italy	ESA
Launch	2005 / 2014	2007 / 2010	2007-2010	2014 / 2016
End of life / Mission duration	2011 / 7 yrs	5 yrs (contin.)[e]	5 yrs (contin.)[e]	7 yrs
Band / Wavelength [cm]	L / 23.60	X / 3.10	X / 3.12	C / 5.55
Incidence Angle [deg.]	8 – 60	20 – 55	25 – 50	20 – 45
Swath width [km][a]	30 – 70	5 – 100	10 – 40	80 – 400
Ground range resolution [m][a]	10 – 30	0.75 – 16	1 – 15	5 – 25
Azimuth resolution [m][a]	4.5	1.1 - 16	1 – 15	5 – 40
Revisit Time [days]	46	11	4[g]	12 (6)[h]

[a] Significant variations according to the acquisition mode.
[b] Only StripMap mode included.
[c] ERS-2 operating without gyro since January 2001, affecting interferometric applications.
[d] The orbit was changed in October 2010, ending the interferometric time series.
[e] Despite the official life duration, the satellite is still operating.
[f] Only Spotlight and StripMap modes included.
[g] Cluster of 4 satellites with a theoretical 4 days revisit time.
[h] With the addition of Sentinel-1b, the revisit time will be 6 days.

Table 2 and Table 3 highlight the significant variability of the incidence angle, swath width and spatial resolutions, even for a specific sensor. Figure 6 illustrates different operating modes of the new European satellite Sentinel-1.

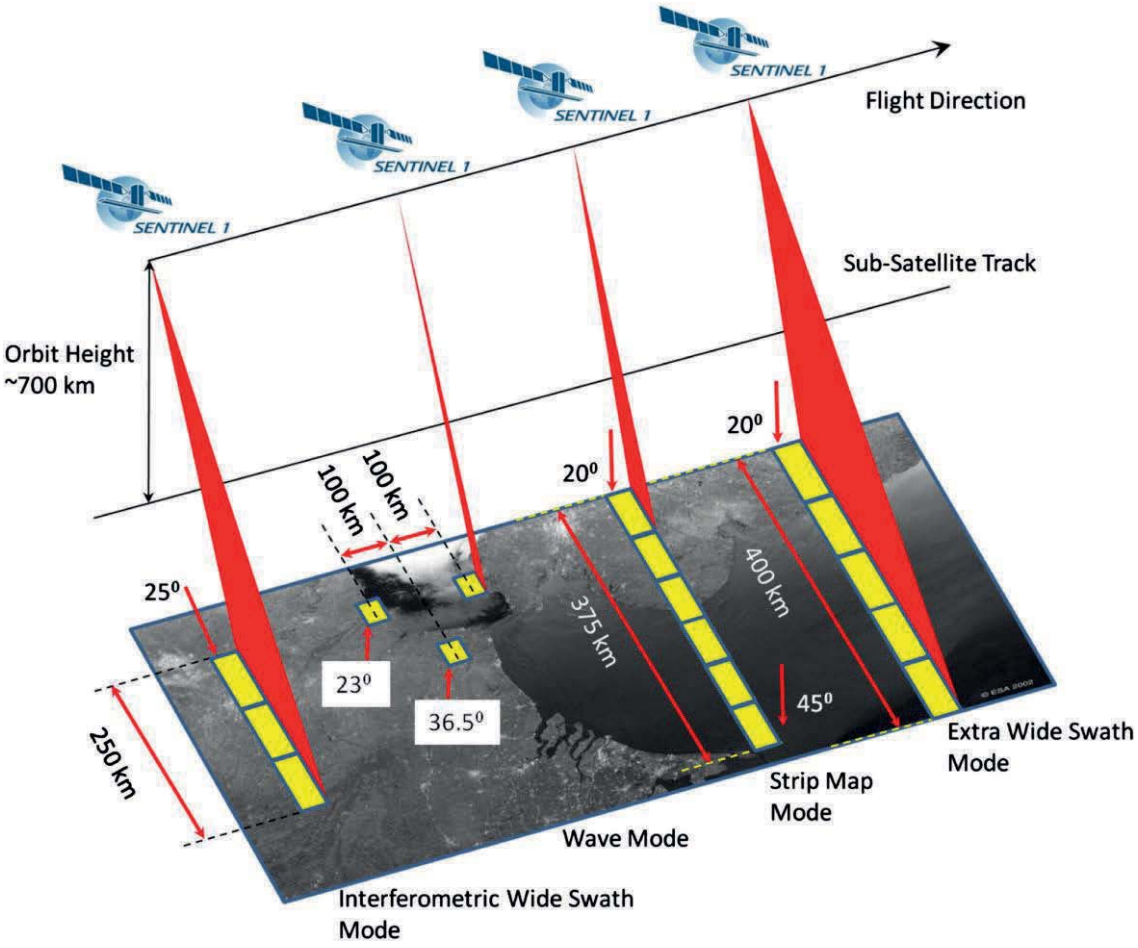

Figure 6: Four Sentinel-1 modes highlighting the high variability of spatial coverage. For each mode, the range & azimuth resolution, as well as the incidence angle vary also. For Norway, the IWS mode will be mainly used. From sentinel.esa.int.

Figure 7 shows examples of SAR images from Envisat ASAR, RADARSAT-2 Ultrafine and TerraSAR-X StripMap mode, with different resolutions. The difference in distinguishable features is obvious. In addition, the impact of the different line-of-sight (LOS) can be highlighted, especially the influence of the incidence angle on the level of radar shadow (both increasing from (a) to (c)).

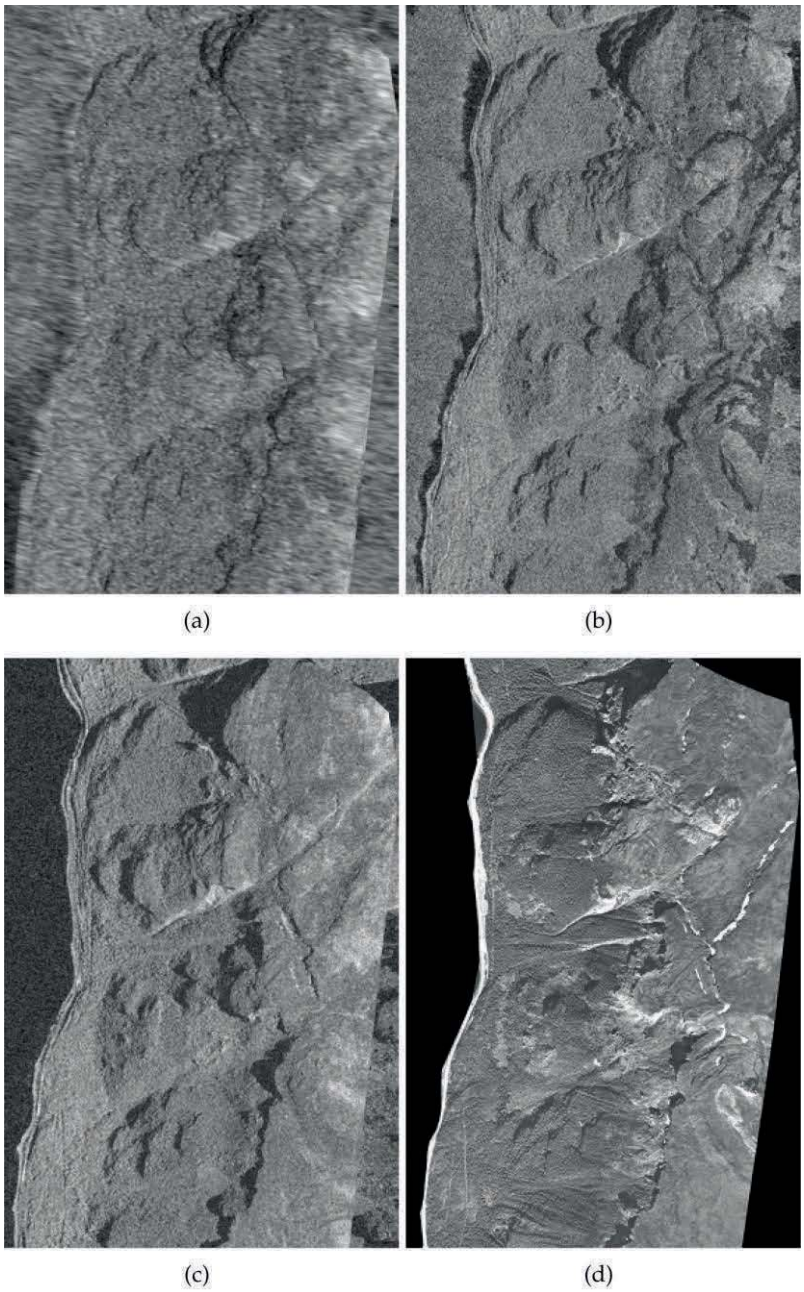

Figure 7: SAR images over Nordnes (Troms, Norway). Images from different sensors illustrating different spatial resolutions. The satellites look toward the West (descending geometry). All images have been geocoded to the same pixel size. (a) Envisat ASAR, (b) RADARSAT-2 Ultrafine, (c) TerraSAR-X StripMap, (d) aerial photo. From [Lauknes, 2010].

2.2 SAR INTERFEROMETRY PRINCIPLES

2.2.1 INTRODUCTION

As discussed in section 2.1.5, the phase information of a single image is not directly usable. However, phase differences between two (or more) different acquisitions are meaningful. This is the main topic of *SAR interferometry (InSAR)*. By computing phase differences between two acquisitions *from two different locations*, it is possible to build a Digital Elevation Model (DEM), while by computing phase changes between two acquisitions *at two different times*, it is possible to detect ground deformation along the line-of-sight (LOS). This is the focus of this report. The methodology has been mainly developed in the 1990's after launch of the ESA (European Space Agency) ERS satellites which triggered a lot of InSAR research activity. In this period, InSAR was successfully used to study surface displacements due to e.g. glacier dynamics [Goldstein et al., 1993], volcano deformation [Massonnet et al., 1995; Amelung et al., 2000], and earthquakes [Massonnet et al., 1993; Massonnet and Feigl; 1998]. More recently the potential of differential InSAR has been investigated to study landslides [Berardino et al., 2003; Hilley et al., 2004; Strozzi et al., 2005; Rott and Nagler, 2006; Colesanti and Wasowski, 2006; Lauknes, 2011].

2.2.2 LINE-OF-SIGHT AND DETECTION CAPABILITY

The analysis of phase changes between two acquisitions at two different times can provide information about ground deformation along the *line-of-sight (LOS)* of the SAR sensor (Figure 8). InSAR is only sensitive to displacements that have a component in the LOS direction, which depends on the flying orientation of the satellite (track) and the incidence angle of the radar beam (see section 2.1.2). Steeper the incidence angles lead to better sensitivity to vertical displacements. Looking toward the West, a descending orbit gives mainly non-distorted coverage in west facing slope, and an ascending covers mainly east facing slopes. Sensitivity is very low in cases where the actual surface displacement vector is near perpendicular to the LOS. Due to the North-South orbit direction, the sensitivity to surface displacement in this plane is near zero.

2.2.3 PHASE CHANGES BETWEEN ACQUISITIONS

Due to the modulo-2π and the effective wavelength $\lambda/2$ explained in section 2.1.5, there is an ambiguity if the phase difference between the two acquisitions is higher than $\lambda/2$. Thus, in practice, for a sensor with a wavelength of 5.55 cm with a revisit time of 24 days (as RADARSAT-2), a moving area with velocity higher than 2.8 cm in 24 days will induce a *phase ambiguity*.

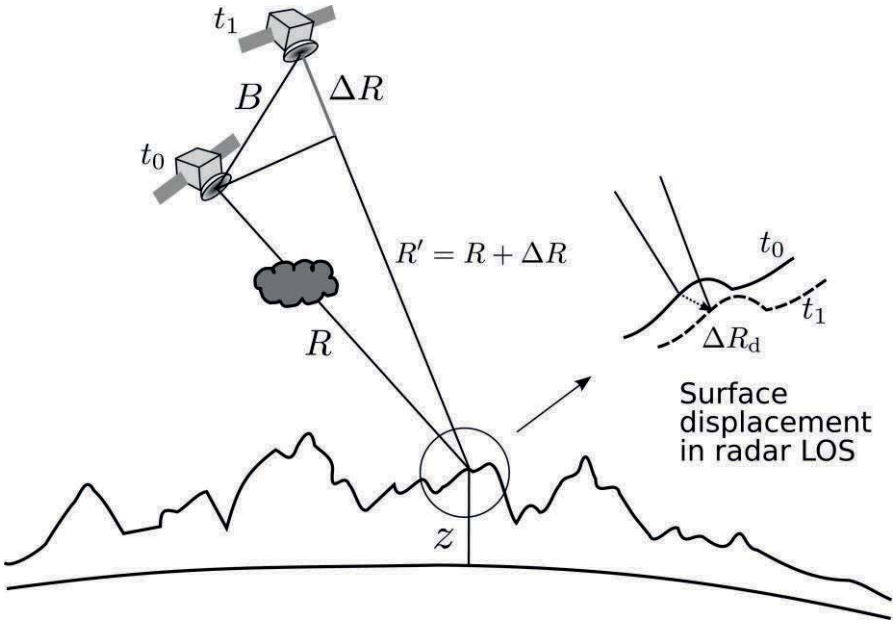

Figure 8: Detecting surface displacement with InSAR. An area on the ground is imaged at two different time t_0 and t_1. A potential surface deformation occurring between the acquisition times will lead to an interferometric phase term ΔR_d. The cloud at the acquisition t_0 illustrates that atmospheric effects can affect the radar propagation producing an additional path delay. From [Lauknes, 2010].

Moreover, terrain deformation is only one of the components of the phase difference. In addition, *the topographic component* due the distance between two orbits (called baseline and expressed as B in Figure 8), the *atmospheric effects* and other noise contributions has to be taken into account. The interferometric phase difference can thus be expressed as [Berardino et al., 2002]:

$$\Delta\varphi = \frac{4\pi}{\lambda}\frac{B_\perp}{Rsin\theta}z + \frac{4\pi}{\lambda}\Delta R_d + \Delta\varphi_{APS} + \Delta\varphi_{decorr}$$

where λ is the radar wavelength, z is the elevation of the target point above a reference plane, $B_\perp$ is the distance between the two orbits (perpendicular baseline), ΔR_d is surface displacement along the LOS, R is the slant range distance, θ is the incidence angle, $\Delta\varphi_{APS}$ is the difference in atmospheric path delay (atmospheric phase screen APS), and $\Delta\varphi_{decorr}$ is a term including other noise contributions / decorrelation sources.

In order to study surface displacements, the topographic contribution has to be removed. This is most often done by using an external high-precision Digital Elevation Model (DEM). The removing of atmospheric effects is one of major issue of InSAR processing that will be discussed in section 2.3.

Figure 9 shows an example of an *interferogram* between two ENVISAT ASAR acquisitions in 2003-2004. The results highlight the co-seismic displacement field originating from an earthquake in Bam, Iran. The values are expressed in modulo-2π (-π to + π) corresponding to λ/2 (28 mm or -14 to 14 mm). This interferogram is thus

wrapped, highlighting a succession of patterns called *fringes*. In section 2.3, we will show how to convert these cyclic phase differences to absolute phase differences and thus continuous distance differences (unwrapping procedure).

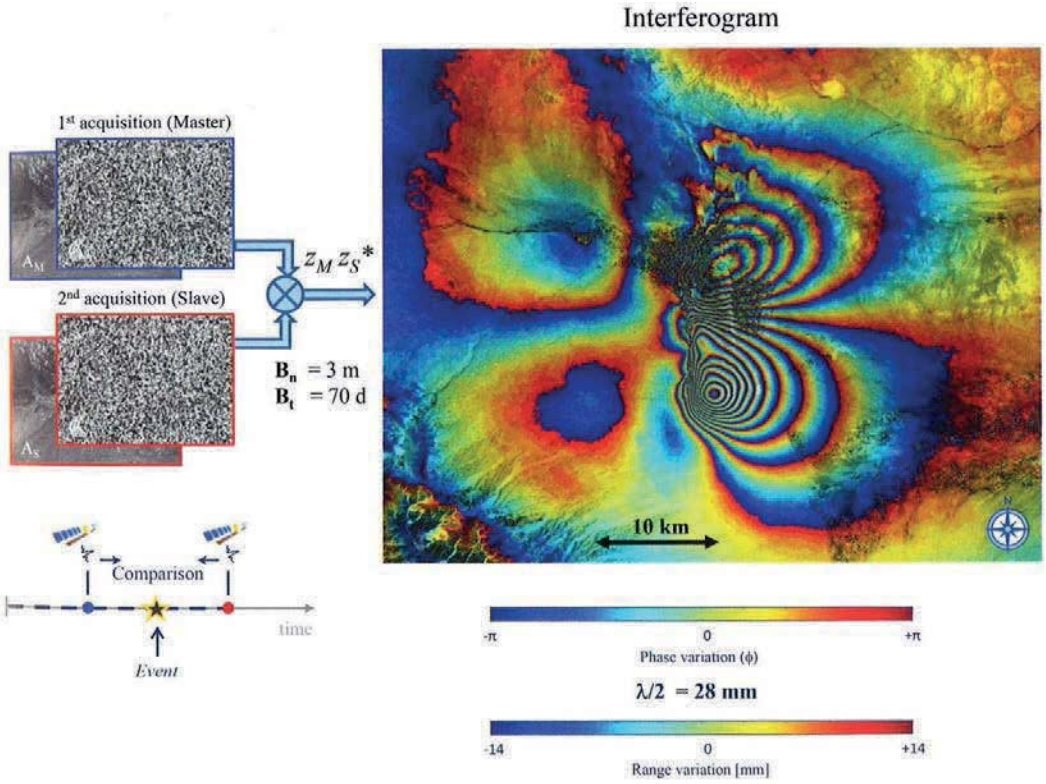

Figure 9: Example of SAR interferogram using images from Envisat ASAR sensor ($\boldsymbol{\lambda/2}$ = 28 mm) with a small perpendicular or normal baseline B_n of 3 m, a descending orbit and a look angle of 23 deg. The area of interest is in south-eastern Iran, where the town of Bam was devastated on 26 December 2003 by an earthquake. The first image was acquired on 3 December 2003 and the second on 11 February 2004 (70 days of time interval or temporal baseline B_t). The results highlight the co-seismic displacements field originating from the earthquake. From [Ferretti, 2014].

2.2.4 INSAR COHERENCE AND DECORRELATION

The phase accuracy in SAR interferometry is mainly affected by phase noise and decorrelation. Phase decorrelation is due to changes in position of individual scatters within the resolution cell and is one of the main limitations for successful use of InSAR. Decorrelation is mainly due to either SAR imaging geometric effects (*spatial decorrelation*), or temporal backscattering changes (*temporal decorrelation*).

Spatial decorrelation is related to the spatial baseline between the sensor at the different acquisitions. Temporal decorrelation is due to changes in geometrical or electrical properties of the surface, as function of time between the acquisitions. These changes may be caused e.g. by moving parts of vegetation, erosion on the land surface, or agricultural activity. Forest is shown to have a generally low phase correlation, even for a short temporal baseline, while urban and arid areas show usually high signal stability

even for acquisition time intervals longer than one year. Terrain containing variable liquid water, such as e.g., areas covered with wet snow, will also have different scattering properties from one observation to the next. Thus the scenes acquired during winter season can be unusable if snowfall occurs. To overcome this limitation, artificial corner reflector can be installed to monitor areas of interest during the whole year (Figure 10).

The temporal decorrelation phenomenon is dependent on the radar wavelength; longer wavelengths are less sensitive to small scale surface scattering changes, however with reduced sensitivity to displacement.

A quality measure of the interferometric phase is the complex correlation coefficient, or *complex coherence* $|\gamma|$. The values of $|\gamma|$ are between 0 and 1, where a coherence value of 1 corresponds to perfect phase correlation between the two measurements. Coherence values less than unity correspond to reduced phase correlation (Figure 11).

Figure 10: Overview of installation of a corner reflector in Troms County. The reflectors provide stable signal, and are covered to prevent snow accumulation.

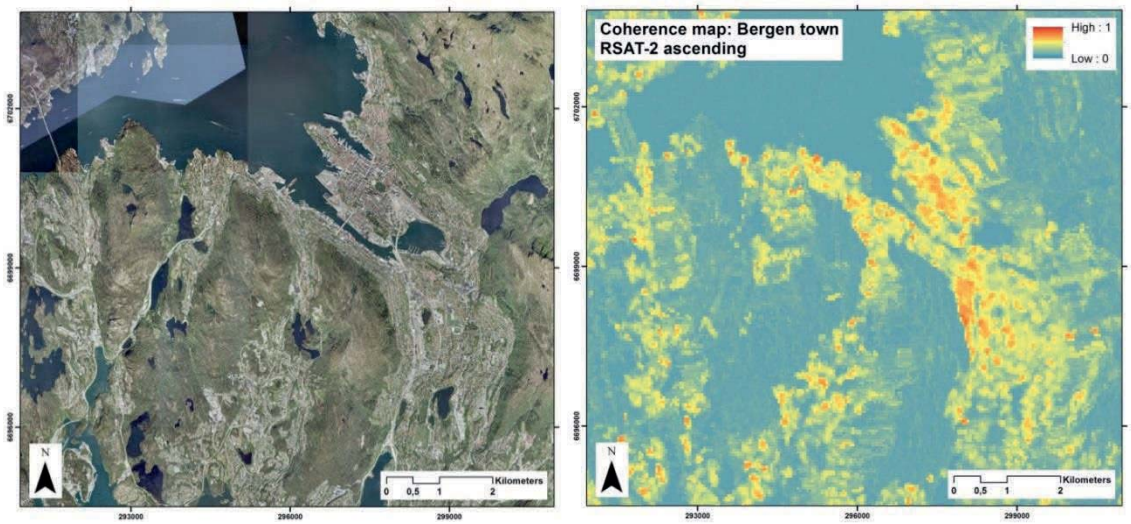

Figure 11: Example of coherence map over Bergen. It clearly appears that the urban area has high coherence values (yellow-red), while the areas with vegetation or water are affected by low coherence (blue).

2.3 INSAR PROCESSING AND RESULTS

InSAR processing involves many steps. Irrelevant phase components have to be removed (section 2.3.1) and wrapped interferograms have to be converted into unwrapped interferograms representing continuous distance variations (section 2.3.2). To overcome the main InSAR limitations, different multi-interferograms techniques were developed in the last decades and the main will be presented in section 2.3.3. The focus is on the main steps and methods included in the GSAR processing chain developed at Norut [Larsen et al., 2005].

2.3.1 PROCESSING OF PHASE COMPONENTS

The challenge in InSAR is to separate the wanted signal (e.g. deformation or topography) from the sum of all phase contributions. For terrain displacement studies, temporal decorrelation can be considered as a random noise source, while errors in the DEM used to remove the topographic phase, orbital errors, and atmospheric changes will introduce a spatially correlated phase error contribution.

To illustrate the effects of some phase components, it is useful to consider first some ideal cases where noise and atmospheric effects are negligible. In Figure 12, the case (a) shows an interferogram built with two acquisitions at different times but made at the exact same location (perpendicular baseline = 0) and without topographic contribution. If no deformation occurred between the two scenes, the phase difference will be zero over the whole interferogram. In the case (b), the perpendicular baseline is still zero and the terrain flat but a deformation occurred between the two scenes, highlighting a pattern in the middle of the interferogram. In the case (c), the area is not affected by ground deformation but a difference between the two orbits is introduced (non-zero perpendicular baseline). This creates a succession of fringes in the range direction. Finally, in the case (d), topographic features are added to the scenario (c). This adds an additional phase component which has to be removed in case of terrain displacement studies.

In addition, we have to take into account the *atmospheric effects*. A radar interferometer measures the phase difference with accuracy on the order of a fraction of the wavelength; more than accurate enough to be influenced by atmospheric path delay. Phase propagation delay due to atmospheric variability is one of the main error sources in repeat-pass InSAR. It is common to divide the atmospheric path delay into one component coming from *turbulent mixing processes*, and a *stratified component correlating with elevation*. Turbulent mixing comes from mixing processes in the inhomogeneous atmosphere, while stratification results from variations in the vertical refractive index profile. The second is correlated with the local topography. Figure 13 shows how atmospheric components as well as a phase noise contribution can affect an interferogram. The atmospheric effects are temporally uncorrelated but spatially correlated, contrary to noise components. In Figure 13 (d), an interferogram combining

the different phase components is presented. It includes *ground deformation component* from Figure 12 (b), *baseline-related component* from Figure 12 (c), *topographic component* from Figure 12 (d), *atmospheric effects* from Figure 13 (a) and (b) and *noise* from Figure 13 (c).

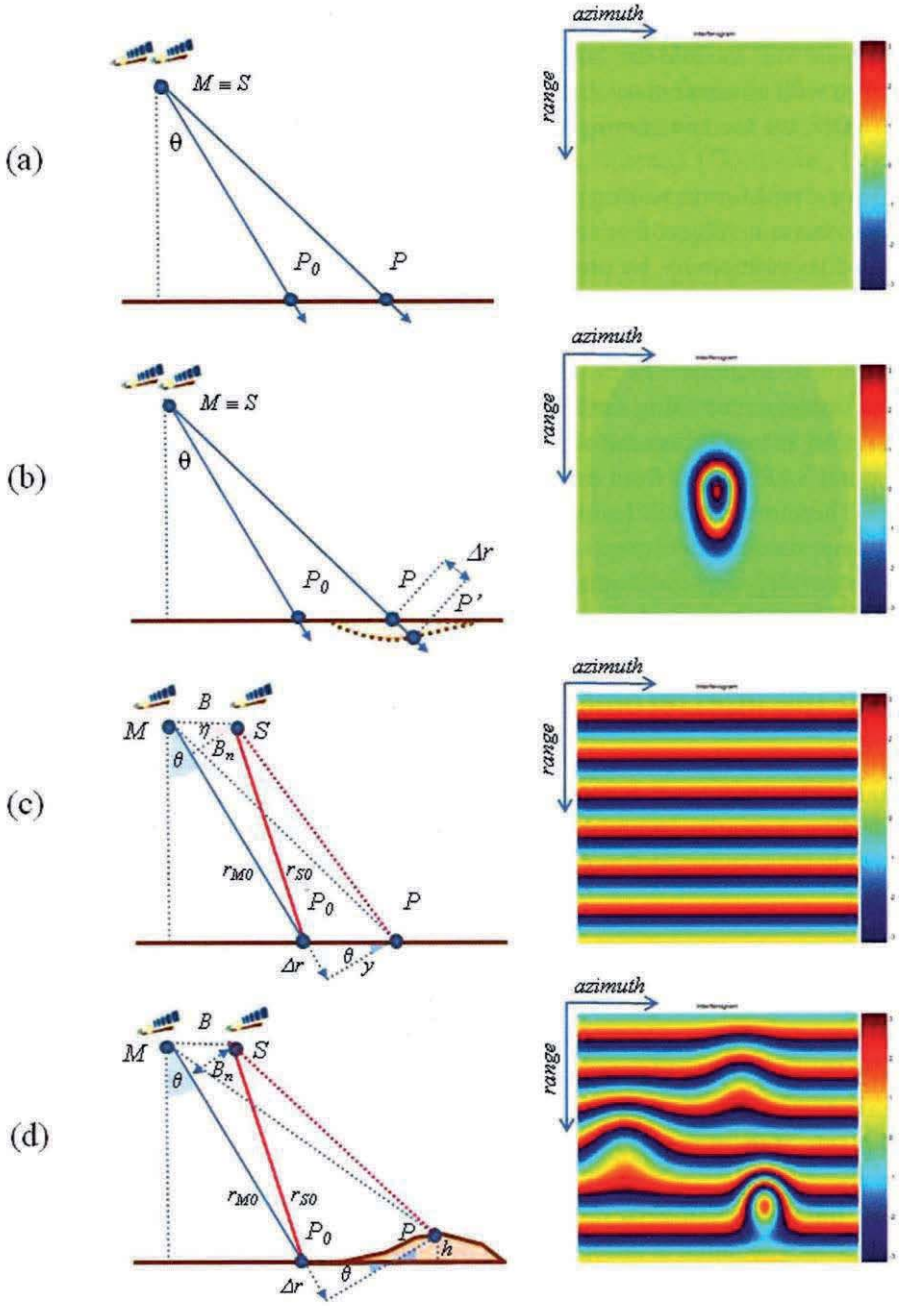

Figure 12: Examples of InSAR configurations and resulting interferograms. (a) Same acquisition geometry, flat area, no atmospheric effects and no ground deformation. (b) Same acquisition geometry, flat area, no atmospheric effects but ground deformation. (c) Flat area, no atmospheric effects and no ground deformation, but different acquisition geometries (perpendicular baseline ≠ 0). (d) No atmospheric effects and no ground deformation, but topographic and baseline-related components. From [Ferretti, 2014].

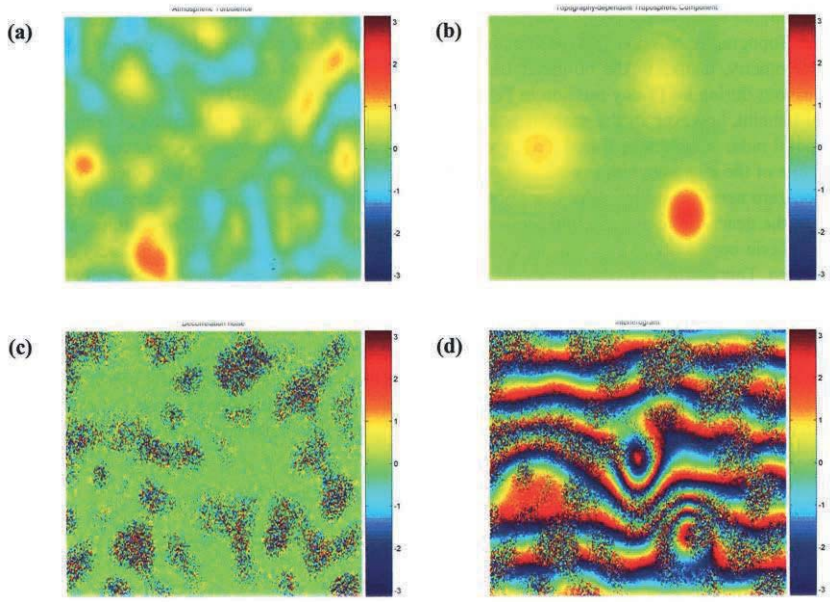

Figure 13: (a) Example of atmospheric turbulence effects on a SAR interferogram. (b) Example of stratified component related to the same topography as Figure 12 (d). (c) Example of noise contribution affecting an interferogram. (d) Final example combining the different phase contributions presented in Figure 12 (b)-(d) & Figure 13 (a)-(c). From [Ferretti, 2014].

2.3.2 UNWRAPPING PROCEDURE

A wrapped interferogram is composed by a succession of fringes when the phase exceeds half the wavelength. The process of restoring the correct multiple of 2π to each point of the interferometric phase image, or with easier words to convert cyclic phase difference into continuous phase difference is called *phase unwrapping* (Figure 14, top). The procedure uses the assumption that the true displacements field has a spatial continuity and thus the neighbouring pixels are supposed to be within a phase cycle of the others. Using a reference point (with high coherence and if possible known as stable or with a known deformation rate), the phase differences are thus spatially integrated using different methods according to the chosen algorithm.

This highlights three potential issues:

- InSAR data are not absolute but *relative to a reference point* that has to be chosen carefully. If the reference point supposed to be stable is in reality moving, the whole dataset will be affected by a shift of values.
- If we use interferograms formed using large temporal or spatial baselines, areas can be decorrelated due to changes in scattering properties within the resolution cell between the two acquisitions. Such decorrelation effects can contaminate large areas in the interferograms and create discontinuous coherent patches. This makes the retrieval of absolute phase a very challenging task.
- If the movements are spatially discontinuous, for example in the case of localized quick event, the procedure can fail to retrieve correct solutions.

Thus, this step is one of the most challenging aspects for successful applications of SAR interferometry.

In Figure 14 (bottom), an example of wrapped and corresponding unwrapped interferogram is presented. The parts affected by decorrelation effects (areas under an applied coherence threshold, in white on (d)) are in this case small.

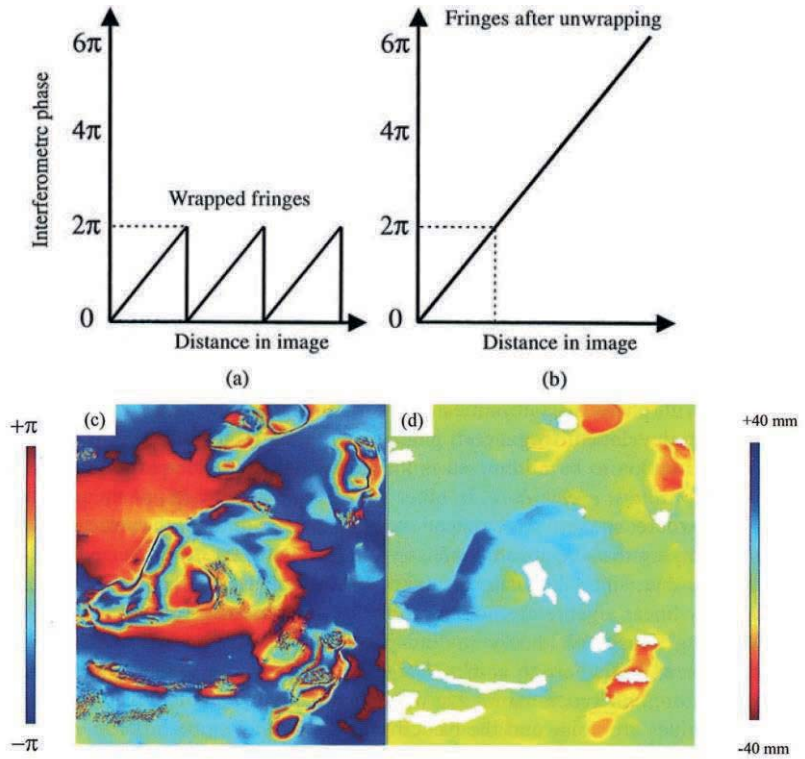

Figure 14: Top: Principle of the unwrapping procedure. (a) Representation of a slice through some fringes on an interferogram. The results are wrapped around 2π. (b) The absolute phase is found after an unwrapping procedure. From [Woodhouse, 2006]. Bottom: Example of wrapped interferogram over an open pit mine in USA (c) and the corresponding unwrapped interferogram (d). From [Ferretti, 2014].

2.3.3 MULTI-INTERFEROGRAM TECHNIQUES

Multi-interferograms techniques were developed over the last decades in order to overcome most of the limitations of the standard single interferogram approach, as temporal and geometric decorrelations, atmospheric effects, etc. They are generally divided into two main groups:

- Methods based on locating *Persistent Scatterers* (PSs), referred to as *Persistent Scatterer Interferometry* (PSI) methods [Ferretti et al., 2000; Ferretti et al., 2001; Colesanti et al,. 2003; Werner et al., 2003; Hooper et al., 2004; Kampes, 2006; Prati et al., 2010].
- Methods based on spatial correlation and *distributed scattering* (DS), referred to as *Small BAseline Subset* (SBAS) methods [Lundgren et al., 2001; Berardino et al.,

2002; Mora et al., 2003; Schmidt and Bürgmann, 2003; Lanari et al., 2007; Prati et al., 2010; Sansosti et al., 2010; Lauknes, et al. 2011].

The two methods refer to the different scattering mechanisms that can be expected from a pixel under study (Figure 15). A coherent point-like target is a scatterer that dominates the scattering from the resolution cell. Due to the broad scattering lobe, point targets are visible from a large span of viewing angles. A Persistent Scatterer (PS) is a target whose amplitude and phase is quite constant as a function of time. If a pixel includes one scatterer that is brighter than the other ones, the pixel phase variance is significantly reduced with respect to the case of distributed scattering from a high number of point targets (Figure 15, top). A PS can be the corner of a building or a rock formation in rural areas. For a distributed scattering mechanism, the measured scattering is the coherent summation of all individual small scatterers within the resolution cell.

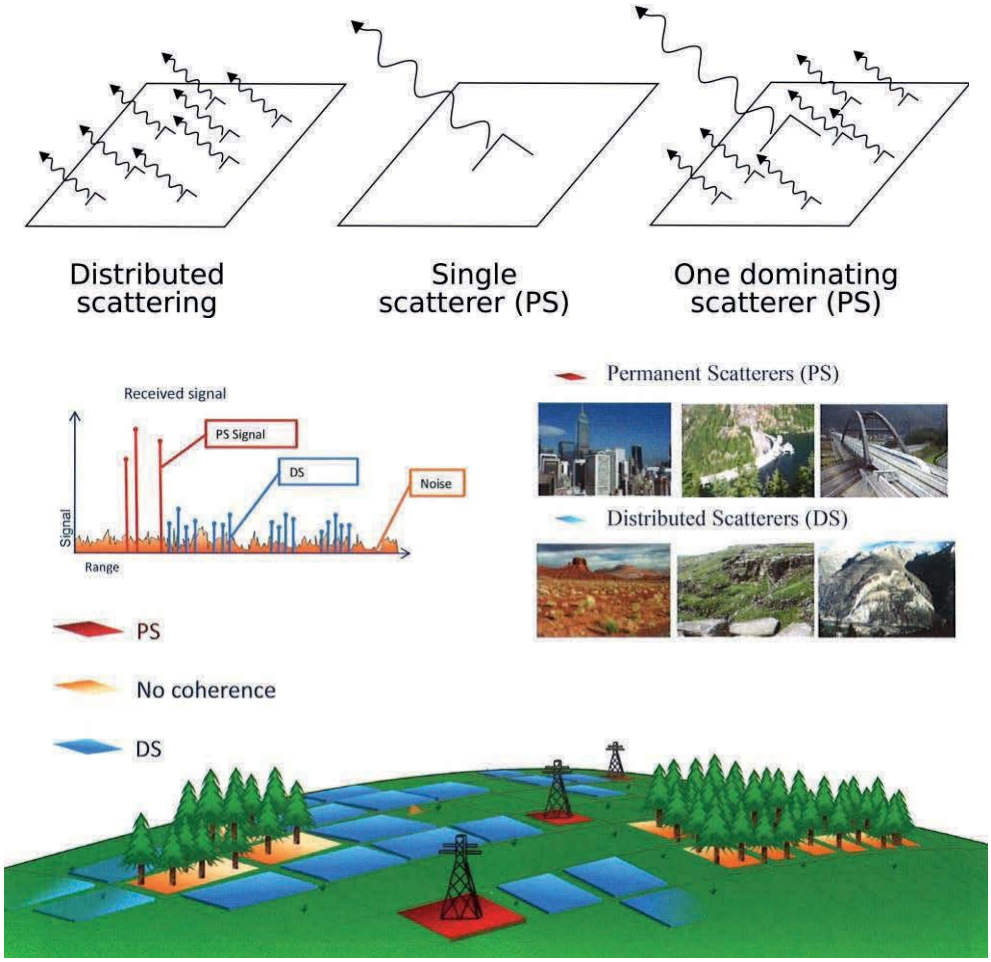

Figure 15: Different surface scattering mechanisms. Top: a pixel with distributed scattering (DS) mechanism (top, left), a dominating point scatterer (top, middle), and a pixel with one scatterer that is brighter than all other (top, right). The phase dispersion for the PS pixels is much smaller than for distributed scattering pixels. From [Lauknes, 2011; Ferretti, 2014].

2.3.3.1 PERSISTENT SCATTERER INTERFEROMETRY (PSI)

PSI methods uses a stack of interferograms generated with the same master scene (Figure 16, left) to analyze the temporal phase evolution of individual coherent point scatterers (Figure 16, right) [Ferretti et al., 2000; Ferretti et al., 2001]. All interferograms are computed at full resolution and all interferometric combinations are employed, even those exceeding the critical baseline. The generated interferograms are often severely decorrelated. However, by searching for pixels that include a stable scatterer over long time intervals, a network of so called Persistent Scatterers can be established, where displacement signal and 3D scatterer position can be resolved. The PS can be selected looking at *amplitude dispersion* below a defined threshold. Such a statistical measure requires a large stack of images.

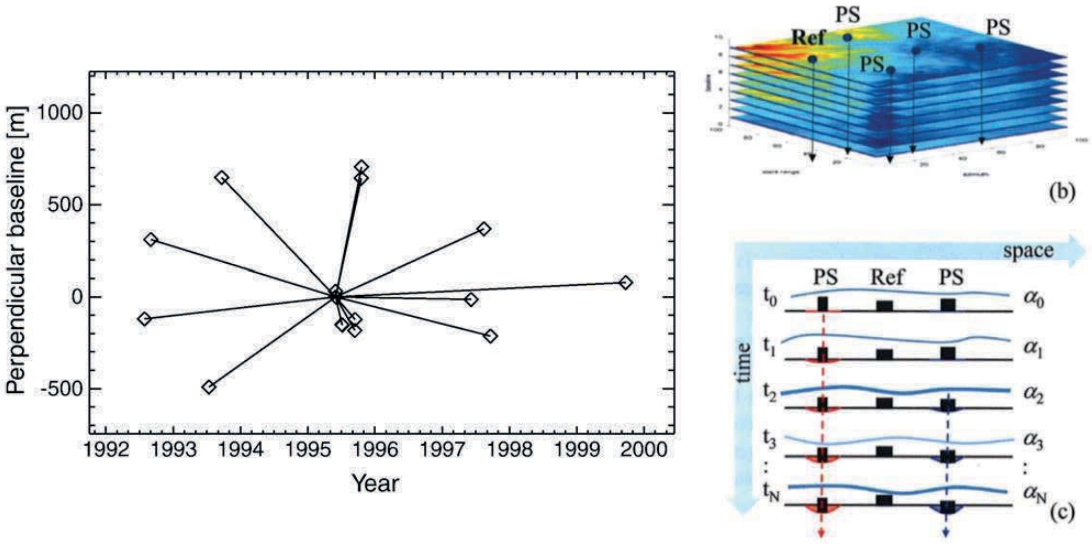

Figure 16: Left: PS baseline plot (perpendicular baseline vs. acquisition time). The master scene is 1995-06-02. Each line corresponds to an interferogram between two acquisition dates. From [Lauknes, 2010]. Right: PSI analysis of a stack of multi-temporal SAR acquisitions using a sparse PS grid rather than the analysis of all image pixels. From [Ferretti, 2014].

PSI procedure includes two networks of Persistent Scatterers. The first PS network is built using a sparse grid of very highly stable targets (low amplitude dispersion) in order to remove irrelevant components such as atmospheric effects. Using a large stack of interferograms (Figure 16, b) and based on the assumption that atmospheric component is spatially correlated but uncorrelated in time, the APS (Atmospheric Phase Screen) is estimated, interpolated and subtracted from each interferogram. The second PS network is built applying a new amplitude dispersion threshold (higher). For each selected PS mean velocity and time series are calculated (Figure 16, c).

2.3.3.2 SMALL BASELINE SUBSET METHOD (SBAS)

Similar to PSI, SBAS method uses a stack of interferograms to remove or reduce the effects of irrelevant phase components. However, it incorporates a larger number of interferograms, not from a unique master scene as for PSI (Figure 17, left) [Berardino, et al. 2002]. Spatial and temporal baselines below chosen thresholds are applied in order to reduce geometric and temporal decorrelation, as well as the effects due to errors in the used DEM. Moreover, a complex *multilooking* procedure is applied at the beginning of the processing chain. This reduces the spatial resolution, but improves the signal quality of pixels characterized by distributed scattering (Figure 17, right).

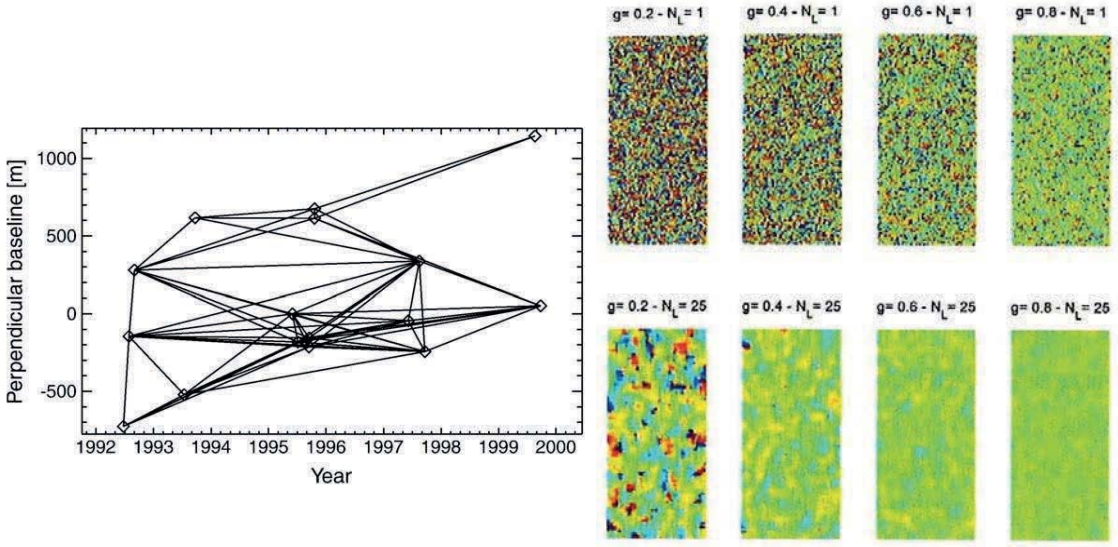

Figure 17: Left: SBAS baseline plot (perpendicular baseline vs. acquisition time). Each line corresponds to an interferogram between two acquisition dates [Lauknes, 2010]. Right: Effect of complex multi-looking $N_L = 25$ (square 5x5 window) on wrapped phase values with different coherence levels (0.2 - 0.8). Modified from [Ferretti, 2014].

In order to provide a mean velocity map with reduced atmospheric noise, short baseline interferograms can be simply averaged and weighted by the temporal differences between the scenes. This refers to the *stacking method* [Gabriel et al., 1989; Sandwell and Price, 1998; Peltzer et al., 2001]. *SBAS models* were later developed in order to take into account the temporal evolution of the deformation and provide complete time series [Berardino, et al. 2002; Pepe et al., 2011; Lauknes et al., 2011].

2.3.4 INSAR OUTPUTS

Different InSAR results can be produced. The most common output is a *deformation map* over the area in interest. The map can display the annual mean velocity as in Figure 18 or specific displacements between two defined times when mean velocity value does not make sense (by example displacements between June and September 2012 if the stack uses only snow-free scenes in a mountainous region). As discussed above, according to the processing method, each element of the map will represent a selected

Persistent Scatterer below a defined amplitude dispersion threshold (for PSI, as in Figure 18, top) or a multilooked pixel above a defined coherence threshold (for SBAS, as in Figure 18, bottom) for the area visible from the satellite (without shadow) and unaffected from geometrical distortions (without layover). For each selected PS or SBAS pixel, *time series* usually displayed on a displacement/time graph can be extracted (Figure 18, bottom). These two outputs allow providing complementary information about the spatial distribution of the movement and its temporal evolution. In addition, derived products such as *coherence map*, *intensity map*, *shadow mask*, *layover mask* can be generated.

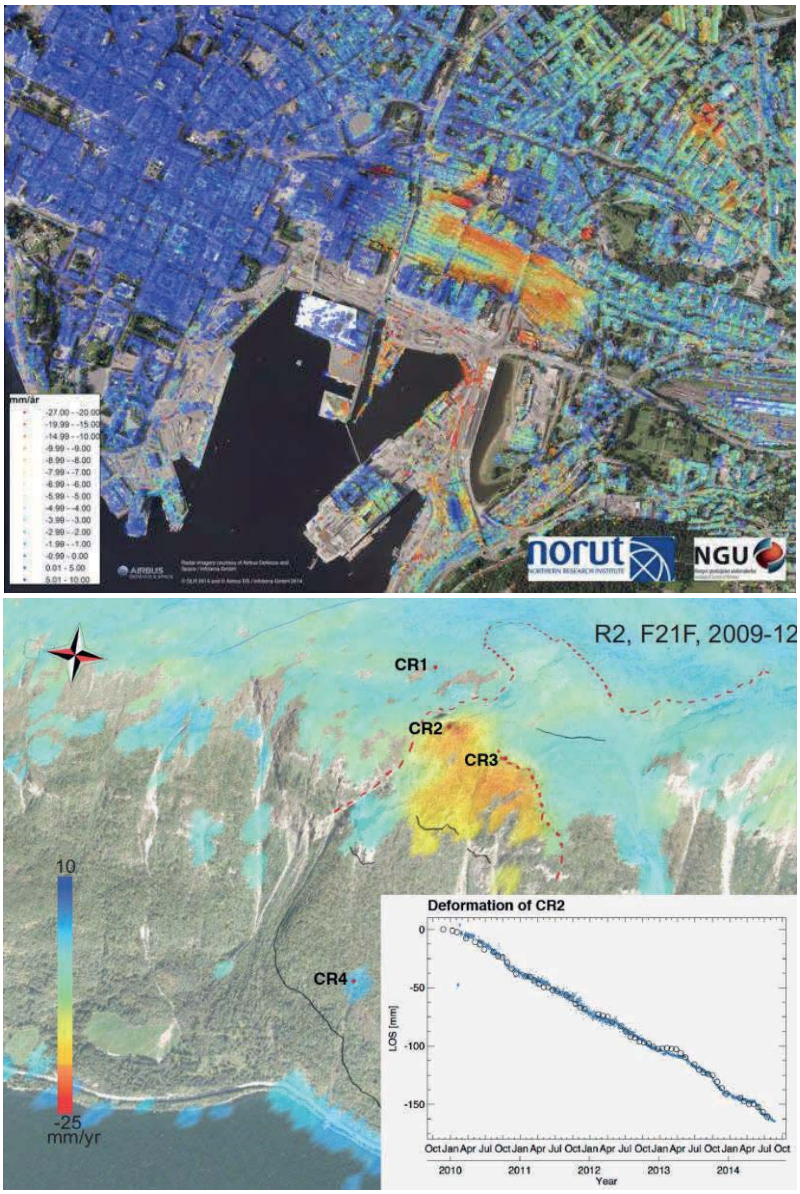

Figure 18: Top: Example of InSAR mean velocity map over Bjørvika (Oslo) from PSI processing using TerraSAR-X data supplied by Airbus Defense & Space (Infoterra GmbH). Bottom: Example of InSAR mean velocity map over Nordnes rockslide (Troms County, Norway) from SBAS processing using RADARSAT-2 images and InSAR time serie (white circles in the graph) compared to DGPS continuous measurements (blue dots in the graph).

It should be reminded that the results are relative to a reference point and the satellite is only able to measure *1D displacement* along its LOS. However, having available data from different acquisition geometries over the same area, it is possible to retrieve *multi-dimensional information*. In practice, using satellites data only, due to the near-polar passes of all the SAR sensors, two geometries (ascending/descending) are available, allowing only a 2D decomposition (vertical/horizontal components in the East-West LOS-plane). An example over Nordnes rockslide (Troms region) is presented in Figure 19.

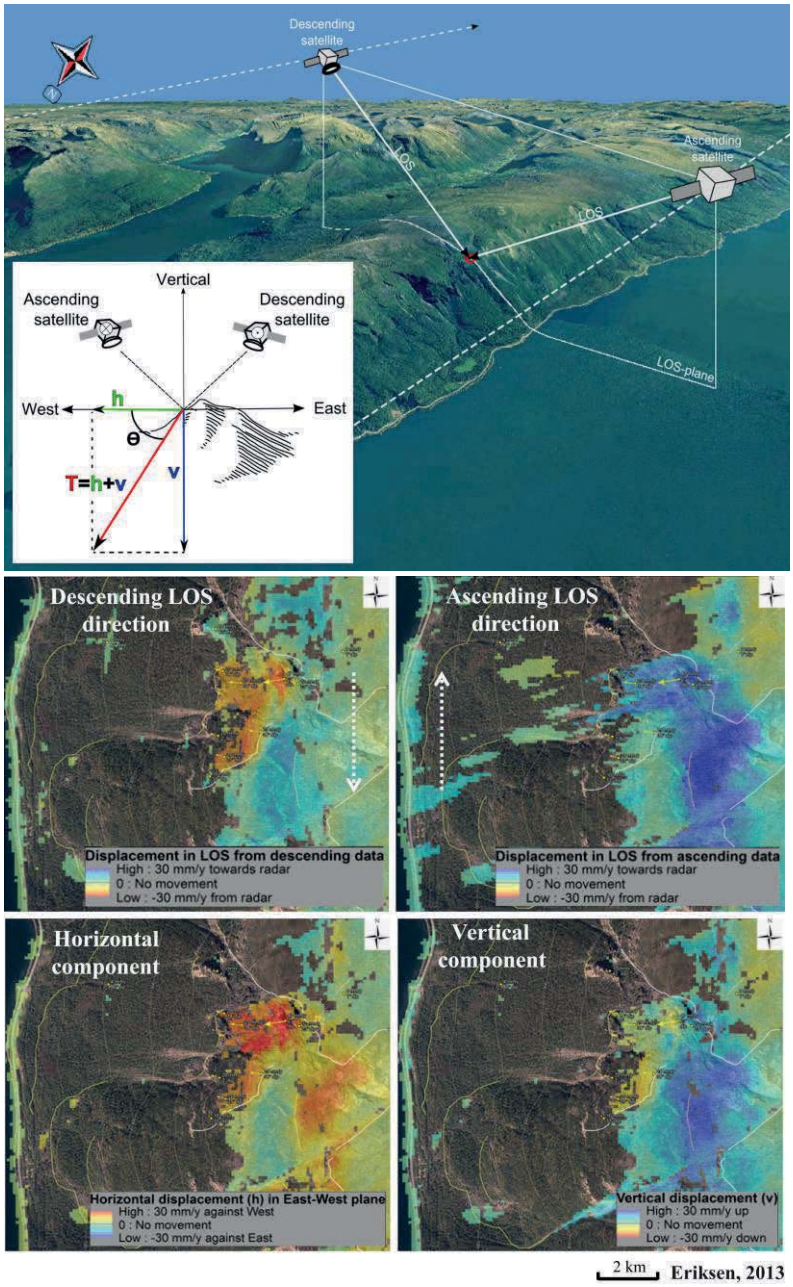

Figure 19: Top: Principle of 2D decomposition using ascending and descending geometries over Nordnes rockslide. Bottom: Examples of mean velocity maps along the LOS using data (approximate satellite paths display with dashed white arrows) and after horizontal/vertical decomposition. From [Eriksen, 2013]. TSX data used © DLR (2009-2014).

3 STUDY AREA

After discussion between the partners of the projects, it appeared that Bergen area including the town and various sectors located within 100 km toward the East is an interesting case-example to illustrate the potential of InSAR technology for ground deformation detection. In section 3.1, the natural hazards context of the region is introduced, as well as the main sectors of interest highlighted by Norges vassdrags- og energidirektorat (NVE), Statens vegvesen and Jernbaneverket. In section 3.2, the main characteristics of the available satellite data are presented.

3.1 HAZARDS CONTEXT

3.1.1 EVENTS INVENTORY

Bergen area is interesting for its natural hazards context. Looking at the inventory of the historical events, it clearly appears that the natural hazards are a significant issue for the management of infrastructure and the safety of population in this region (Figure 20).

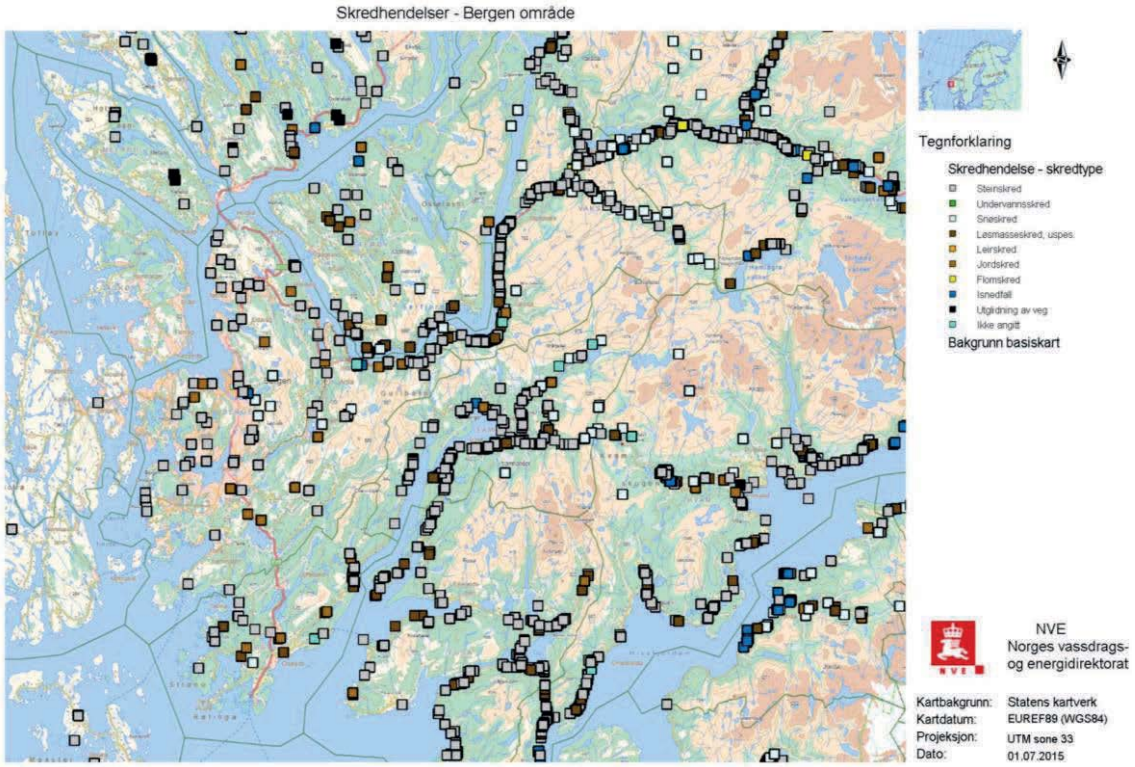

Figure 20: Extract of the inventory of natural hazards events in Norway: rockfalls (gray), landslides (brown), debris flows (yellow), roads deterioration (black), avalanches (white), icefalls (dark blue), unspecified (turquoise). From www.skrednett.no (download: 07-01-2015).

Unsurprisingly the main clusters of registered events are located along the main infrastructure in areas characterized by significant relief. The density is especially high along the E16 road from Arna to Evanger via Dale (top-right part of the Figure 20), as well as around the NE part of Samnagerfjorden (Årland, Haga) and over Kvamskogen (middle of the Figure 20). It appears that most of the events are classified as rockfalls, landslides or avalanches.

3.1.2 FOCUS OF THE STUDY

The project description highlighted three main areas covered by the available datasets and interesting because of the density of events and the importance of infrastructure (roads and rail).

They are located within an approximate 50 km distance around Bergen:

- E16 and rail Arna-Dale, eventually to Evanger (and also on the other side of the fjord, along the south part of Osterøy);
- Fv7 over Kvamsskogen, especially around Norheimsund (Tokagjelet);
- The area at the head of Samnangerfjorden.

These are covered at least by one of the available satellite dataset. However, due to several limitations regarding to the characteristics of the datasets (see section 3.2) and the region (see sections 4.1 & 4.2), the main focus of the ground deformation analysis will be placed on the western part of the region including Bergen and Indre Arna (see sections 4.3.1 & 4.3.2).

3.2 SATELLITE DATA CHARACTERISTICS

The results presented in Chapter 4 are based on the analysis of three different datasets from two sensors: RADARSAT-2 (RSAT-2) and TerraSAR-X/TanDEM-X (TSX/TDX). The results using the second sensor are from [Cetinic, et al., 2015 (in prep.)]. The main differences between the two satellites can be found in Table 2 and Table 3 (section 2.1.7). The most important elements to take into account are the frequency band and corresponding wavelength (C: λ=5.55 cm for RSAT-2 vs. X: λ=3.1 cm for TSX/TDX) and the revisit time (24 days for RSAT-2 vs. 11 days for TSX/TDX). In addition, the available sets include different amount of scenes acquired using different modes.

The elements relative to the different temporal & spatial coverages and resolutions are presented thereafter in sections 3.2.1 and 3.2.2. The elements relative to the different line-of-sight and their impact on geometrical distortions are discussed in section 3.2.3. Tables highlighting the acquisition time, spatial and temporal baselines of each scene are available in Appendixes (Table 11, Table 12 & Table 13). Remember that the theory about the relationships between these different parameters and the advantages and limitations of InSAR results were presented in Chapter 2 and summarized in Table 1.

3.2.1 TEMPORAL COVERAGES & RESOLUTIONS

The three datasets have different temporal distributions (Table 4 & Figure 21). For RSAT-2 Standard mode, the dataset includes 72 scenes over 6 years between 2008 and 2014. It covers all the seasons but with a significant gap between November 2009 and October 2010. For RSAT-2 Ultrafine mode, the dataset is quite small including 20 scenes over 2 years between 2012 and 2014. It covers also all the seasons but with a higher density in summer and a gap between November 2013 and May 2014. For TSX/TDX StripMap mode, the dataset is also quite small including 23 scenes. It covers a wider interval than RSAT-2 Ultrafine mode (3 years between 2011 and 2014) but does not include winter scenes (only between March and September).

The repeat-pass interval and the sensor wavelength have an impact on the detection capability, depending on the speed of the moving area (see sections 2.1 & 2.2). Moreover the results have not the same time references due to the different temporal coverages. To compare the results, the maps are expressed for the three datasets in term of mean annual velocity, but it has to be kept in mind that the mean values are not calculated on the same temporal basis.

Table 4: TEMPORAL COVERAGES AND RESOLUTIONS					
Satellite	**Band (wavelength)**	**Repeat-pass interval**	**Dataset mode**	**Number of images**	**Time period**
RSAT-2	C (λ=5,55 cm)	24 days	Standard	72	10.2012 - 10.2014
			Ultrafine	20	11.2008 - 11.2014
TSX/TDX*	X (λ=3,11 cm)	11 days	StripMap	23	07.2011 - 06.2014

* From [Cetinic, et al., 2015 (in prep.)]

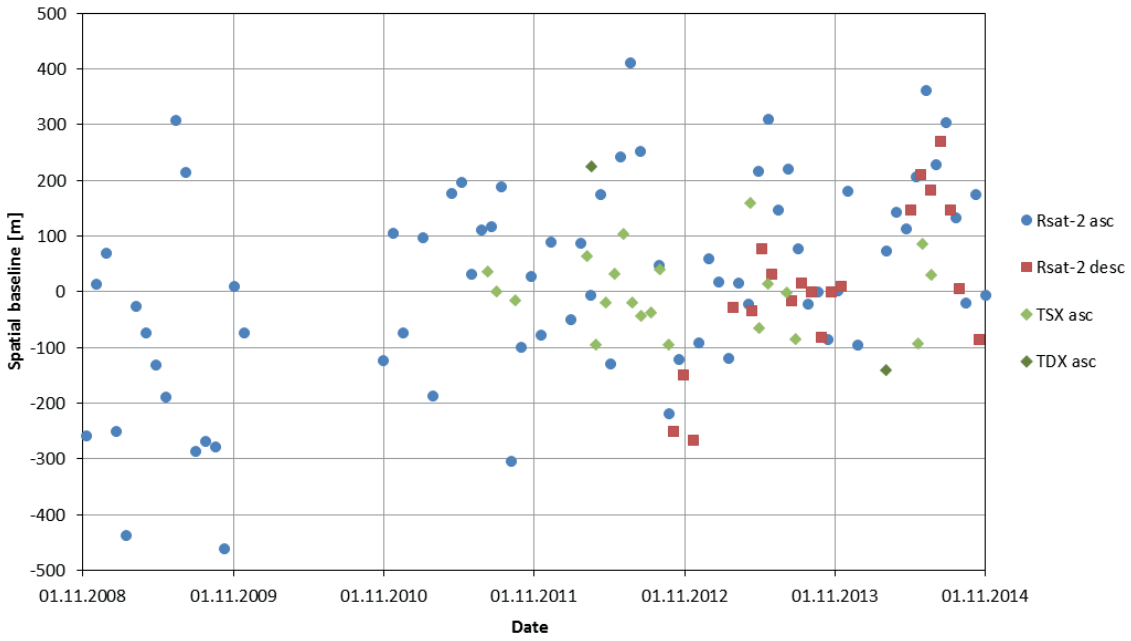

Figure 21: Baseline plot (perpendicular baseline vs. acquisition time) for the 3 datasets highlighting the temporal variability of the 3 datasets: blue circles: RSAT-2 Standard mode, red squares: RSAT-2 Ultrafine mode, green diamonds: TSX/TDX StripMap mode [Cetinic, et al., 2015 (in prep.)]. Based on information available in Table 11, Table 12 & Table 13 (in Appendixes)

3.2.2 SPATIAL COVERAGES & RESOLUTIONS

Each dataset has a different coverage of the region of interest and different spatial resolutions (Table 5 & Figure 22). RSAT-2 Standard mode has a medium resolution (range x azimuth: 23.3 m x 5.1 m) but the scenes cover a large area of 100 km x 100 km to Norheimsund, Bolstadøyri and Namdal at their east edge. For RSAT-2 Ultrafine mode, the resolution is clearly better (range x azimuth: 2.8 m x 2.1 m) but the scenes cover only a small area including Bergen (20 km x 20 km). For TSX/TDX StripMap mode, the resolution is even better than RSAT-2 Ultrafine mode (range x azimuth: 1.5 m x 2.1 m) and the size of the scenes (30 km x 50 km) allows a coverage to Vaksdal og Haga at their east edge. It should be thus noted that in the eastern part of the region, only RSAT-2 Standard mode is available. Because of its low resolution, it makes impossible the detection of small moving areas.

As discussed in section 2.3.3, depending on the processing methods the final resolution can change. Using Persistent Scatterers Interferometry (PSI), the results are in full resolution (3rd column in Table 5). Using Small BAseline subset (SBAS), the results have to be multilooked (4th column in Table 5) and the resolution is thus reduced (5th column in Table 5).

Table 5: SPATIAL COVERAGES AND RESOLUTIONS					
Satellite	**Dataset mode**	**Full resol. (ra / az)**	**SBAS multilook. (ra / az)**	**SBAS resol. (ra / az)**	**Scene size (ra / az)**
RSAT-2	Standard	23.3 m / 5.1 m	2 / 8	46.5 m / 46.2 m	100 km / 100 km
	Ultrafine	2.8 m / 2.1 m	6 / 8	16.5 m / 16.6 m	20 km / 20 km
TSX/TDX*	StripMap	1.5 m / 2.1 m	8 / 6	12.4 m / 12.3 m	30 km / 50 km

* From [Cetinic, et al., 2015 (in prep.)]

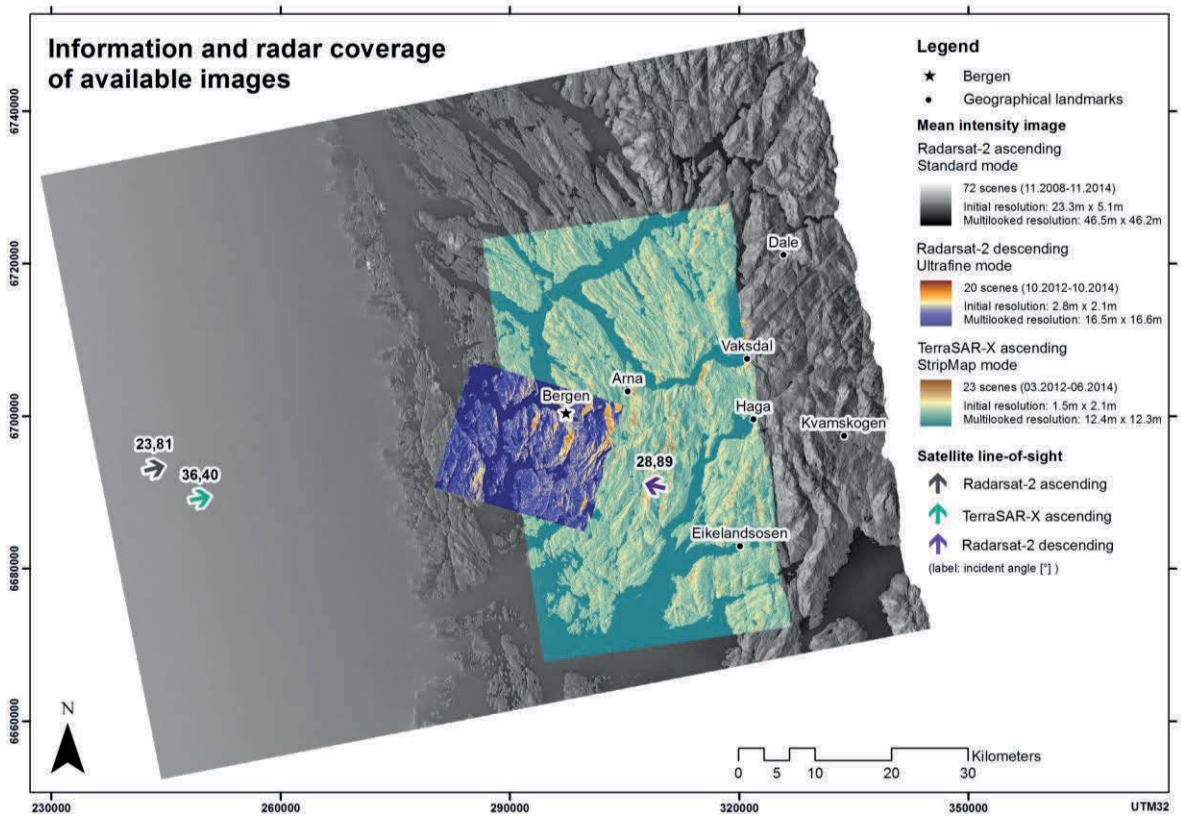

Figure 22: Spatial coverage and summary of main characteristics of the three satellite datasets, illustrated here using the mean intensity images of the areas covered for each dataset. The ascending satellites are flying parallel to the left edge of the images; the descending satellite is flying parallel to the right edge of the image. The arrows represent the LOS orientation. (TSX/TDX: [Cetinic, et al., 2015 (in prep.)])

The different spatial coverages and resolutions have obviously an impact on the size of the potential analyzed area, as well as on the detection capability, depending on the size of the moving area. In order to illustrate the effects of the different spatial resolutions of

the three datasets on the ground features detection, a comparison of the mean intensity images over Bergen is available in Figure 23.

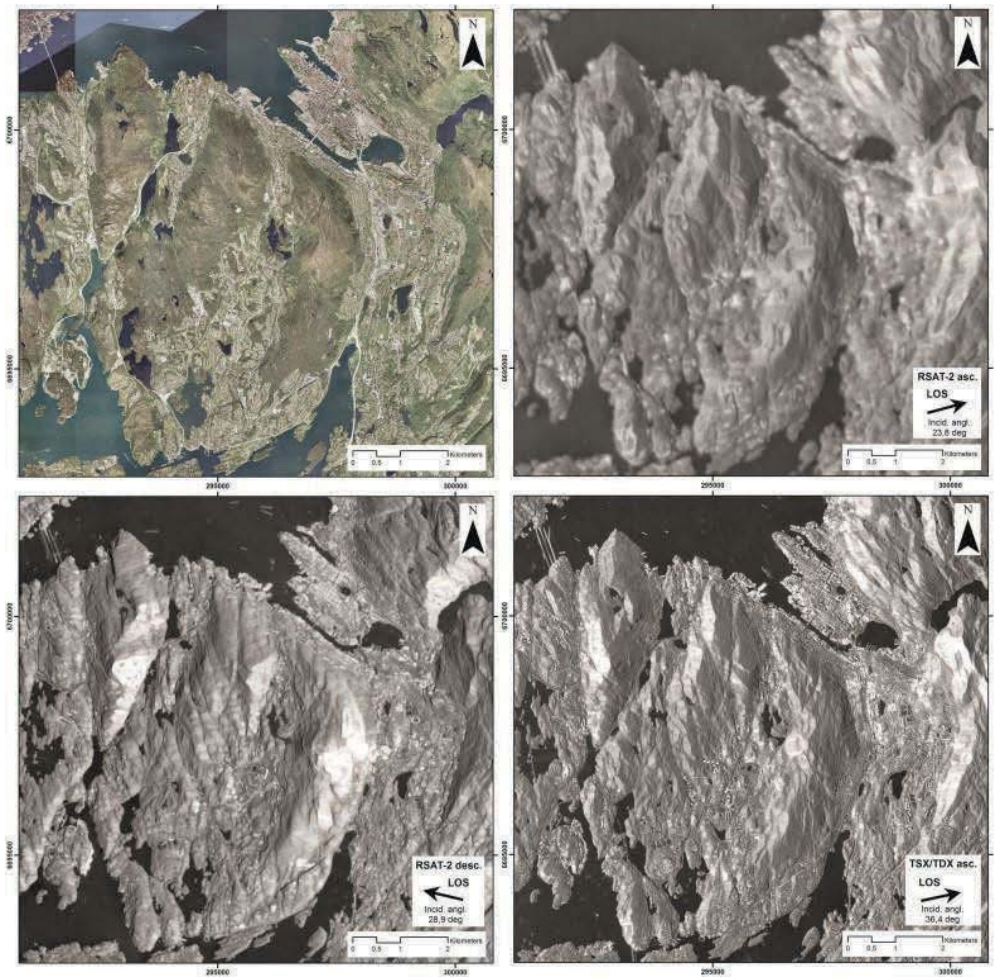

Figure 23: Effect of the SAR resolution on the quality of ground features display. From top left to bottom right: orthophoto & mean intensity images for RSAT-2 Standard mode, RSAT-2 Ultrafine mode, TSX/TDX StripMap mode [Cetinic, et al. 2015 (in prep.)].

3.2.3 LINE-OF-SIGHT & GEOMETRICAL EFFECTS

Each dataset has a different measurement direction (line-of-sight: LOS) according to the track orientation and the incidence angle of the SAR geometry (Table 6 & Figure 24). For RSAT-2 Standard mode, the scenes of the dataset were acquired using an ascending geometry (satellite flying from the S-SE to the N-NW, with a 345.4°N orientation). The LOS is thus toward E-NE, with a quite steep view (incidence angle θ: 23.8°). For RSAT-2 Ultrafine mode, a descending geometry was used (satellite flying from the N-NE to the S-SW, with a 283.4°N orientation). The LOS is thus toward W-NW, with a view more oblique than for RSAT-2 standard mode (incidence angle θ: 28.89°). For TSX/TDX StripMap mode, the data were acquired using an ascending geometry, with an orientation slightly more toward the N than RSAT-2 Standard mode (348.5°N

orientation). The LOS is also toward W-NW, but with a view clearly more oblique than RSAT-2 (incidence angle θ: 36.4°).

The line-of-sight (LOS) has an impact on the detection capability. Indeed, due to the ability of the satellite to measure only 1D displacement along the LOS, any moving area with a direction perpendicular to the LOS will be missed, and more the directions of the displacements diverge than the LOS, more they are underestimated.

Table 6: SAR GEOMETRIES AND LINE-OF-SIGHT (LOS) ORIENTATIONS					
Satellite	**Dataset mode**	**Orbit**	**Incidence angle**	**Track angle**	**LOS orientation**
RSAT-2	Standard	Ascending	23,8°	-14,6°	75,4°
	Ultrafine	Descending	28,9°	-166,6°	283,4°
TSX/TDX*	StripMap	Ascending	36,4°	-11,5°	78,5°

* From [Cetinic, et al., 2015 (in prep.)]

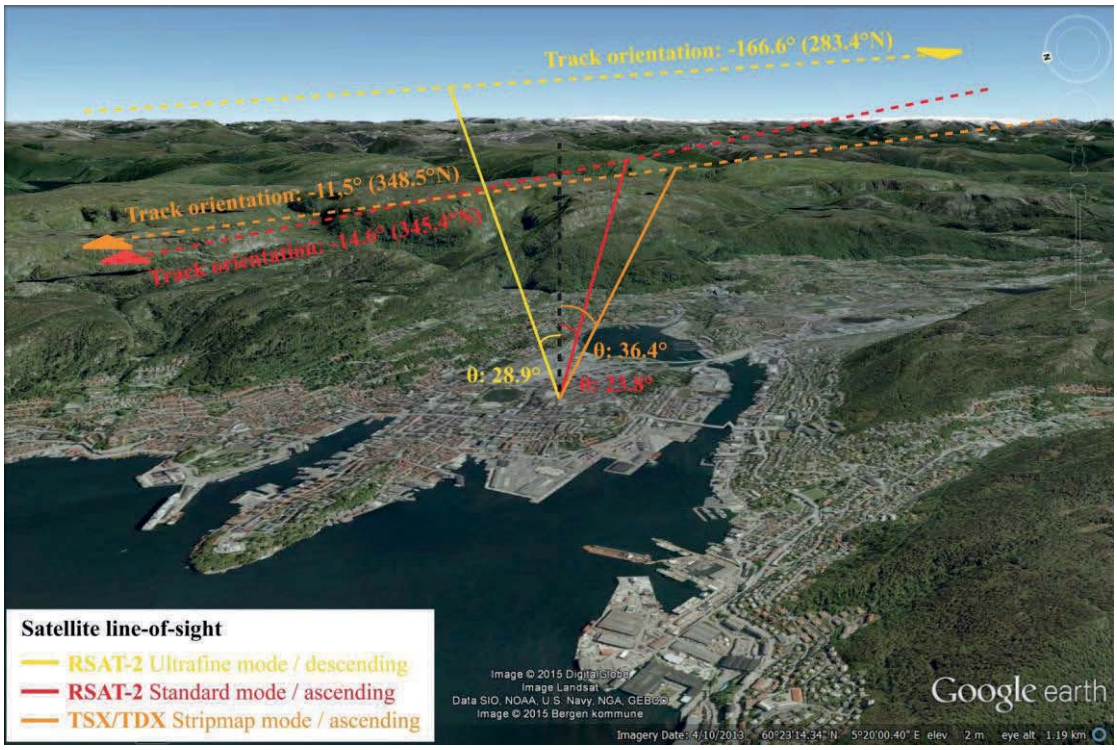

Figure 24: Schematic representation of the satellites tracks and line-of-sight over Bergen

The LOS has also an impact on the geometrical distortions according to the local topography (see section 2.1.4). In Figure 25, the Digital Elevation Model (DEM) of the area is presented as well as shaded reliefs generated using the information about the SAR track and its line-of-sight to define the orientation of the illumination source. It appears that with an ascending geometry, the west-facing relief with a slope perpendicular to the LOS will be affected by layover effects, while the east-facing relief

can be affected by shadow (and the opposite for descending geometry). The areas affected by layover and shadow thus vary according to the datasets and require the generation of masks. They will be presented and compared in section 4.1.

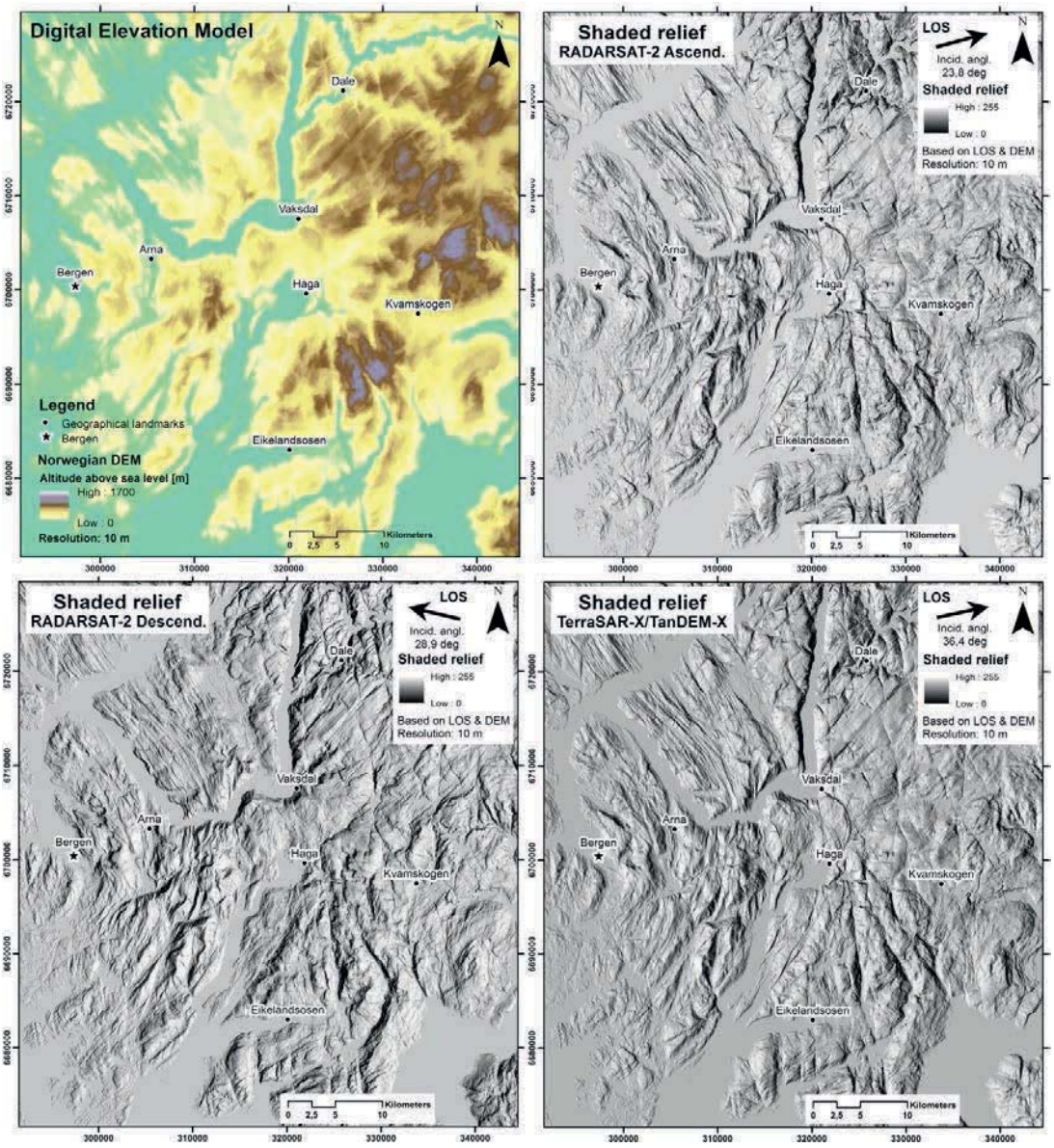

Figure 25: Digital Elevation Model and shaded relief generated considering the respective LOS of RSAT-2 Standard mode, RSAT-2 Ultrafine mode and TSX/TDX StripMap mode [Cetinic, et al. 2015 (in prep.)] as illumination source considered to be at infinity. By default hillshades are expressed as integers between 0 (shadow) and 255 (beam perpendicular to the local slope). The calculation method is available in [Burrough & McDonell, 1998].

4 INSAR RESULTS: BERGEN AREA

This Chapter presents results from InSAR analysis using the case study of Bergen area. As briefly described in section 2.3.4, the most interesting results concern usually the ground deformation and can be expressed as deformation maps or time series (section 4.3). But other derived produces can also be generated. They are mainly related to geometrical effects and temporal decorrelation. Because they are valuable to better understand advantages and limitations of InSAR technology, they will be presented in sections 4.1 and 4.2.

4.1 SHADOW & LAYOVER MASKS

Shadow and layover masks can be generated depending on the line-of-sight and the local topography. The areas affected by these geometrical effects will be removed of the final analysis.

Over Bergen area, the datasets are overall not highly affected by shadow due to the relatively vertical views of the satellite, but the layover effect has a high impact. Depending on the different lines-of-sight, layover varies significantly according to the datasets. Due to its small incidence angle, the RADARSAT-2 (RSAT-2) Standard mode dataset is highly affected by layover on east facing slopes, but little by shadow. For RSAT-2 Ultrafine mode (descending geometry), the layover effect occurs on west facing slope. The TerraSAR-X/TanDEM-X (TSX/TDX) StripMap mode dataset (ascending geometry) [Cetinic, et al. 2015 (in prep.)] is less affected by layover and more by shadow than RSAT-2 Standard mode, due to its higher incidence angle.

The shadow and layover masks for the three datasets are presented in Figure 26 and Figure 27. In Figure 28 and Figure 29, smaller areas are highlighted (zooms of the blue squares on Figure 26 & Figure 27) in order to give a better view of the differences between the datasets. Figure 28 (left) compares RSAT-2 Standard mode and TSX/TDX StripMap mode (RSAT-2 Ultrafine not available at this location). Both datasets have an ascending geometry with quite similar LOS orientation toward NE, but the different incidence angles induce significant differences in the extent of the geometrical effects (larger incidence angle for TSX/TDX StripMap mode: more areas affected by shadow, and less by layover). Figure 28 (right) compares the three datasets. It shows that layover effect is present on west facing slopes for ascending geometry and east facing slopes for descending.

Overall it clearly appears the use of the RSAT-2 Standard mode is strongly limited by the layover. The mask affects a large proportion of the scenes (16 % on land). It reduces the areas available for the analysis, but also makes them discontinuous and thus more difficult to process.

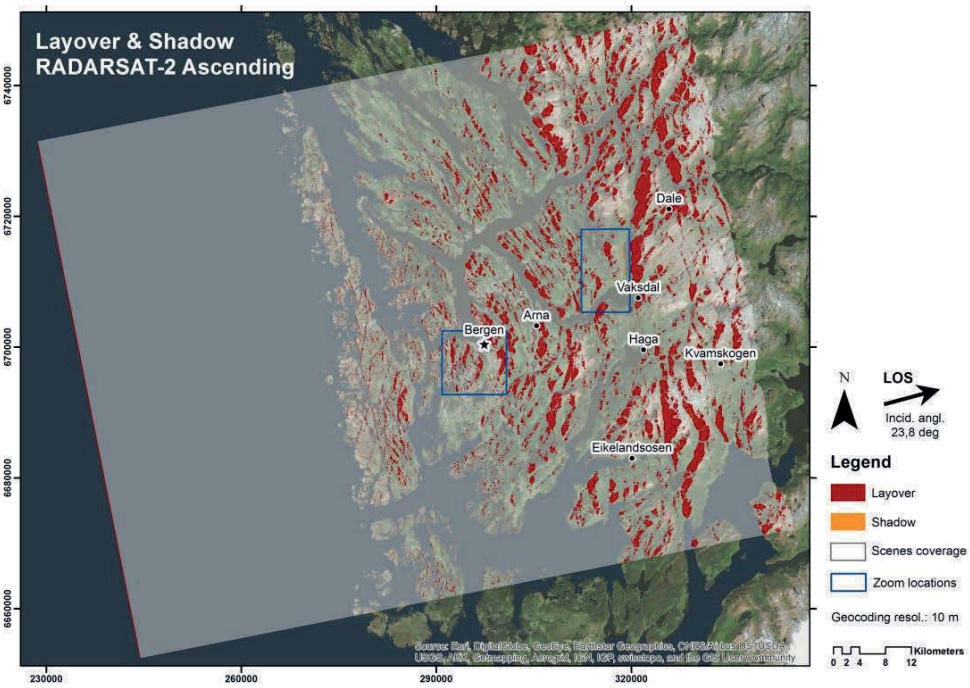

Figure 26: Areas affected by layover & shadow for RSAT-2 Standard mode (ascending geometry). The dataset is highly affected by layover effects but little by shadow due to its steep incidence angle.

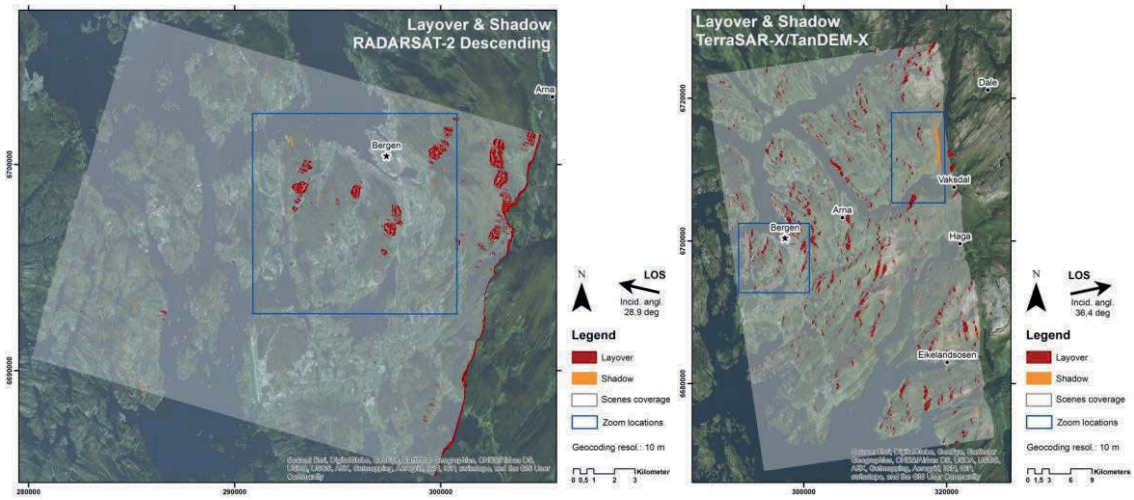

Figure 27: Left: areas affected by layover & shadow for RSAT-2 Ultrafine mode (descending geometry). Layover effect occurs on west facing slopes contrary to RSAT-2 Standard mode, due to the different geometry. Right: areas affected by layover & shadow for TerraSAR-X/TanDEM-X StripMap mode (ascending geometry) [Cetinic, et al. 2015 (in prep.)]. The dataset is less affected by layover and more by shadow than RSAT-2 Standard mode, due to the larger incidence angle.

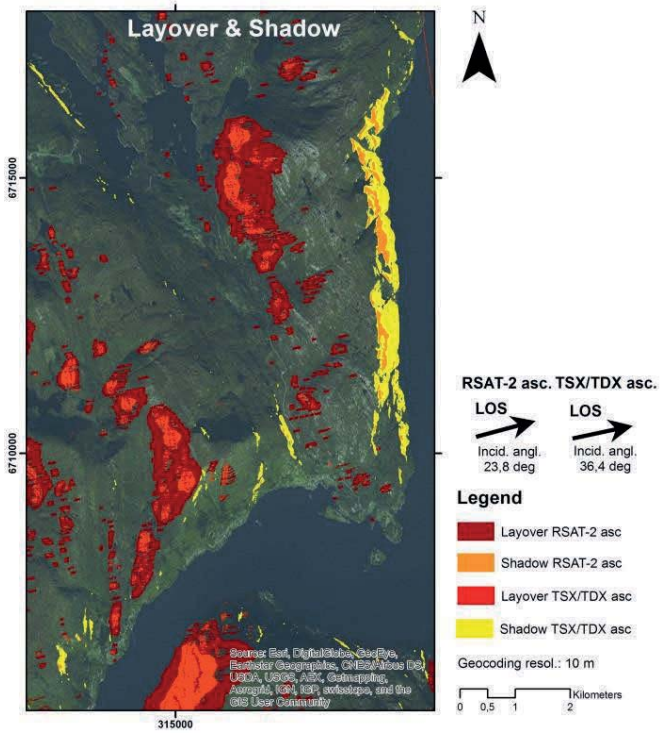

Figure 28: Zoom in the west of Vaksdal (upper right blue square in Figure 26 & Figure 27). Area covered by RSAT-2 Standard mode and TSX/TDX StripMap mode [Cetinic, et al. 2015 (in prep.)].

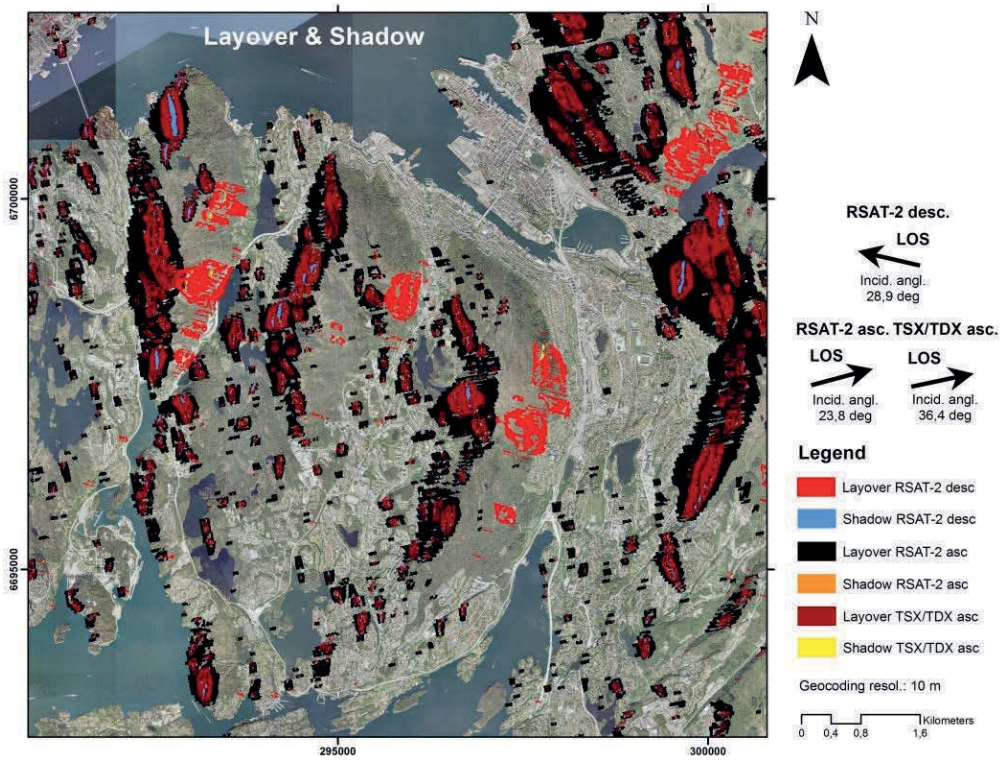

Figure 29: Zoom on Bergen (lower left blue square in Figure 26 & Figure 27). Area covered by RSAT-2 Standard mode, RSAT-2 Ultrafine mode & TSX/TDX StripMap mode [Cetinic, et al. 2015 (in prep.)].

4.2 TEMPORAL DECORRELATIONS

4.2.1 SPATIAL VARIATIONS

As described in section 2.2.4, InSAR results can be affected by temporal decorrelations due to changes in geometrical or electrical properties of the surface, as function of time between the acquisitions. A way to measure the stability of the signal is the coherence which is a complex correlation coefficient. Using a stack of interferograms, a mean coherence map can be generated. Looking at the spatial distribution of the values it clearly appears that the land cover has an impact of the signal stability. In this way, it is interesting to compare it with the distribution of the vegetation over the area under study. In Figure 30, a simplified version of a vegetation map over Bergen area is compared with a mean coherence map using RSAT-2 Standard mode interferograms with a temporal baseline of 24 days only. It clearly appears that vegetated areas, especially forests have a generally low phase correlation, even for a small temporal baseline while urban and arid areas show higher signal stability. In the eastern part, the patches of medium coherence corresponding to the mountainous parts without dense vegetation are discontinuous which makes difficult the production of relevant InSAR results.

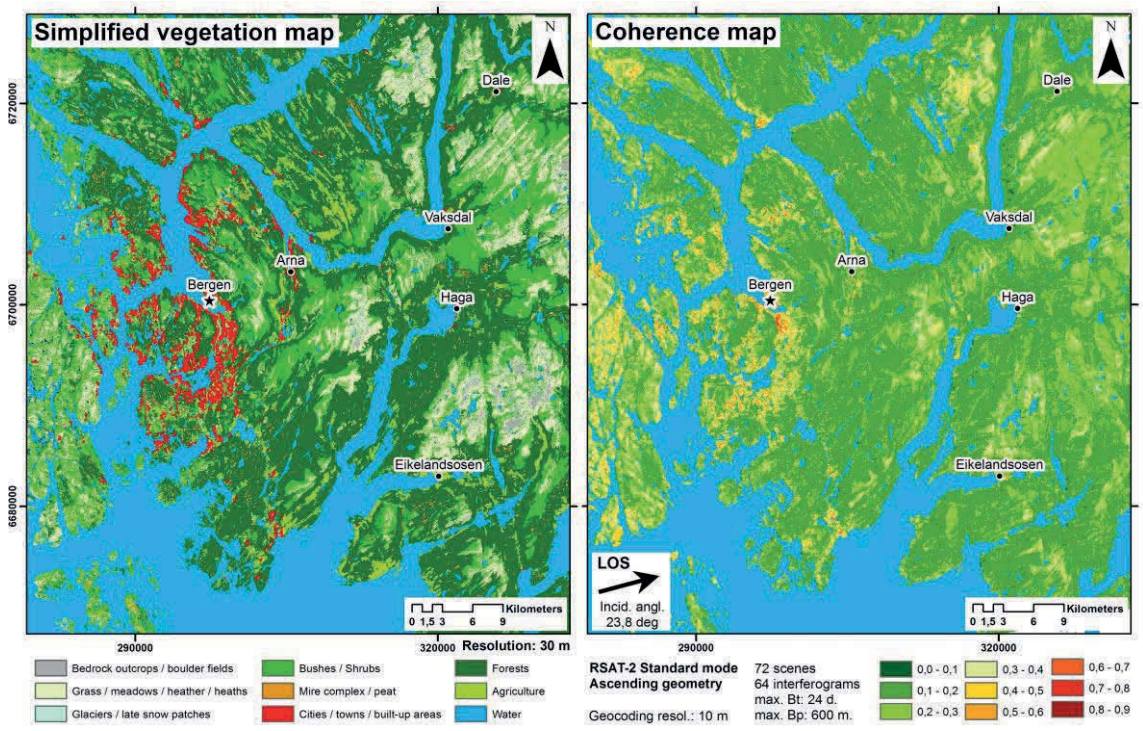

Figure 30: Left: simplified vegetation map over Bergen area (8 classes) based on vegetation map from [Johansen, 2009 & Johansen, et al. 2009]. Right: Example of mean coherence map from RSAT-2 Standard mode dataset (using only interferograms with a temporal baseline of 24 days).

4.2.2 SEASONAL VARIATIONS

The coherence varies also in time. For example, terrain containing variable liquid water, such as e.g., areas covered with wet snow, will also have different scattering properties from one observation to the next. Thus, in areas affected by snow during the winter, the coherence can vary a lot according to the season. The winter scenes can be unusable if bare rocks or artificial infrastructure allowing high signal stability are not present above the snow level. In Figure 31, two examples of simple interferograms in summer and in winter between RSAT-2 Standard mode acquisitions with a temporal baseline of 24 days are presented and compared with the snow cover at this period.

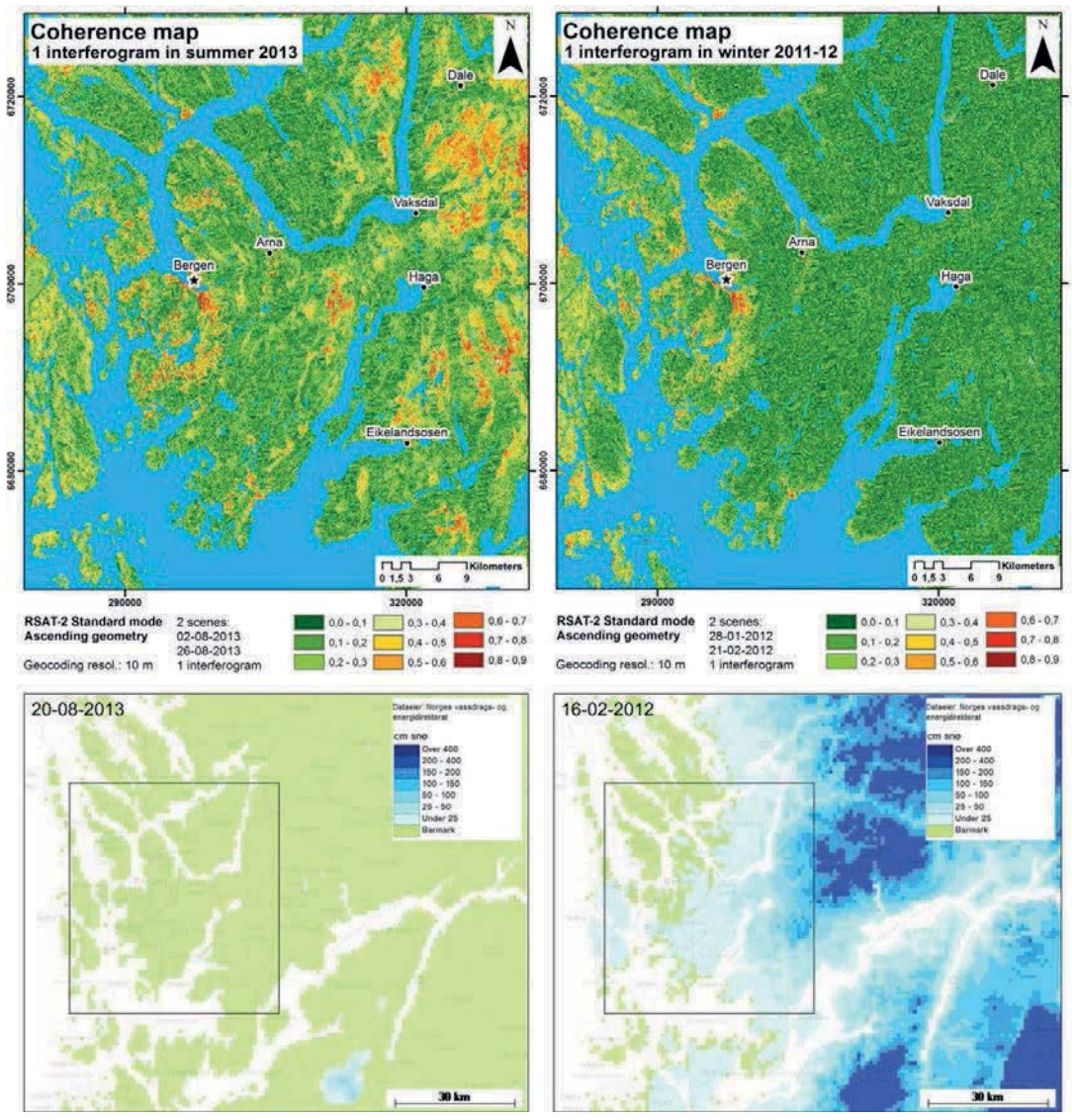

Figure 31: Examples of the effects of snow cover on the coherence (RSAT-2 Standard mode dataset). Top left: coherence map based on 1 interferogram in summer 2013. Top right: coherence map based on 1 interferogram in winter 2011-12. Bottom: Snow depth at the same period as the interferograms. From www.senorge.no (download: 16-02-2015).

On the left of Figure 31, the interferogram was generated using scenes in summer 2013 (02-08-2013 & 26-08-2013) and on right, using scenes in winter 2011-12 (28-01-2012 & 21-02-2012). The summer interferogram shows good coherence values on the urban areas as well as in the areas with bare rocks or low vegetation. The winter interferogram shows significant temporal decorrelation on the whole eastern part due to the snow, except on urban areas. The seasonal variations can require removing winter scenes. In areas where snow affects large areas over a long time period, this is a significant limitation that can severely reduce the amount of usable interferograms.

4.2.3 COHERENCE OR AMPLITUDE DISPERSION FILTERS

In practice the coherence map is also used to select pixels that will be used for the ground deformation analysis. During the SBAS processing, in addition to the layover/shadow masks, a coherence mask is thus generated using a coherence threshold defined by the operator (Figure 32).

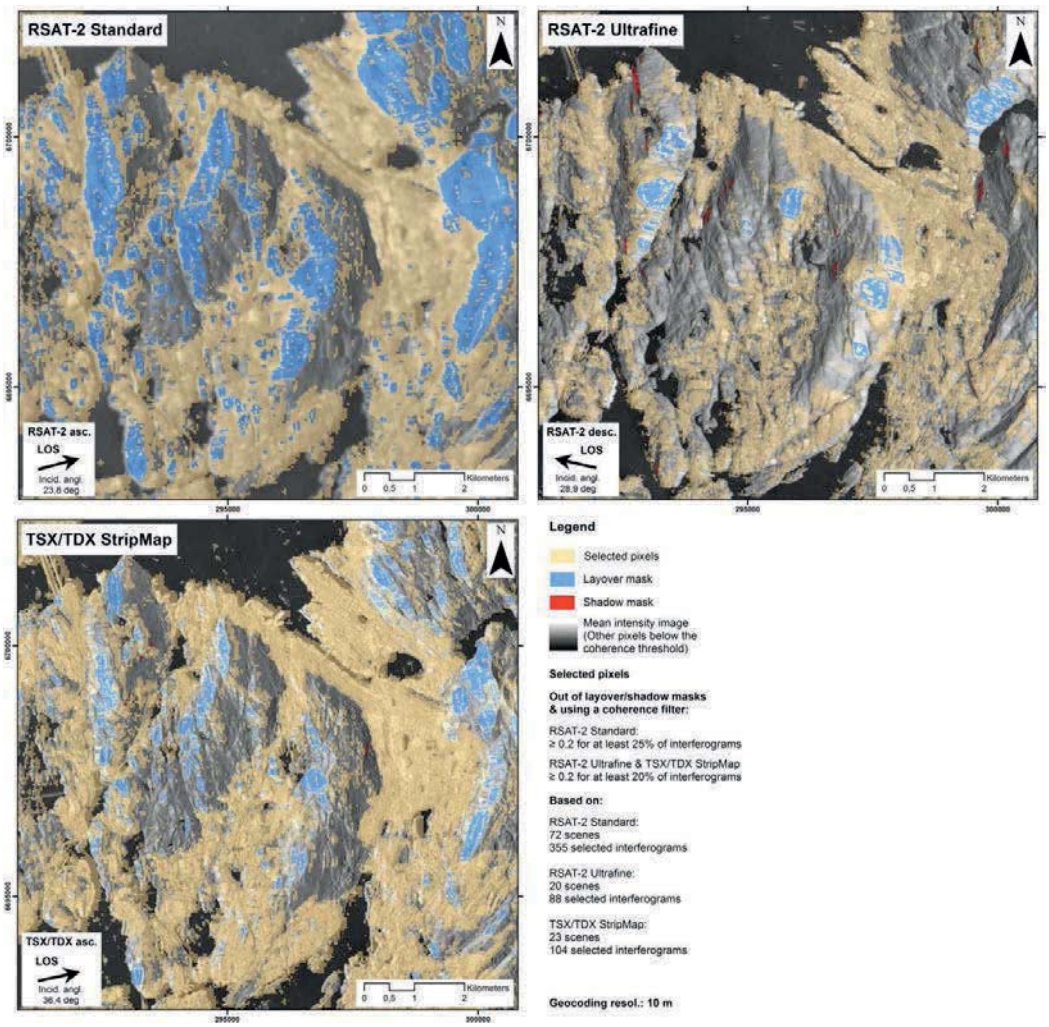

Figure 32: Example of selected pixels for the SBAS analysis over Bergen for each dataset (TSX/TDX: [Cetinic, et al. 2015 (in prep.)]), depending on the applied coherence threshold and the layover & shadow masks.

The selected pixels correspond finally to those outside the layover/shadow masks with a coherence value above a defined coherence value (for ex. 0.3) for a minimum percent (for ex. 25 %) of the used interferograms. The choice of the thresholds is a balance between amount of selected pixels and good coherence. A too high coherence threshold can indeed lead to too small areas of analysis organized in discontinuous patches.

For PSI processing, instead of a coherence threshold, the amplitude dispersion is used to select the points used for the analysis. As for the coherence threshold in SBAS procedure, the choice of the thresholds is a balance between low amplitude dispersion and amount of points. Figure 33 shows an example of primary and complete networks over Bergen using the RSAT-2 Ultrafine dataset. Here the applied amplitude dispersion threshold is 0.2 for the primary network (Figure 33, left) and 0.35 for the complete network (Figure 33, left).

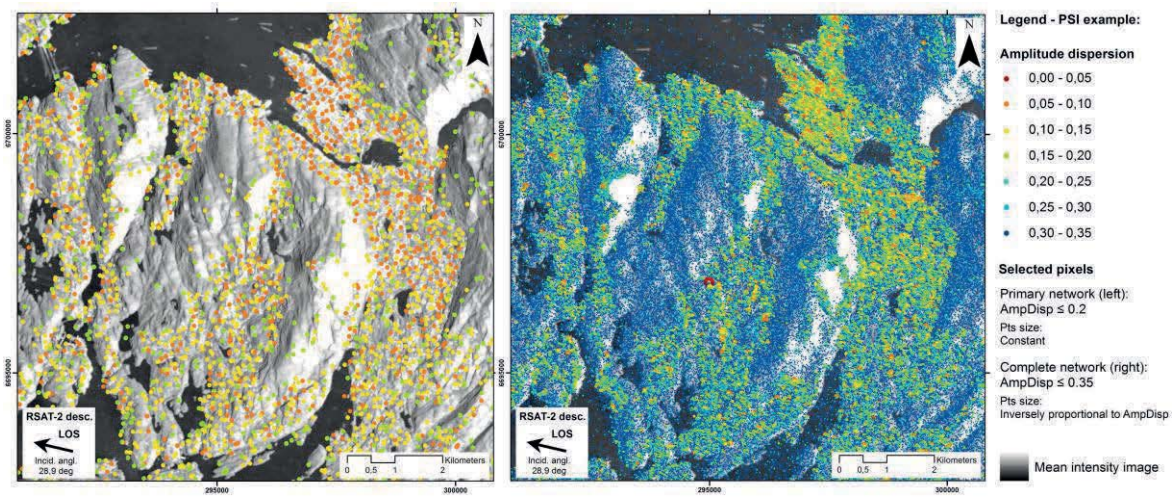

Figure 33: Example of primary (left) and complete (right) PS networks based on two amplitude dispersion thresholds (RSAT-2 Ultrafine dataset).

4.3 GROUND DEFORMATION RESULTS

The ground deformation results are presented separately for different subareas. In section 4.3.1, the results on Bergen are analyzed. Although this area was not specified in the main areas of interest for the partners (see section 3.1.2), it is the only sector covered by RSAT-2 Ultrafine mode and it is interesting to have one case study comparing the three datasets. Moreover the coherence is good in this area due to the urban infrastructure which give overall better results than most of the areas in the eastern part. In section 4.3.2, results in Indre Arna are analyzed. In section 4.3.3, some results from the eastern part of area are introduced (Samnangerfjorden - Kvamsskogen - Dale). However, it has to be noted that due to the limitations described in sections 3.2, 4.1 and 4.2, especially related to the spatial resolution, the geometrical effects and the coherence, the reliability of the results are highly reduced.

The main deformation maps presented thereafter are based on stacking and PSI methods (see section 2.3.3). A SBAS method is used to retrieve the time series presented in sections 4.3.1.2 and 4.3.2.2. All the maps displayed the mean velocity in millimeter per year along the line-of-sight. Negative values correspond to deformation away from the SAR sensor. Positive values correspond to deformation toward the SAR sensor. The millimetric interval that was chosen for the color scale highlights that the displacements over the area are very small. It should be noted that for display purpose the scales vary from a dataset to another. The results differences are due to the different wavelengths and revisit times of the sensor, as well as the different lines-of-sight, spatial resolution, temporal coverage of the datasets.

4.3.1 BERGEN

4.3.1.1 DEFORMATION MAPS

The availability of three datasets on Bergen makes this area interesting to compare InSAR results. In Figure 34 (up left), a map highlights Bergen and the different zooms (letters A-C) that will be used for the comparison. In Figure 34 (up right and bottom), stacking results of the three datasets are presented for the zoom A. Overall it appears that the area is not affected by significant ground deformation. However, some small moving areas are detected by several sensors. Their size and velocity varies especially due to the different spatial resolutions, line-of-sight and temporal distribution of available images. It appears for example that RSAT-2 Standard mode detects slower and spatially smoother deformation than the two other sensors due to its lower spatial resolution.

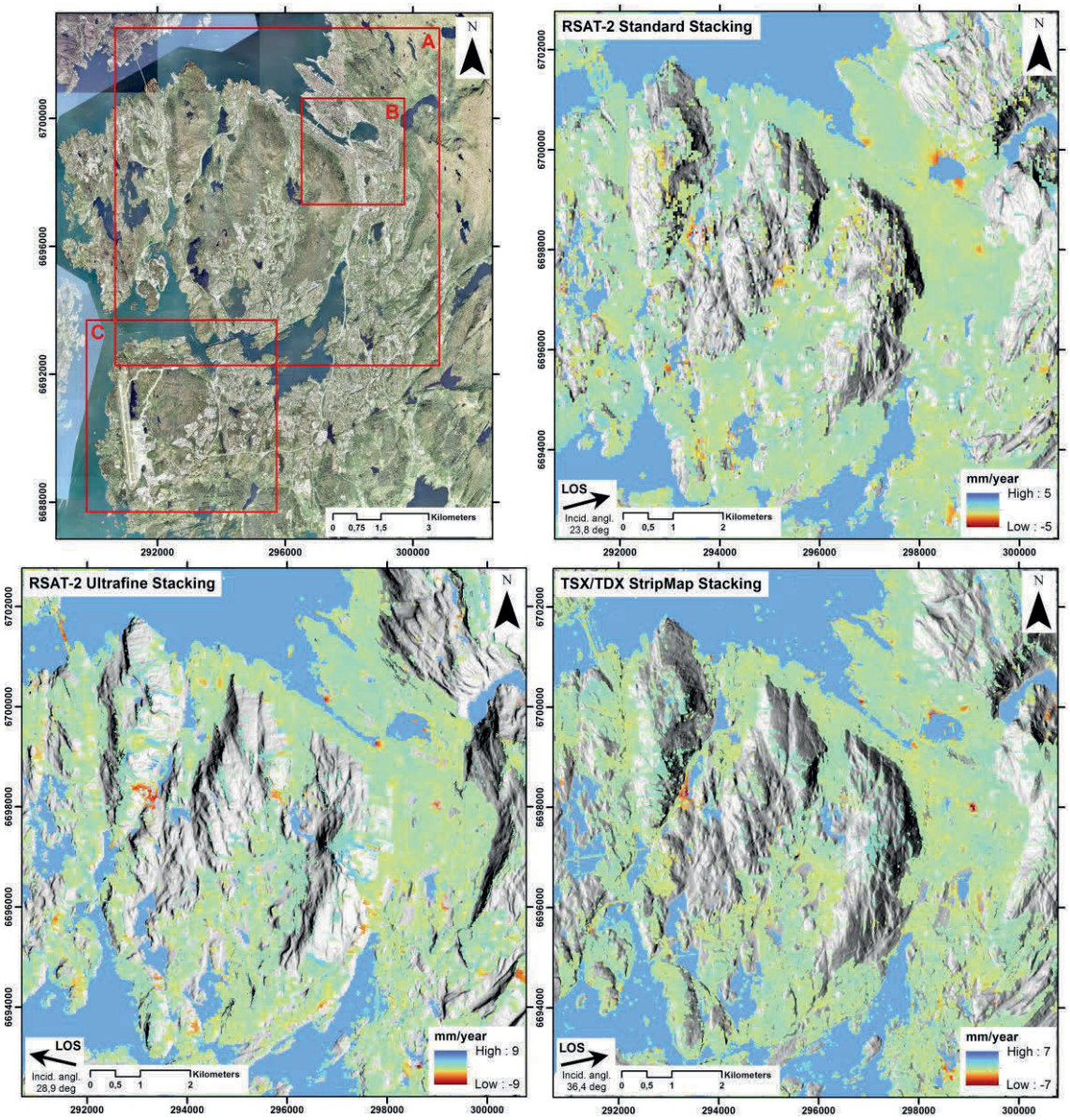

Figure 34: Up left: location map over Bergen with zooms of the analyzed areas. Up right: stacking results for RSAT-2 Standard mode (zoom A). Bottom left: stacking results for RSAT-2 Ultrafine mode (zoom A). Bottom right: stacking results for TSX/TDX StripMap mode (zoom A) [Cetinic, et al. 2015 (in prep.)]. Backgrounds: Norge i bilder orthophoto & LOS-related shaded reliefs.

The Figure 35 corresponds to the zoom B on downtown. Various small moving areas are present on the three sets of results: at Møhlenpris, Solheimsviken, around the Store Lungegårdsvann, on the North of the Brann Stadion. Comparing the results of the three datasets and the PSI and stacking methods, it appears that the moving sectors detected thanks to stacking are less well displayed by PSI due to small amount of Persistent Scatterers in the these areas.

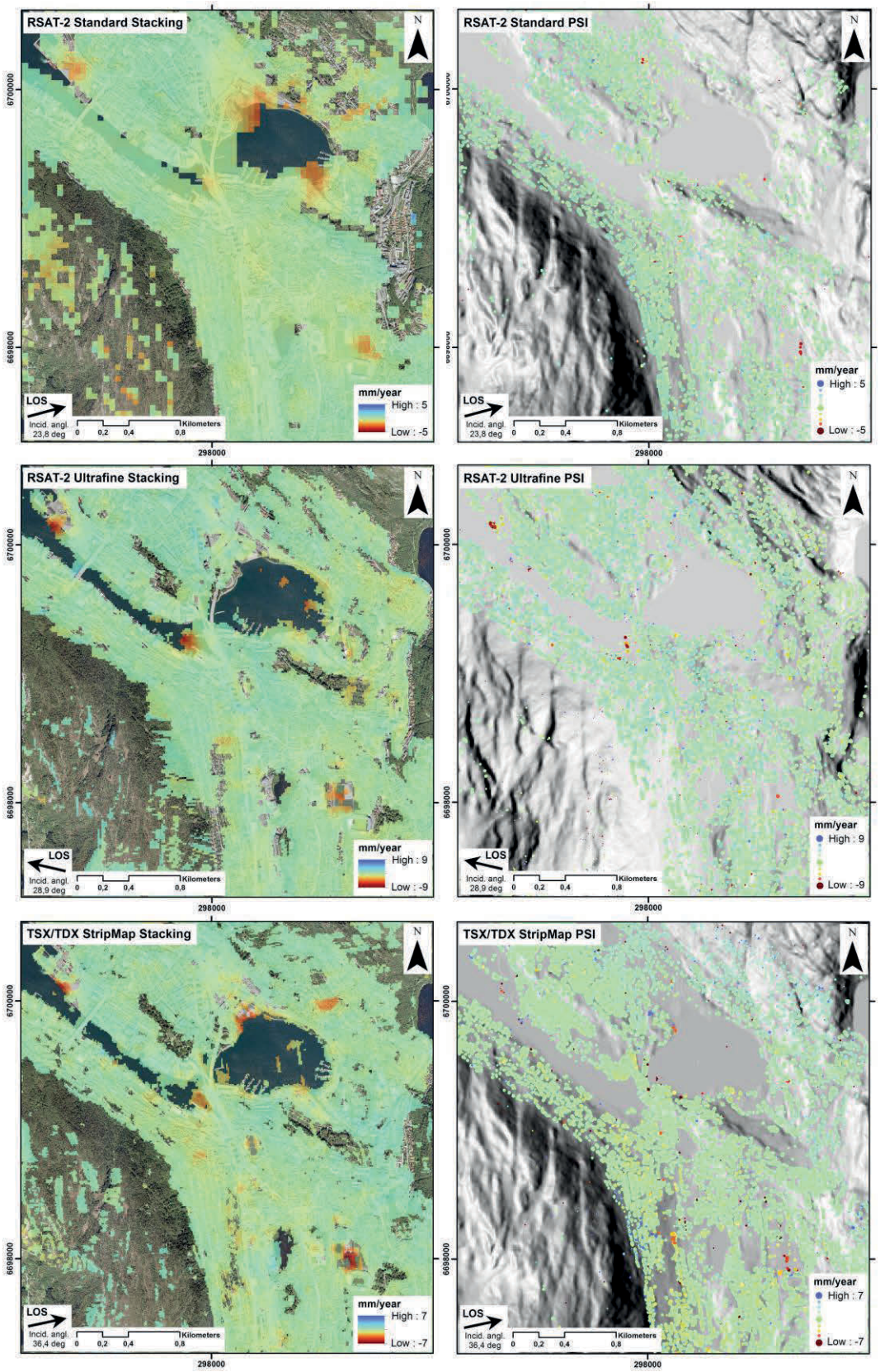

Figure 35: InSAR results on zoom B (see Figure 34). Left: stacking results. Right: PSI results. Top: RSAT-2 Standard mode. Middle: RSAT-2 Ultrafine mode. Bottom: TSX/TDX StripMap mode [Cetinic, et al. 2015 (in prep.)]. Backgrounds: Norge i bilder orthophoto & LOS-related shaded reliefs.

Figure 36 corresponds to the zoom C in the area of the airport. Here only the two RSAT-2 datasets are available. The moving area in the North of the landing strips appears to be a gravel pit, while the areas highlighted along the strips are artificial banks. The comparison of the two datasets clearly highlights the impact of the spatial resolution on the delineation and rate of movement. Comparing the results of PSI and stacking methods, it appears that the moving sectors detected thanks to stacking are less well displayed by PSI due to small amount of Persistent Scatterers aside the main artificial infrastructure. In the eastern part, some small patterns and especially on RSAT-2 Ultrafine dataset are probably due to unwrapping errors due to the patchy coherent area.

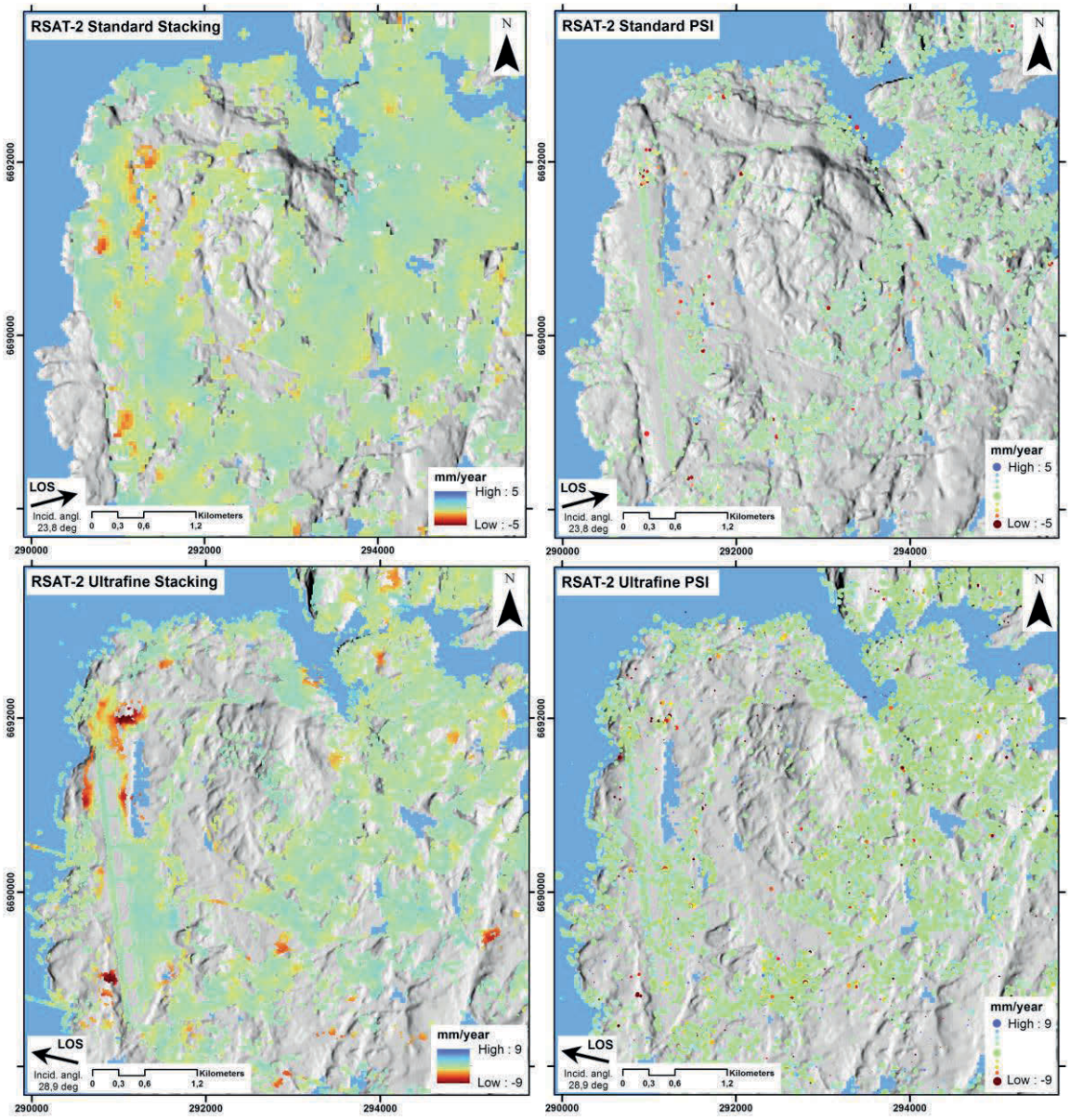

Figure 36: InSAR results on zoom C (see Figure 34). Left: stacking results. Right: PSI results. Top: RSAT-2 Standard mode. Bottom: RSAT-2 Ultrafine mode. Backgrounds: LOS-related shaded reliefs.

Figure 37 presents results on zooms D-E-F that show moving areas on the road 555 along the Liavtnet (zoom D), on the road 558 between Hetlevik and Haakonsvern (zoom E) and on the road 582 along Nesttunvatnet (zoom F). The moving patterns are present on the different datasets but only TSX/TDX StripMap mode results are highlighted here. Due to the spatial resolution and the line-of-sight, it allows indeed a better detection and delineation of the movement.

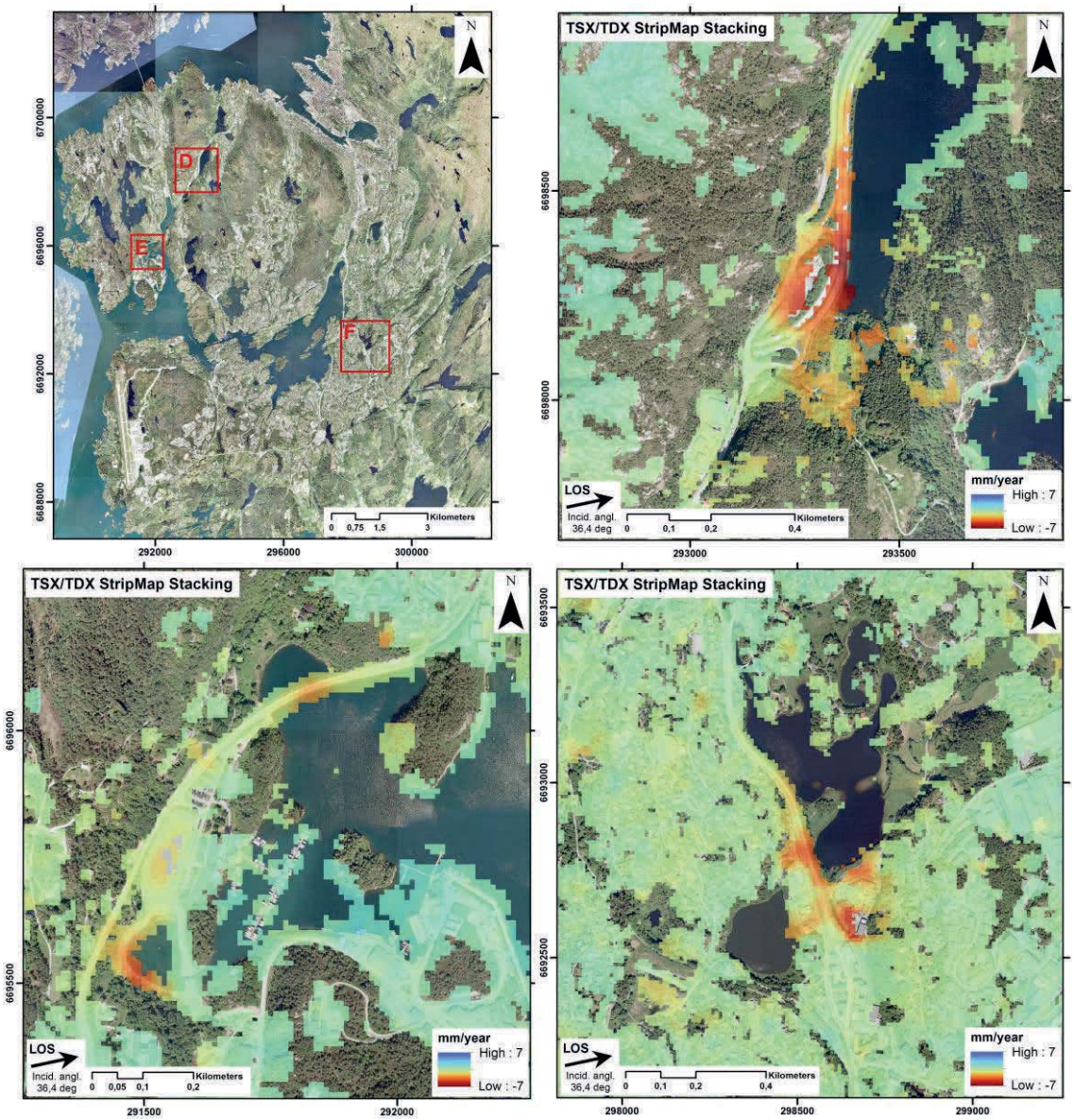

Figure 37: Up left: location map over Bergen with zooms on TSX/TDX StripMap mode results [Cetinic, et al. 2015 (in prep.)]. Up right: zoom D. Bottom left: zoom E. Bottom right: zoom F. Backgrounds: Norge i bilder orthophoto.

4.3.1.2 TIME SERIES

In addition to the analysis of the spatial distribution of ground deformation, it is possible to have a look on the temporal evolution of the displacements. The time series are extracted from SBAS and PSI results. In the graphs thereafter some time series used for the comparison have not been selected at the exact same location and averages of points have been performed in some cases.

Figure 38 shows these results for the zoom A that was also used for the stacking presentation in Figure 34. Some time series are analyzed for the locations D, E, F and in the North of the Brann Stadion (Figure 38, up left) previously presented in Figure 35 and Figure 37. For RSAT-2 Standard mode, the same color scale than stacking results is used. It shows that SBAS method allows detecting faster deformation, but is also more affected by noise.

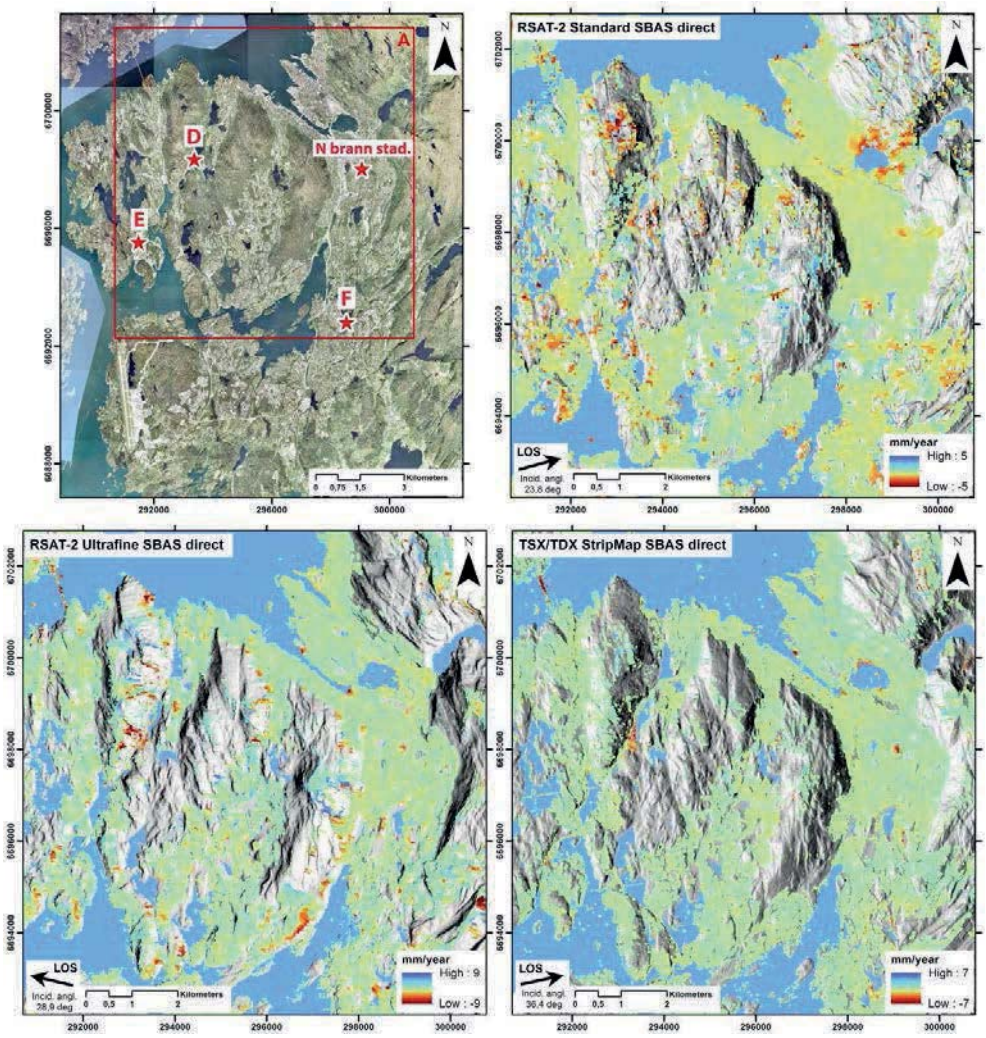

Figure 38: Up left: location map over Bergen with locations of zoom A and time series presented thereafter (red stars). Up right: SBAS results for RSAT-2 Standard mode (zoom A). Bottom left: SBAS results for RSAT-2 Ultrafine mode (zoom A). Bottom right: SBAS results for TSX/TDX StripMap mode (zoom A) [Cetinic, et al. 2015 (in prep.)]. Backgrounds: Norge i bilder orthophoto & LOS-related shaded reliefs

Figure 39 displays temporal evolutions of main moving sectors on the road 555 along the Liavtnet (D), on the road 558 between Hetlevik and Haakonsvern (E) and on the road 582 along Nesttunvatnet (F) (see Figure 37) using TSX/TDX StripMap dataset and PSI method. It shows that the different areas have not only different mean velocities but also different temporal variations. The datasets does not include winter scenes. It leads to large gaps between acquisitions. This can be challenging for the processing and induce errors in the time series retrieval.

Figure 40 compares PSI time series on the road 555 along the Liavtnet (D) with SBAS time series. It shows that the overall pattern is quite similar with a deceleration from summer 2013. However the rates of movement are different. In this case, SBAS probably underestimates the displacements due to the multilooking procedure (reduced resolution).

Figure 41 presents time series extracted on the footballs field in the North of the Brann Stadion in the center of Bergen. Here results from the different datasets, as well as from the different processing methods are presented. Due to different temporal coverage of the datasets, the RSAT-2 Ultrafine mode and TSX/TDX StripMap results are artificially shifted to be compared with RSAT-2 Standard mode. It clearly appears that the results from RSAT-2 Standard mode using SBAS underestimate the rate of movement. This is also slightly visible on the two others datasets. The difference of movement rates between the three datasets can be explained by their different line-of-sight. The two RSAT-2 datasets having opposite geometries (ascending/descending geometries) shows quite similar rates meaning that the movement is mainly vertical. TSX/TDX StripMap mode that has a larger incidence angle is less able to detect vertical component and thus gives lower rates.

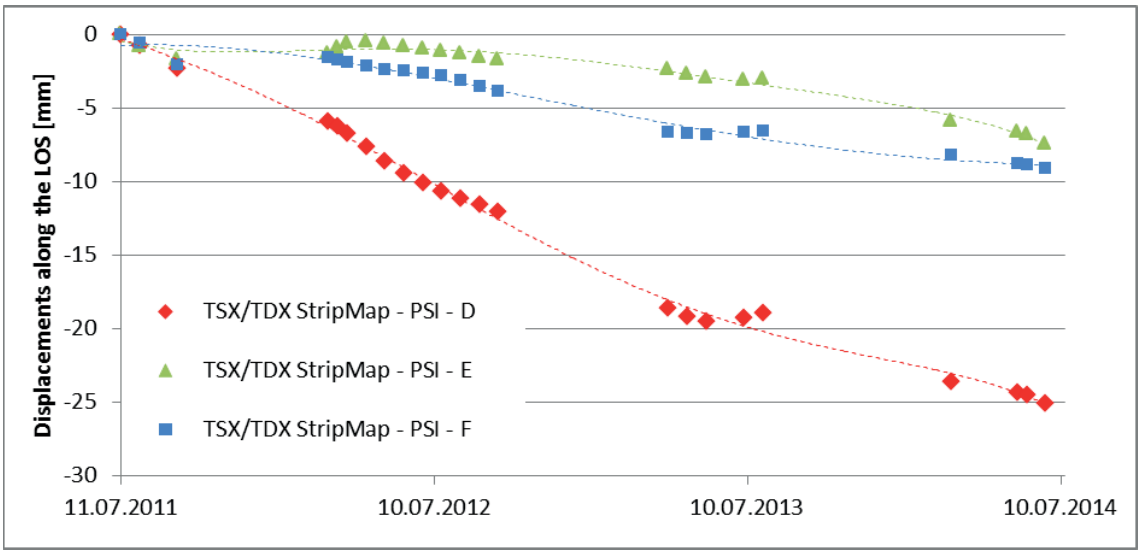

Figure 39: Comparison of PSI time series (TSX/TDX StripMap mode dataset) on the road 55 along the Liavtnet (location D: Figure 38), on the road 558 between Hetlevik and Haakonsvern (location E: Figure 38) and on the road 582 along Nesttunvatnet (location F: Figure 38).

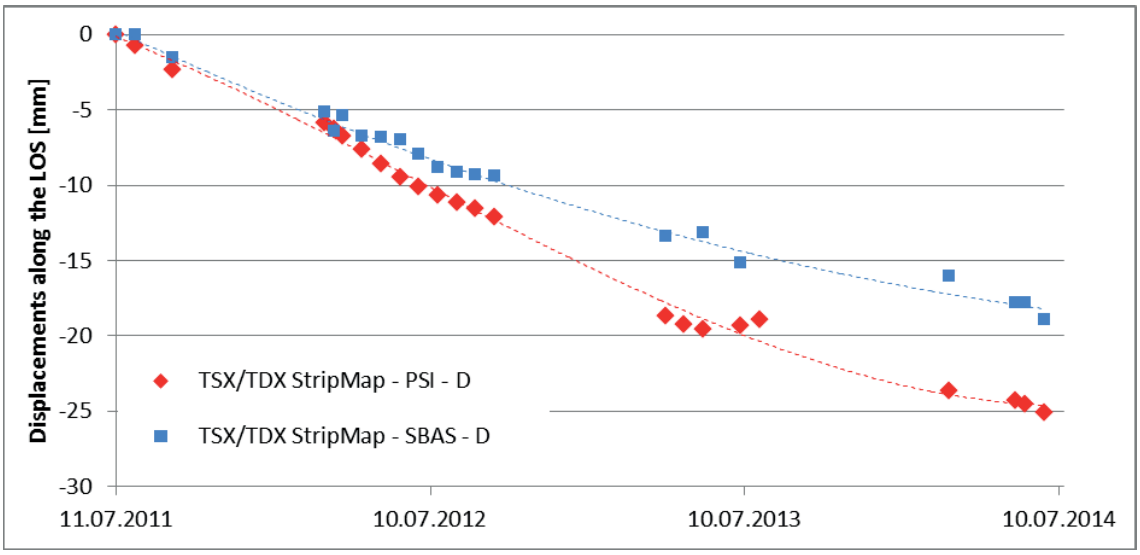

Figure 40: Comparison of SBAS and PSI time series (TSX/TDX StripMap mode dataset) on the road 55 along the Liavtnet (location D: Figure 38) highlighting probable underestimation of movement for SBAS results.

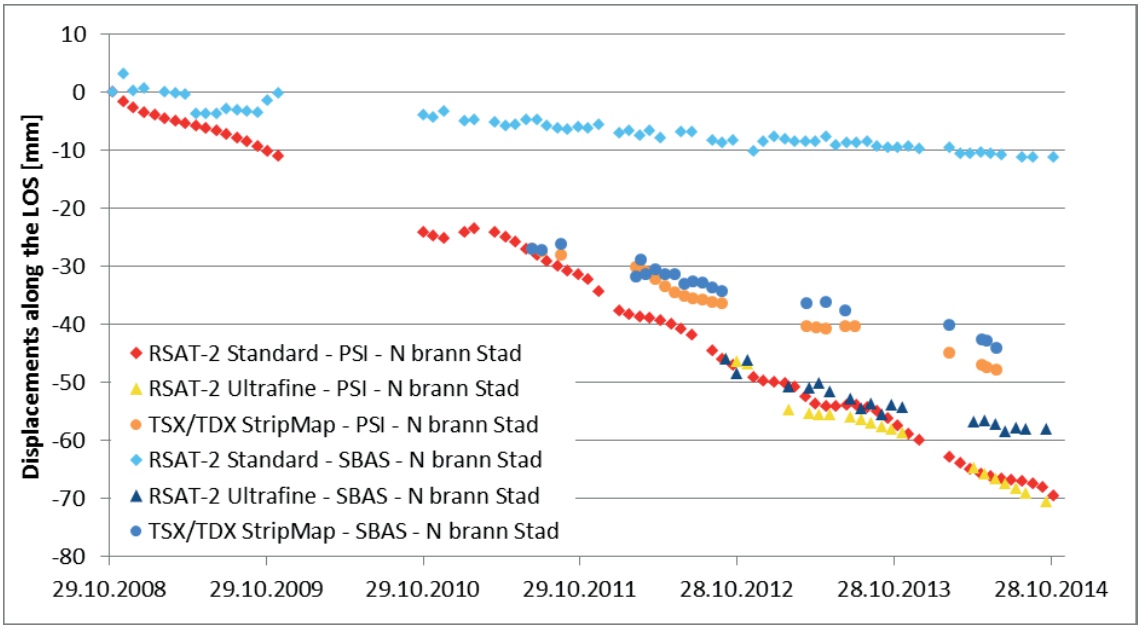

Figure 41: Comparison of SBAS and PSI time series for the three datasets close the Brann Stadion (location: Figure 38) highlighting variation of movement detection for the different sensors mainly due the different LOS and a clear underestimation for SBAS results from RSAT-2 Standard mode.

Around the airport, the SBAS results from RSAT-2 Standard mode show a large amount of noise. Only examples from RSAT-2 Ultrafine mode are thus presented thereafter. The SBAS deformation map (Figure 42) is quite similar to the stacking results presented in Figure 36. The time series extracted at the black stars locations (Figure 43) highlight various temporal patterns (succession of acceleration/deceleration for location 1, deceleration for location 2 and quite linear deformation for location 3).

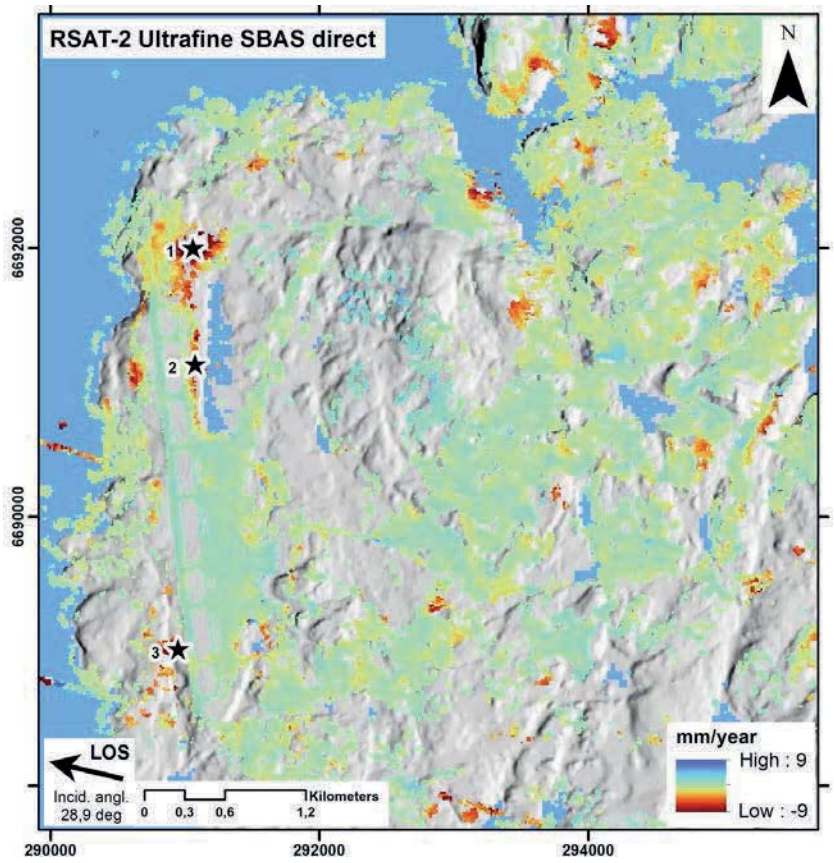

Figure 42: SBAS results for RSAT-2 Ultrafine mode on zoom C (see Figure 34). Black stars: locations of time series presented thereafter. Background: LOS-related shaded relief.

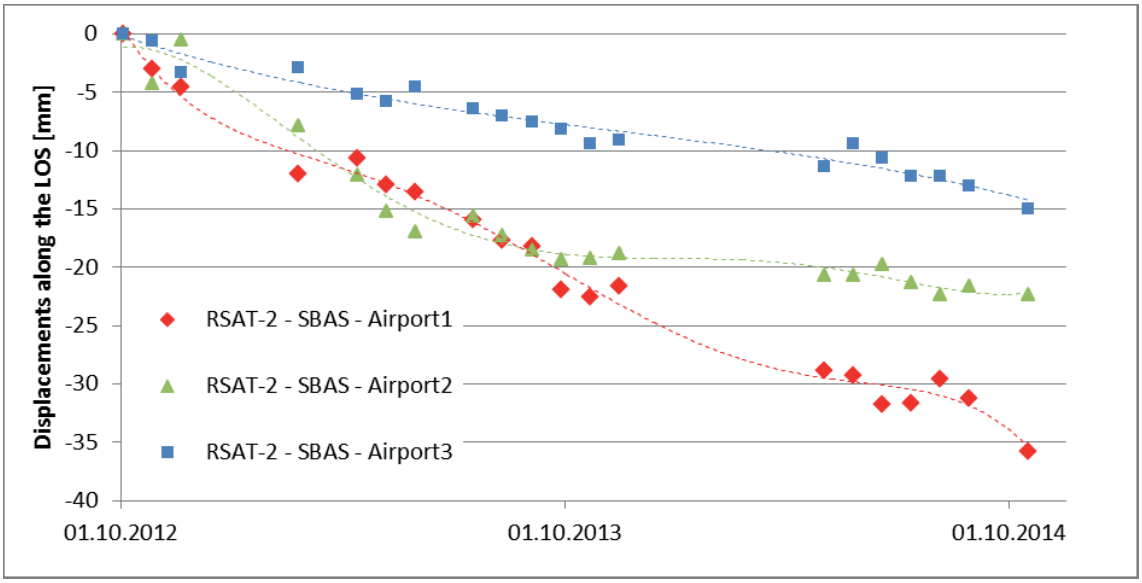

Figure 43: Comparison of SBAS time series (RSAT-2 Ultrafine mode dataset) at different locations close to Bergen airport (locations 1-3: Figure 42) highlighting variable movement evolution.

4.3.2 INDRE ARNA

4.3.2.1 DEFORMATION MAPS

In Indre Arna, only two datasets are available: RSAT-2 Standard mode and TSX/TDX StripMap mode. The results presented in Figure 44 highlight moving areas close to harbour and the railway, and along the north-east facing slopes. On TSX/TDX StripMap mode results, movements on the bridge on the south-eastern part of the image are also visible. It should be noted that the reduced deformation map on the west facing slopes for RSAT-2 Standard mode is due to layover effects (wider mask than TSX/TDX StripMap mode).

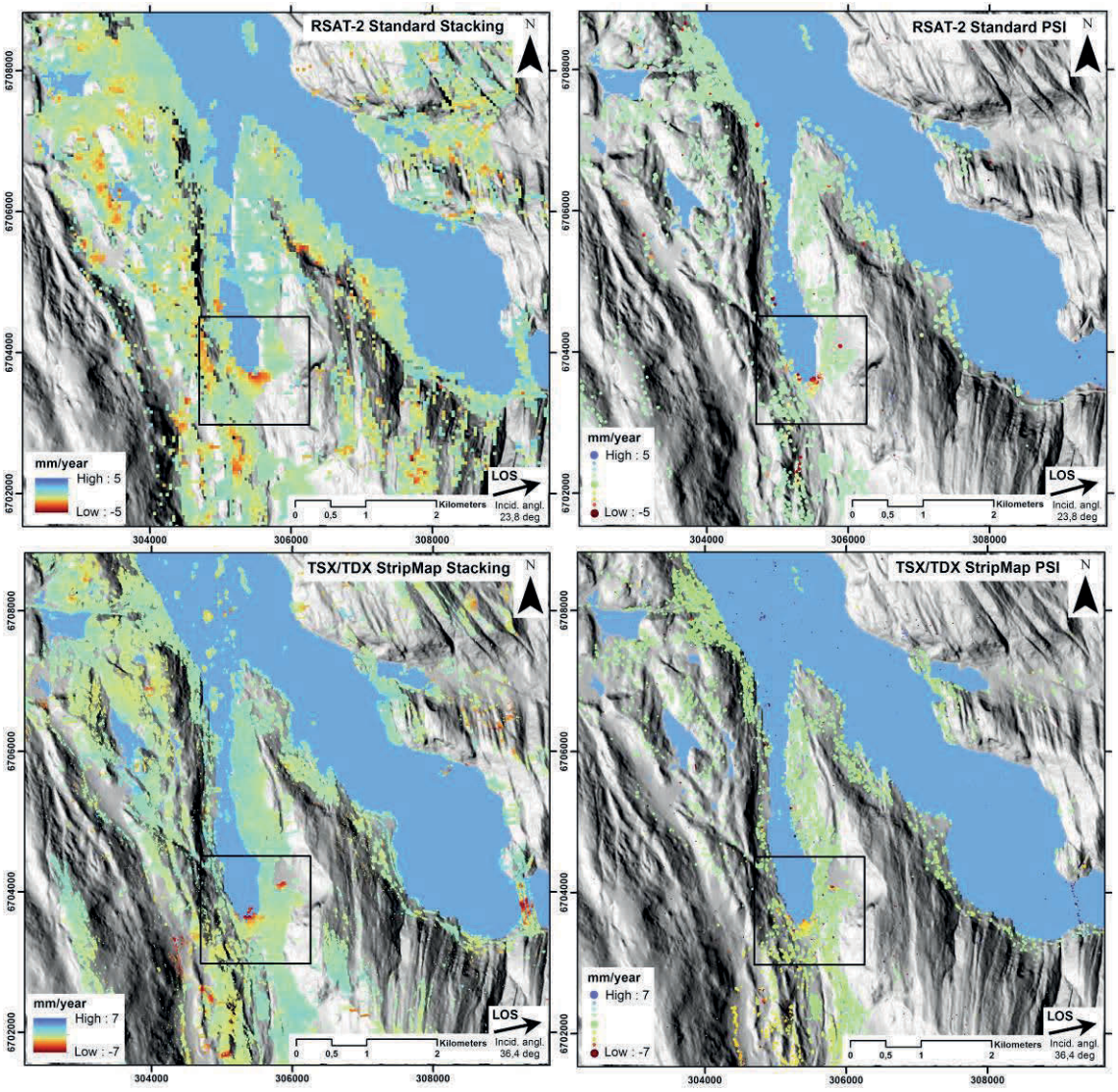

Figure 44: InSAR results in Indre Arna. Left: stacking results. Right: PSI results. Top: RSAT-2 Standard mode. Bottom: TSX/TDX StripMap mode [Cetinic, et al. 2015 (in prep.)]. Black square: zoom presented in Figure 45. Backgrounds: LOS-related shaded reliefs.

The zoom presented in Figure 45 highlights the clear difference of patterns delineation according to the spatial resolution. In the center of the image, movements affect progressively an area located between the railway and the harbour. In addition, displacements are visible in the northern part of a football field (NE of the image) and the slope in the western part is also affected by movement according to stacking (no Persistent Scatterers to compare).

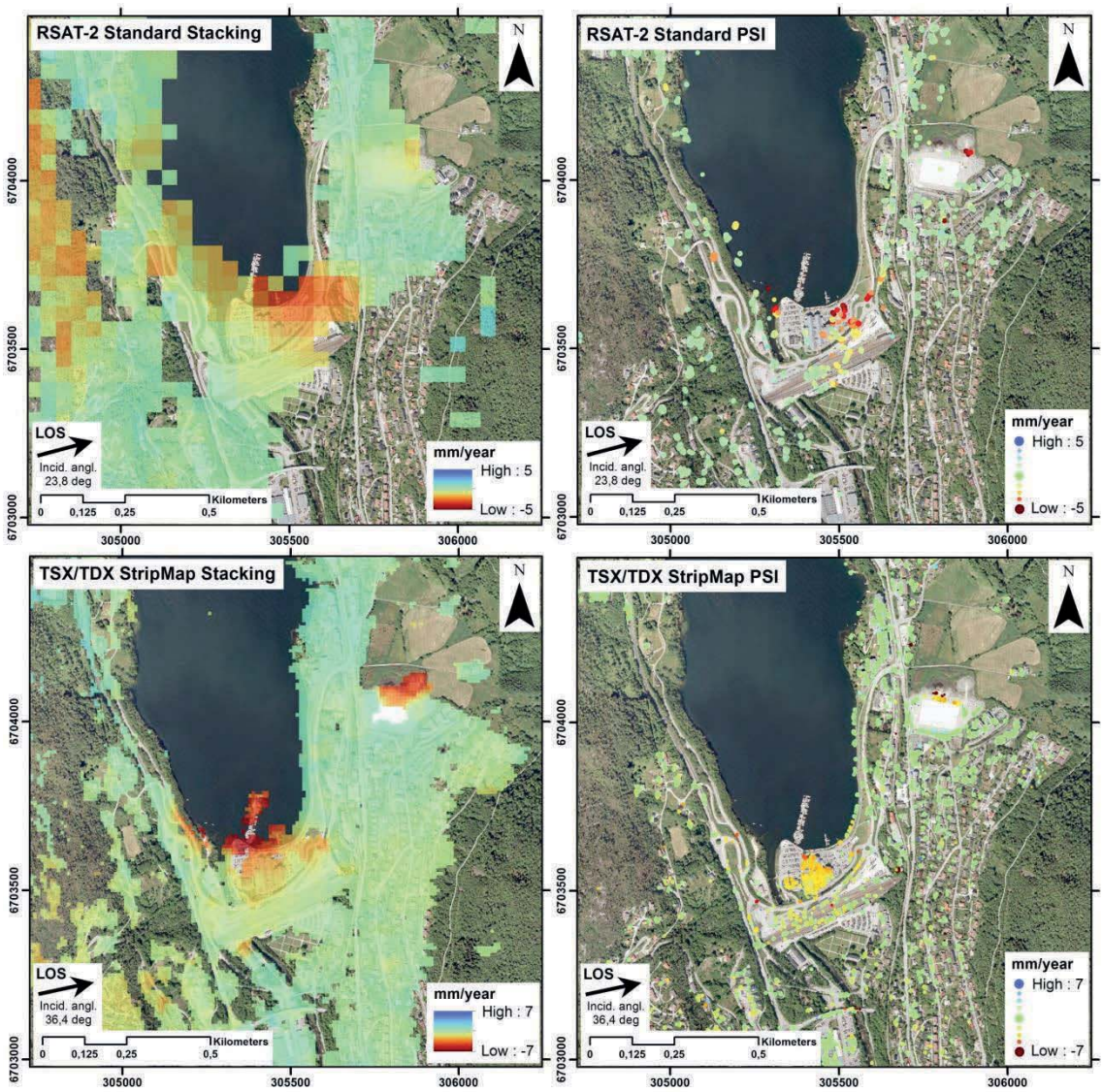

Figure 45: InSAR results on zoom in Indre Arna (black square in Figure 44). Left: stacking results. Right: PSI results. Top: RSAT-2 Standard mode. Bottom: TSX/TDX StripMap mode [Cetinic, et al. 2015 (in prep.)]. Backgrounds: Norge i bilder orthophoto.

4.3.2.2 TIME SERIES

In Indre Arna time series can also be analyzed. Here only TSX/TDX StripMap results are presented due to the better spatial resolution. Figure 46 shows the SBAS results with a zoom over the area where main deformation is detected. Time series are extracted for different locations highlighted using black stars.

Figure 47 displays time series at different locations between the harbour and the railway. Due to the gaps of scenes during the winter and noise affecting the results, the temporal evolution is unclear. However, it shows that the rate of movement progressively increase toward the sea.

Figure 48 shows an example of comparison between SBAS and PSI methods in the northern part of the football field. Even if some small trends are due to noise, the overall pattern with a deceleration in 2012 and acceleration at the end of the time period is quite similar between for two results.

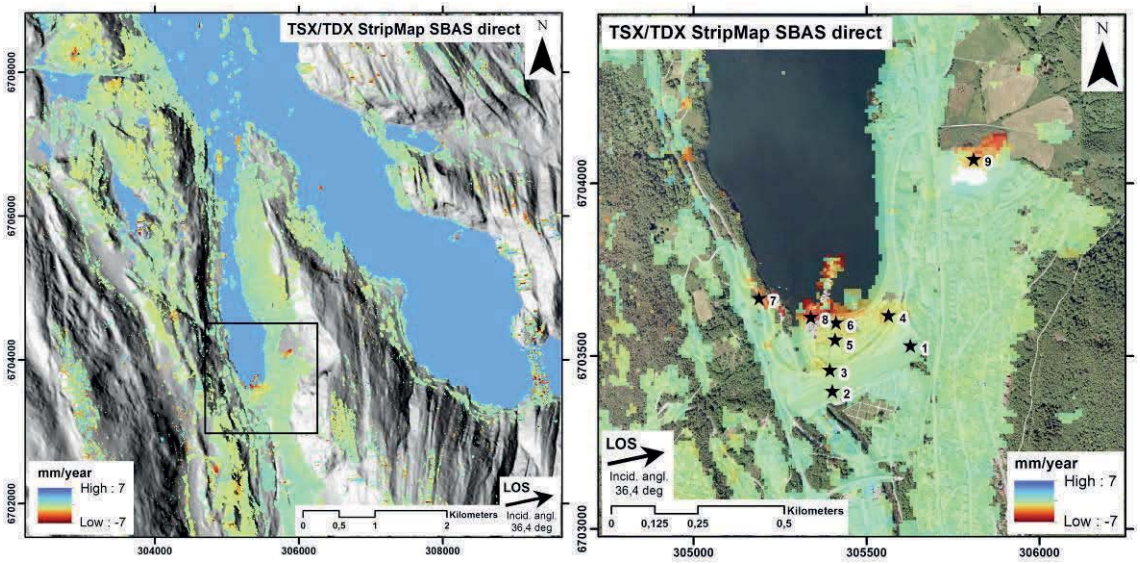

Figure 46: Left: SBAS results in Indre Arna for TSX/TDX StripMap mode [Cetinic, et al. 2015 (in prep.)]. Right: Zoom on the black square displayed on the left. Black stars: locations of time series presented thereafter. Backgrounds: Norge i bilder orthophoto & LOS-related shaded relief.

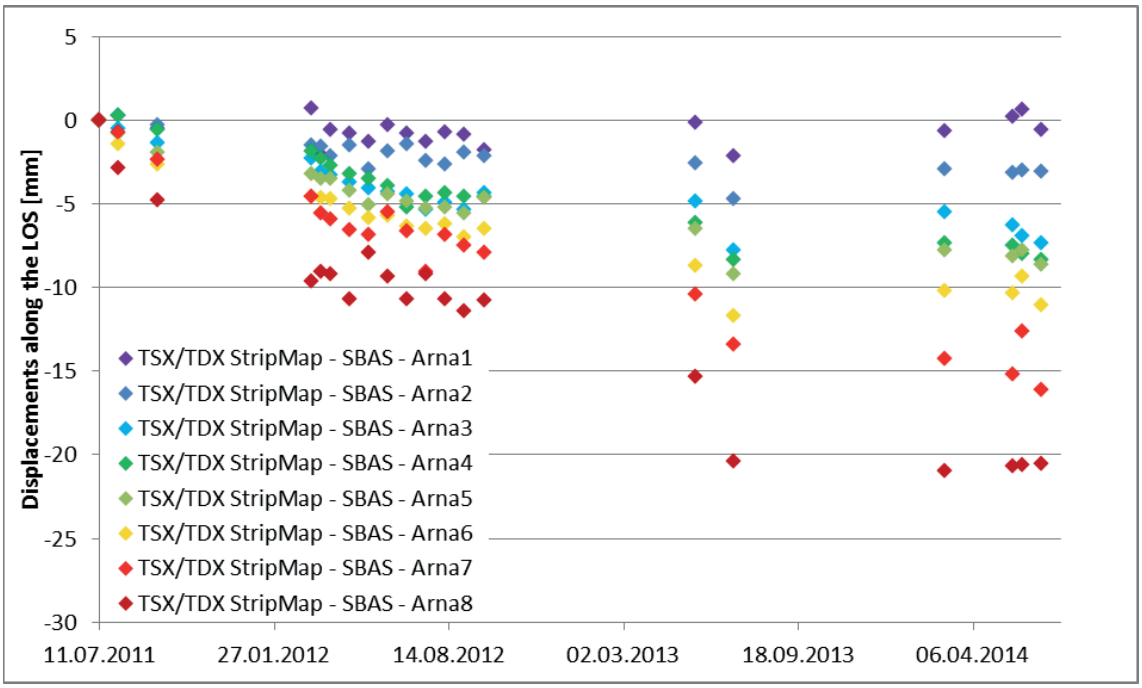

Figure 47: Comparison of SBAS time series (TSX/TDX StripMap mode dataset) at different locations between the railway and the harbour (locations 1-8: Figure 46) highlighting progressive spatial increase of displacement.

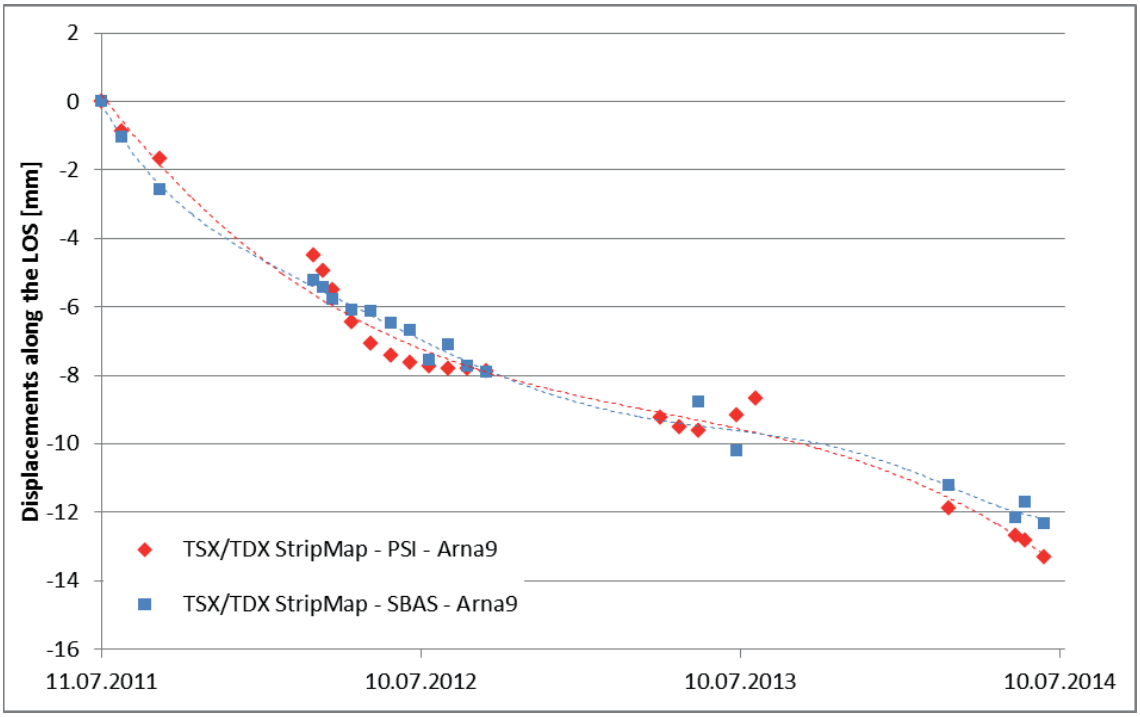

Figure 48: Comparison of time series from SBAS and PSI methods (TSX/TDX StripMap mode dataset) close to the Arna football field (location: Figure 46).

4.3.3 SAMNANGERFJORDEN - KVAMSSKOGEN - DALE

In the eastern part of the region of interest, only RSAT-2 Standard mode dataset and a little part of TSX/TDX StripMap mode dataset are available. In addition to the problems of geometrical effects (layover) and temporal decorrelation (due to vegetation and snow in winter), this reduces the detection capability due to the spatial resolution of RSAT-2 Standard mode. The SBAS processing did not provide reliable results, while PSI processing produced information on reduced sectors due to overall high amplitude dispersion.

Figure 49 presents the PSI results from RSAT-2 Standard mode at the head of Samnangerfjorden and in Kvamsskogen. At these locations, the coverage of Persistent Scatterers (PS) points is quite good due to artificial infrastructure. In between and over the mountains aside mostly no information is found. Some points show small displacement rates but no significant moving areas are highlighted.

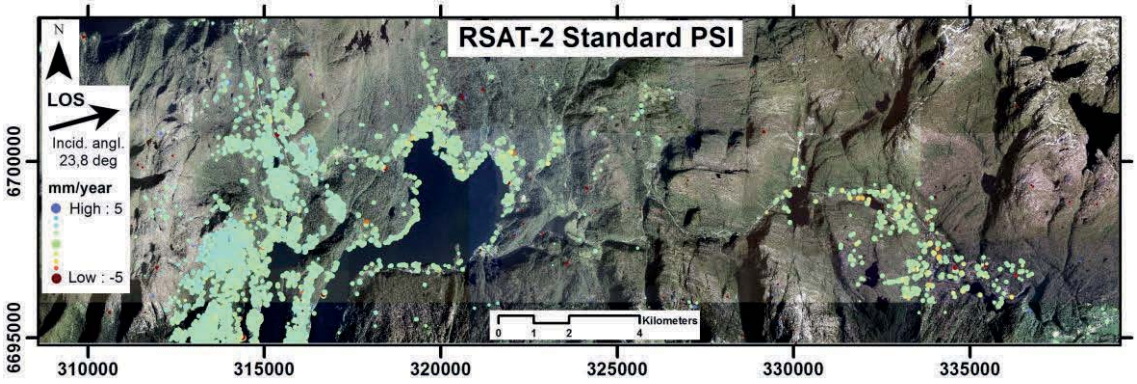

Figure 49: Overview of PSI results for RSAT-2 Standard mode at the head of Samnangerfjorden and in Kvamsskogen

In Figure 50, the RSAT-2 Standard mode results are compared with TSX/TDX StripMap mode results available at the head of Samnangerfjorden. Due to the higher spatial resolution, the PS coverage is better and more moving points are highlighted. On Kvamsskogen, no comparison with TSX/TDX StripMap mode is possible because the scenes do not cover this area.

Figure 51 gives an overview of RSAT-2 Standard mode results using PSI for the area between Vaksdal and Dale, as well as a zoom on the sector between Stanghelle and Dale. As for Samnangerfjorden and Kvamsskogen, the amount of PS points is low and they do not highlight significant moving areas. Moreover a large portion of the E16 road on the east side of the fjord is unfortunately located in an area affected by layover. No comparison with TSX/TDX StripMap mode is possible because the scenes do not cover the entire area.

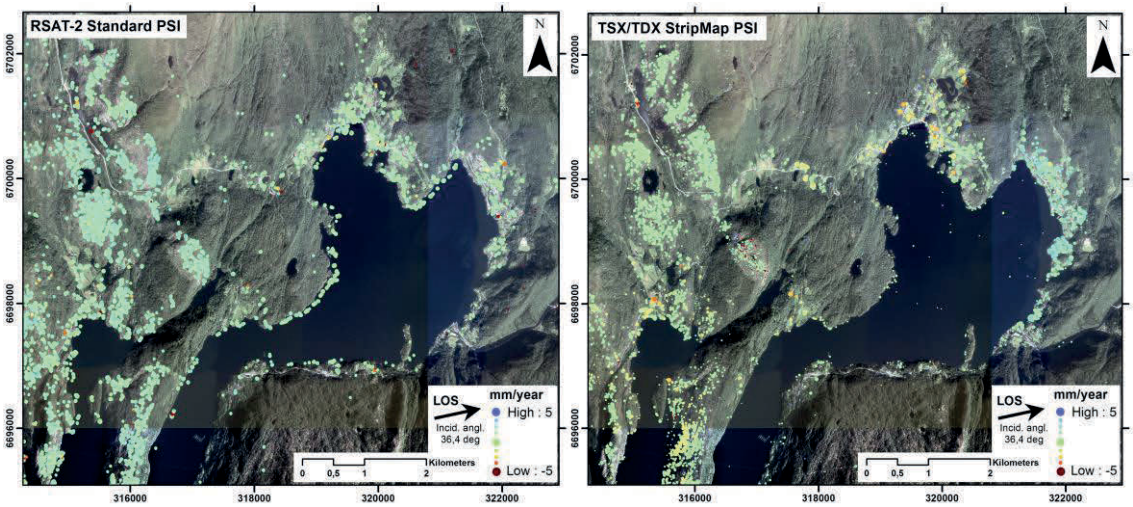

Figure 50: Zoom on the head of Samnangerfjorden showing PSI results. Right: RSAT-2 Standard mode. Left: TSX/TDX StripMap mode.

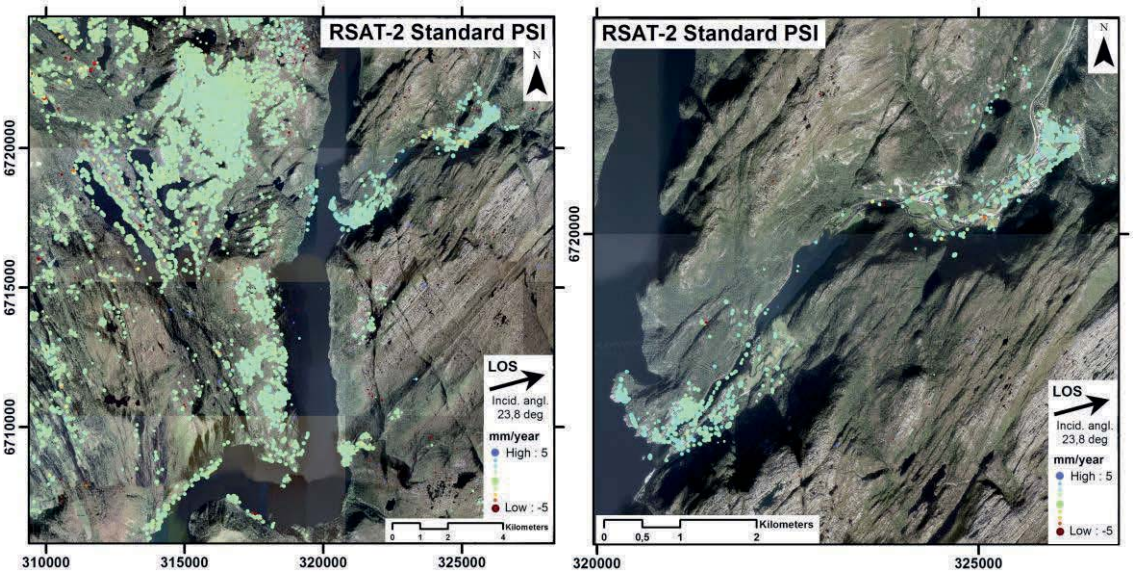

Figure 51: Right: overview of PSI results for RSAT-2 Standard between Vaksdal and Dale. Left: zoom on Stanghelle and Dale.

5 DISCUSSIONS

5.1 INSAR ADVANTAGES AND LIMITATIONS

As discussed in the previous chapters, SAR interferometry is a valuable tool to detect and monitor ground deformation. However, the technology is affected by several limitations, due to the intrinsic characteristics of SAR sensors, as well as the current processing issues. Table 7 summarizes these.

Table 7: Summary of the main advantages and limitations of InSAR technology for ground deformation measurements.

Advantages		**Limitations**	
Main element	Description	**Main element**	Description
Remote sensing	No need of access to the monitored area	**Relative measurement**	Measurement relative to a calibration/reference point
Active sensors	Acquisitions independent to illumination by the sun	**Uncontinuous monitoring**	At this moment, revisit time usually > 10 days. No InSAR information in between
Microwave sensors	Acquisitions independent to weather conditions	**Phase ambiguity**	Velocity has to be < λ/2 between 2 acquisitions and 2 points
Large coverage	Specially suitable for movement detection at regional scale	**Geometrical distortions**	Layover, shadow effects limit the real coverage.
		Variable spatial resolution	Spatial resolution can be too low to be able to detect small moving areas
Good accuracy	Ability to detect mm/yr displacement rates	**1-dimensional measurement**	Measurement along the line-of-sight (LOS). No sensitivity in N-S plane (near polar orbits)
Sensors development	Constant improvement of coverage, revisit times, resolutions, etc.	**Coherence variability**	Reduced capability on vegetated area, snow, etc. limits the real coverage
InSAR technology development	Significant research field: constant improvement of the processing chain	**Unwrapping procedure**	Due to the potential discontinuous movement patterns and decorrelation
Constant datasets enlargement	Availability of data from the 90's. Large datasets allow overcoming part of processing limitations	**Removing of atmospheric & topographic effects**	Due to the high variability of the atmospheric delay & uneven quality of the DEM used to remove the topographic component

The overall advantages and limitations of InSAR have an obvious impact on its present capability to be used for different kinds of applications in ground deformation measurement. These elements were previously discussed in the NRS-rapport(2014)2 "Kartlegging og overvåking av skredfare og infrastryktur ved bruk av radarsatellitter og InSAR-metodikk" [Strøm, et al., 2014], with a focus on the multi-use of InSAR by various Norwegian agencies.

In Table 8 we present a suggestion of the degree of maturity of InSAR technics for different applications involving different Norwegian actors (modified from [Strøm, et al., 2014]. The column "others" includes private actors (real estate, hydroelectric companies, etc.)

Table 8: Evaluation of degree of maturity of InSAR technics for various applications involving different Norwegian actors. Green: overall mature. Yellow: R&D stage. Red: Not mature. (X): main responsibility. (o): highly concerned. Modified from [Strøm, et al., 2014].

Involved actors / **Ex. of application**	NVE	NGU	Statens vegvesen	Jernbane-verket	Others
Rockslides	X	X	o	o	o
Subsidence in urban areas		X	X	X	X
Buildings deformation					X
Deformation over tunnels			X	X	o
Landslides (in loose material)	X	X	o	o	o
Roads deformation			X		X
Rails deformation				X	X
Hydroelectric infrastructure	o				X
Bridges deformation			X	X	X
Glaciers dynamics and mass balance	X				
Permafrost features evolution	o	X			
Rockfalls	X	X	o	o	o
Avalanches	X		o	o	o
Debris flows	X	o	o	o	o
Quick clays	X	o	o	o	o

5.2 INSAR DEVELOPMENTS AND POTENTIAL

The three last points presented in the InSAR advantages of the Table 7 highlight the significant potential of the technology due to its constant improvement and the enlargement of the available datasets. Thanks to these developments, the consequences of several major limitations on the results quality will progressively decrease. Indeed, most of the research activities relative to the sensors themselves, as well as those relative to the processing methods, are now focused on finding ways to overcome a part of the limitations presented in the right columns of Table 7. The availability of data with shorter revisit time allows monitoring more continuously the areas of interest and detecting faster movement. The availability of various sensors with different wavelengths, spatial resolutions and coverages, etc. allows wider applications (on various surfaces, at various scales and for detection of various movement rates). The enlargement of datasets can partly overcome the problem of atmospheric effects and allow more robust and representative results. Finally, it is obvious that the constant increase of research in this field allows developing complementary methods (e.g. SBAS, PSI), new algorithms and processing chains (for unwrapping procedure, atmospheric effects removing, DEM-errors estimation and removing, combination of geometries to get 2(3)-dimensional information, etc.).

Table 9 presents the main historical, present and planned SAR sensors between 1991 and 2020 (modified from [Strøm, et al., 2014). It highlights the good continuity of data availability and the overall increase of life duration of the satellites. Some of them were designed to work during 3-8 years but stayed operational much longer. Additional information about their characteristics was presented in Table 2 and Table 3 (section 2.1.7).

The availability and cost of the different satellite produces vary also. For historical analysis, archives from ERS-1/2 and Envisat are available from ESA and free of charge. RADARSAT-1/2 data are commercial but an agreement between Norway and Canada allows public use of more than 2000 scenes of different resolutions. For other commercial satellites as TerraSAR-X/TanDEM-X, Cosmo-Skymed or ALOS, agreements with customers are also possible to purchase stacks of images. Regardless of these possibilities, the prices vary according to sensor and the images modes. They correspond to about 1000-1300 € per StripMap scene for TerraSAR-X/TanDEM-X and Cosmo-Skymed, and 600 € for ALOS PALSAR product.

Table 10 focuses on the four planned satellites already presented in Table 9 (red) and highlights the main characteristics (spatial resolution, revisit time and coverage). Sentinel-1 is especially interesting. As part of the Copernicus program from the European Space Agency (ESA), this C-band satellite comprises a constellation of two satellites (one launched in 2014 and one planned for 2016). The data products are

publicly available and free of charge. The revisit time will reach 6 days with the launch of the second satellite and the coverage of Interferometric Wide Swath mode is very large: 250 x 250 km. As explained in Chapter 2, this makes impossible a very high spatial resolution. The full IWS resolution is 5 m x 20 m (range x azimuth). In addition to Sentinel-1, the new generations of Cosmo-Skymed, TerraSAR-X and RADARSAT satellites are planned to be launched between 2017 and 2018 with higher spatial resolutions.

Table 9: Overview of available historical (blue), present (green) and planned (red) SAR satellites data for movement detection. Light blue: satellite still operating but with modifications affecting InSAR applications. Modified from [Strøm, et al., 2014].

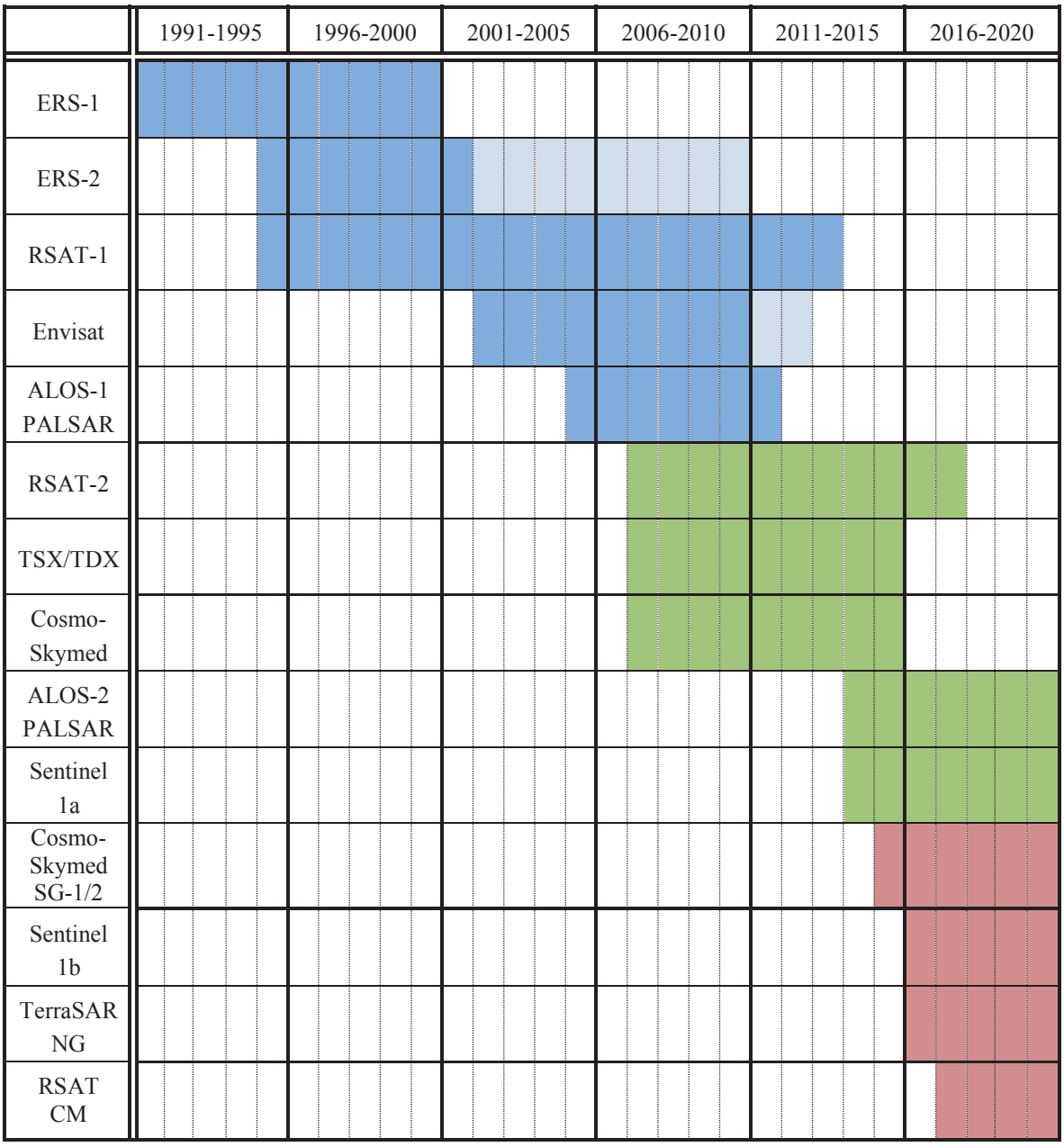

Table 10: Overview of main characteristics for some recent & planned SAR satellites. Modified from [Strøm, et al., 2014].

SAR satellite	Spatial resolution [m]	Launch	Revisit time	Coverage [km]
Sentinel-1a/1b	IWS[1]: 5 x 20	1a: 2014 - 1b: 2016 -	12 days 6 days[2]	IWS: 250 x 250
Cosmo-Skymed SG – CSG	0.8 x 0.8 3 x 3 4 x 20 6 x 40	*2018* -	8 days[2] (potentially 1 day[3])	10 x 10 40 x 40 100 x 100 200 x 200
TerraSAR-X NG	1.2 x 1-4 3 x 3-6 16 x 16	*2017* -	6 days[3]	5-10 x 10 30 x 30-50 100 x 100
RADARSAT CM	3 x 3 5 x 5 30 x 30	*2018* -	4 days[2]	20 x 20 30 x 30 125 x 125

[1] IWS = Interferometric Wide Swath mode

[3] Revisit time with 2 satellites

[3] Revisit time with 3 satellites

In Italic: Uncertain launch time

6 CONCLUSION

In the previous chapters, basic theory and main advantages and limitations of satellite InSAR technology for ground deformation detection were explained (Chapter 2), exemplified using the case of Bergen area (Chapter 3 and 4) and discussed (Chapter 5).

InSAR is a unique method for both mapping and monitoring of movement in natural terrain and manmade infrastructure. InSAR's greatest advantages are that it can be applied over remote and otherwise unmonitored areas and it gives in many cases a broad overview of the deformation, not only punctual information as most of the in situ monitoring techniques. It is also independent of any deployed infrastructure, except if you want to measure during the snow season or in heavy vegetation where the use of artificial corner reflectors is needed.

However, even if InSAR gives unique opportunities and for several applications the methods are today mature, several issues regarding to the characteristics of the sensors and the processing methods can still limit its use, i.e. in steep terrain (shadow and layover effects), in regions affected by vegetation and snow cover (temporal decorrelation) and for the detection of small areas moving fast (due to spatial resolution and phase ambiguity).

Being aware of these actual limitations, it is possible to play with the complementarity of the datasets, and to adapt the choice of them to the characteristics of the area and the required applications. It also shows the need to continue the development and research to overcome the present limitations and extend the capabilities and applicability of the technology.

In the report we have exemplified the use of InSAR showing the differences with regard to temporal and spatial resolutions and spatial coverage of some of the most common sensors today. To cover broad areas Sentinel-1 will be ideal. With both Sentinel-1a and 1b operational we will have 6 days temporal resolution, giving unpreceded opportunities for regional monitoring. The European Space Agency has a free and open Sentinel-1 data policy, but a national coverage with InSAR will need resources for the processing and interpretation of the results. Applying these data at a regional scale, we will get an overview of areas to be further investigated for risk and eventually more closely monitored.

For many applications the spatial resolution of Sentinel-1 will not be sufficient (e.g. for roads, railways or small geohazards). There is thus a need for higher resolution satellites such as e.g. TerraSAR-X/TanDEM-X or Cosmo-Skymed. These satellites are operated commercially, do not have a continuous acquisition plan (data need in many cases to be ordered in advance to get time series) and data are relatively expensive. However, for certain high priority areas, such as bridges, dams, some roads or railway sections these

data can give a very detailed and cost efficient method for surveillance compared to intensive in situ monitoring networks.

InSAR is however not sufficient for high risk objects where continuous surveillance and warning is necessary, as the well-known geohazards of Mannen, Åknes or Nordnes. InSAR need time series of 15-20 scenes before we can obtain reliable results, and the temporal resolution will never be sufficient for continuous monitoring. However, for 'medium risk' objects, that need to be followed on a cost effective way over many years, InSAR with deployment of corner reflectors is a valuable method for long-term periodic monitoring.

To conclude, we see that InSAR in the coming years, both due to the steadily increasing availability of data, better processing methods and an increasing number of users and service providers, will be more and more used as a tool for mapping and monitoring of geohazards and infrastructure.

7 REFERENCES

Amelung, F., Jónsson, S., Zebker, H., & Segall, P. (2000). Widespread uplift and 'trapdoor' faulting on Galápagos volcanoes observed with radar interferometry. *Nature, 407*, pp. 993-996. doi:10.1038/35039604

Balmer, R., & Hart, P. (1998). Synthetic aperture radar interferometry. *Inverse Problems, 14*, pp. R1-54. doi:10.1088/0266-5611/14/4/001

Berardino, P., Costantini, M., Franceschetti, G., Iodice, A., Pietranera, I., & Rizzo, V. (2003). Use of differential SAR interferometry in monitoring and modelling large slope instability at Maratea (Basilicata, Italy). *Engineering Geology, 68*, pp. 31-51. doi:10.1016/S0013-7952(02)00197-7

Berardino, P., Fornaro, G., Lanari, R., & Sansosti, E. (2002). A new algorithm for surface deformation monitoring based on small baseline differential SAR interferograms. *IEEE Transactions on Geoscience and Remote Sensing, 40*(11), pp. 2375-2383. doi:10.1109/TGRS.2002.803792

Burrough, P. A., & McDonell, R. (1998). *Principles of Geographical Information Systems.* New York: Oxford University Press.

Cetinic, F., Rouyet, L., & Lauknes, T. R. (2015 (in prep.). *High resolution SAR Interferometry for ground deformation over Bergen area (report).* Globesar.

Colesanti, C., & Wasowski, J. (2006). Investigating landslides with space-borne Synthetic Aperture Radar (SAR) interferometry. *Engineering Geology, 88*(3-4), pp. 173-199. doi:10.1016/j.enggeo.2006.09.013

Colesanti, C., Ferretti, A., Novali, F., Prati, C., & Rocca, F. (n.d.). SAR monitoring of progressive and seasonal ground deformation using the permanent scatterers technique. *IEEE International Geoscience and Remote Sesning, 41*(7), pp. 1685-1701. doi:10.1109/TGRS.2003.813278

Cumming, I. G., & Wong, F. H. (2005). *Digital Processing of Synthetic Aperture Radar Data: Algorithms and Implementation.* New York, U.S.A: Artech House Inc.

Curlander, J. C., & McDonough, R. N. (1991). *Synthetic Aperture Radar.* New York, U.S.A: John Wiley & Sons.

Eriksen, H. (2013). Slope displacement patterns observed using satellite InSAR data in the Storfjord-Kåfjord-Lyngen region, Troms. *Master thesis*, University of Tromsø, Norway.

Ferretti, A. (2014). *Satellite InSAR Data, Reservoir Monitoring from Space.* DB Houten, The Netherlands: EAGE Publications, Education Tour Series.

Ferretti, A., Monti-Guarnieri, A., Prati, C., Rocca, F., & Massonnet, D. (2007). *InSAR Principles: Guidelines for SAR Interferometry. Processing and Interpretation.* Noordwijk, The Netherlands: ESA Publications.

Ferretti, A., Prati, C., & Rocca, F. (2000). Nonlinear subsidence rate estimation using permanent scatterers in differential SAR interferometry. *IEEE Transactions on Geoscience and Remote Sensing, 38*(5), pp. 2202-2212. doi:10.1109/36.868878

Ferretti, A., Prati, C., & Rocca, F. (2001). Permanent Scatterers in SAR Interferometry. *IEEE Transactions on Geosciences and Remote Sensing, 39*(1), 8-20. doi:10.1109/36.898661

Franceschetti, G., & Lanari, R. (1999). *Synthetic Aperture Radar Processing.* Boca Raton, U.S.A.: CRC Press.

Gabriel, A. K., Goldstein, R. M., & Zebker, H. A. (1989). Mapping small elevation changes over large areas: Differential radar interferometry. *Journal of Geophysical Research, 94*(B7), 9183-9191. doi:10.1029/JB094iB07p09183

Goldstein, R. M., Engelhardt, R., Kamp, B., & Frolich, R. M. (1993). Satellite radar interferometry for monitoring ice sheet motion: Application to an Antarctic ice stream. *Science, 262*, pp. 1525-1530. doi:10.1126/science.262.5139.1525

Hanssen, R. (2001). *Radar Interferometry: Data Interpretation and Error Analysis.* Dordrecht, The Netherlands: Kluwer Academic.

Hilley, G. E., Bürgmann, R., Ferretti, A. N., & Rocca, F. (2004). Dynamics of slow-moving landslides from permanent scatterer analysis. *Science, 304*(5679), pp. 1952-1955. doi:10.1126/science.1098821

Hooper, A., Segall, P., & Zebker, H. (2007). Persistent scatterer interferometric synthetic aperture radar for crustal deformation analysis, with application to Volcán Alcedo, Galápagos. *Journal of Geophysical Research,, 112*(B07407). doi:10.1029/2006JB004763

Hooper, A., Zebker, H., Segall, P., & Kampes, B. (2004). A new method for measuring deformation on volcanoes and other natural terrains using InSAR persistent scatterers. *Geophysical Research Letters, 31*(L23611). doi:10.1029/2004GL021737

Johansen, B. (2009). *Vegetasjonskart for Norge basert Landsat TM/ETM+ data. Rapport 4/2009.* Norut.

Johansen, B., Aarrestad, P. A., & Øien, D. I. (2009). *Vegetasjonskart for Norge basert på satellittdata. - Klasseinndeling og beskrivelse av utskilte vegetasjonstyper. Rapport 3/2009.* Norut.

Kampes, B. M. (2006). *Radar Interferometry - Persistent Scatterer Technique.* Dordrecht, The Netherlands: Springer.

Lanari, R., Casu, F., Manzo, M., Zeni, G., Berardino, P., Manuta, M., & Pepe, A. (2007). An overview of the small baseline subset algorithm: A DInSAR technique for surface deformation analysis. *Pure and Applied Geophysics, 164*(4), pp. 637-661. doi:10.1007/s00024-007-0192-9

Larsen, Y., Engen, G., Lauknes, T. R., Malnes, E., & Høgda, K. A. (2005). A generic differential InSAR processing system, with applications to land subsidence and SWE retrieval. *Proc. ESA Fringe 2005*, ESA ESRIN, Frascati, Italy, November 28-December 2.

Lauknes, T. R. (2010). Rockslide mapping in Norway by means of interferometric SAR time series analysis. *Ph.D. Thesis*, University of Tromsø, Norway.

Lauknes, T. R., Zebker, H. A., & Larsen, L. (2011). InSAR Deformation Time Series Using an-Norm Small-Baseline Approach. *IEEE Transactions on Geoscience and Remote Sensing, 49*(1), pp. 536-546. doi:10.1109/TGRS.2010.2051951

Lundgren, P., Usai, S., Sansosti, E., Lanari, R., Resauro, M., Fornato, G., & Berardino, P. (2001). Modelling surface deformation observed with synthetic aperture radar interferometry at Campi Flegrei caldera. *Journal of Geophysical Research, 106*(B9), pp. 19355–19366. doi:10.1029/2001JB000194

Massonet, D., Briole, P., & Arnaud, A. (1995). Deflation of Mount Etna monitored by spaceborne radar interferometry. *Nature, 375*, pp. 567-570. doi:10.1038/375567a0

Massonnet, D., & Feigl, K. L. (1998). Radar interferometry and its applications to changes in the Earth's surface. *Reviews of Geophysics, 36*(4), pp. 441-500. doi:10.1029/97RG03139

Massonnet, D., Rossi, M., Carmona, C., Adragna, F., Peltzer, G., Feigl, K., & Rabaute, T. (1993). The displacement field of Landers earthquake mapped by radar interferometry. *Nature, 364*(8), pp. 138-142. doi:10.1038/364138a0

Mora, O., Mallorqui, J. J., & Broquetas, A. (2003). Linear and non-linear terrain deformation maps from a reduced set of interferometric sar images. *IEEE Transactions on Geoscience and Remote Sensing, 41*(10), pp. 2243-2253. doi:10.1109/TGRS.2003.814657

Peltzer, G., Crampé, F., Hensley, S., & Rosen, P. (2001). Transient strain accumulation and fault interaction in the Eastern California shear zone. *Geology, 29*(11), pp. 975-978. doi:10.1130/0091-7613(2001)029

Pepe, A., Oriz, A. B., Lundgren, P. R., Rosen, P. A., & Lanari, R. (2011). The stripmap-ScanSBAS approach to fill gaps in stripmap deformation time series with ScanSAR data. *IEEE Transactions on Geoscience and Remote Sensing, 49*(12), pp. 4788-4804. doi:10.1109/TGRS.2011.2167979

Prati, C., Ferretti, A., & Perissin, C. (2010). Recent advances on surface ground deformation measurement by means of repeated space-borne SAR observations. *Journal of Geodynamics, 49*(3-4), pp. 161-170. doi:10.1016/j.jog.2009.10.011

Rocca, F., Prati, F., Guarnieri, A. M., & Ferretti, A. (2000). SAR interferometry and its applications. *Surveys in Geophysics, 21*(2-3), pp. 159-176. doi:10.1023/A:1006710731155

Rosen, P. A., Hensley, S., Joughin, I. R., Li, F. K., Madsen, S. N., Rodríguez, E., & Goldstein, R. M. (2000). Synthetic Aperture Radar Interferometry. *Proceedings of the IEEE, 88*(3), pp. 333-382. doi:10.1109/5.838084

Rott, H. N. (2006). The contribution of radar interferometry to the assessment of landslide hazards. *Advances in Space Research, 37*(4), pp. 710-719. doi:10.1016/j.asr.2005.06.059

Sandwell, D. T., & Price, E. J. (1998). Phase gradient approach to stacking interferograms. *Journal of Geophysical Research, 103*(B12), pp. 39183-30204. doi:10.1029/1998JB900008

Sansosti, E., Casu, F., Manzu, M., & Lanari, R. (2010). Space-borne radar interferometry techniques for the generation of deformation time series: An advanced tool for Earth's surface displacement analysis. *Geophysical Research Letters, 137*(L20305). doi:10.1029/2010GL044379

Schmidt, D., & Bürgmann, R. (2003). Time-dependent land uplift and subsidence in the Santa Clara valley, California, from a large InSAR data set. *Journal of Geophysical Research, 108*(B9). doi:10.1029/2002JB002267

Strozzi, T., Farina, P., Corsini, A., Ambrosi, C., Thüring, M., Zilger, J., Wiesmann, A., Wegmüller, U. & Werner, C. (2005). Survey and monitoring of landslide displacements by means of L-band satellite SAR interferometry. *Landslides, 2*(3), pp. 193-201. doi:10.1007/s10346-005-0003-2

Strøm, G. D., Moldestad, D. A., Øydvin, E. K., Dehls, J., Bjordal, H., & Fevang, P. A. (2014). *Karlegging og overvåkning av skredfare og infrastruktur ved bruk av radarsatellitter og InSAR-metodikk. Grunnlag for en strategisk plan for offentlig bruk av interferometri i Norge (NRS-rapport(2014)2).* Norsk Romsenter.

Werner, C., Wegmüller, U., Strozzi, T., & Wiesmann, A. (2003, July 21-25). Interferometric point target analysis for deformation mapping. *Proceedings of International Geoscience and Remote Sensing Symposium 2003 (IGARSS'03)*, pp. 4362-4364.

Woodhouse, I. H. (2006). *Introduction to Microwave Remote Sensing.* Boca Raton, U.S.A.: Taylor & Francis.

Zebker, H. A., Rosen, P. A., Goldstein, R. M., Gabriel, A., & Werner, C. L. (1994). On the derivation of coseismic displacement fields using differential radar interferometry: The Landers earthquake. *Journal of Geophysical Research, 99*(B10), pp. 19617-19634. doi:10.1029/94JB01179

8 APPENDIXES

8.1 RSAT-2 STANDARD MODE IMAGES

Table 11: RSAT-2 Standard mode scenes (ascending geometry).

Date	Perp. baseline [m]	Temp. baseline [days]
08.11.2008	-256,4	-1776
02.12.2008	13,8	-1752
26.12.2008	69,6	-1728
19.01.2009	-249,6	-1704
12.02.2009	-436,3	-1680
08.03.2009	-25,7	-1656
01.04.2009	-72,4	-1632
25.04.2009	-129,5	-1608
19.05.2009	-187,1	-1584
12.06.2009	307,6	-1560
06.07.2009	216,1	-1536
30.07.2009	-285,6	-1512
23.08.2009	-268,3	-1488
16.09.2009	-276,5	-1464
10.10.2009	-460,0	-1440
03.11.2009	11,4	-1416
27.11.2009	-73,1	-1392
29.10.2010	-123,3	-1056
22.11.2010	106,8	-1032
16.12.2010	-71,8	-1008
02.02.2011	97,9	-960
26.02.2011	-186,4	-936
15.04.2011	178,1	-888
09.05.2011	197,3	-864
02.06.2011	32,8	-840
26.06.2011	112,7	-816
20.07.2011	118,6	-792
13.08.2011	188,8	-768
06.09.2011	-303,7	-744
30.09.2011	-98,9	-720
24.10.2011	29,1	-696
17.11.2011	-76,9	-672
11.12.2011	89,9	-648
28.01.2012	-48,0	-600
21.02.2012	88,8	-576
16.03.2012	-5,5	-552
09.04.2012	175,7	-528

03.05.2012	-128,7	-504
27.05.2012	242,7	-480
20.06.2012	412,2	-456
14.07.2012	252,2	-432
31.08.2012	49,0	-384
24.09.2012	-218,5	-360
18.10.2012	-119,5	-336
05.12.2012	-90,1	-288
29.12.2012	60,0	-264
22.01.2013	17,9	-240
15.02.2013	-119,0	-216
11.03.2013	15,8	-192
04.04.2013	-21,1	-168
28.04.2013	217,6	-144
22.05.2013	310,9	-120
15.06.2013	146,9	-96
09.07.2013	221,0	-72
02.08.2013	78,9	-48
26.08.2013	-20,8	-24
19.09.2013	**0,0**	**0**
13.10.2013	-84,2	24
06.11.2013	3,0	48
30.11.2013	182,3	72
24.12.2013	-95,0	96
06.03.2014	73,9	168
30.03.2014	143,2	192
23.04.2014	114,6	216
17.05.2014	206,4	240
10.06.2014	361,2	264
04.07.2014	228,2	288
28.07.2014	304,6	312
21.08.2014	134,2	336
14.09.2014	-19,6	360
08.10.2014	175,0	384
01.11.2014	-6,1	408

8.2 RSAT-2 ULTRAFINE IMAGES

Table 12: RSAT-2 Ultrafine scenes (descending geometry).

Date	Perp. baseline [m]	Temp. baseline [days]
03.10.2012	-249,6	-336
27.10.2012	-148,2	-312
20.11.2012	-265,2	-288
24.02.2013	-27,2	-192
13.04.2013	-33,9	-144
07.05.2013	78,6	-120
31.05.2013	32,5	-96
18.07.2013	-15,0	-48
11.08.2013	17,1	-24
04.09.2013	**0,0**	**0**
28.09.2013	-81,1	24
22.10.2013	1,6	48
15.11.2013	9,8	72
02.05.2014	146,8	240
26.05.2014	210,5	264
19.06.2014	183,3	288
13.07.2014	271,1	312
06.08.2014	148,1	336
30.08.2014	6,2	360
17.10.2014	-85,6	408

8.3 TSX/TDX STRIPMAP IMAGES

Table 13: TSX/TDX StripMap scenes (ascending geometry). From [Cetinic, et al. 2015 (in prep.)].

Date	Perp. Baseline [m]	Temp. baseline [days]
11.07.2011	37,3	-22
02.08.2011	**0,0**	**0**
15.09.2011	-14,9	44
09.03.2012	64,4	220
20.03.2012*	225,5	231
31.03.2012	-95,4	242
22.04.2012	-19,0	264
14.05.2012	31,8	286
05.06.2012	104,8	308
27.06.2012	-18,5	330
19.07.2012	-43,8	352
10.08.2012	-36,0	374
01.09.2012	41,4	396
23.09.2012	-93,6	418
09.04.2013	160,4	616
01.05.2013	-65,2	638
23.05.2013	15,4	660
06.07.2013	-1,0	704
28.07.2013	-83,8	726
05.03.2014*	-139,9	946
21.05.2014	-92,4	1023
01.06.2014	85,4	1034
23.06.2014	30,0	1056

* TanDEM-X scenes

Norges vassdrags- og energidirektorat

Middelthunsgate 29
Postboks 5091 Majorstuen
0301 Oslo

Telefon: 09575
Internett: www.nve.no